Doctoral Dissertation

Fabrication and Evaluation of Thin Composite Emission Filters for Implantable Fluorescent Micro-Imagers in the Deep Brain.

脳深部埋植型蛍光イメージングデバイス用 複合薄膜エミッションフィルタの作製と評価

Erus Rustami

September 2020

NARA INSTITUTE OF SCIENCE AND TECHNOLOGY
GRADUATE SCHOOL OF MATERIALS SCIENCE

Acknowledgment

Foremost, I would like to thank Prof. Jun Ohta, the head of Photonic Device Science Laboratory, for his kind decision accepting me as a doctoral student. We met through an unusual path of doctoral pre-screening program hosted in 2016, where he was my examiner at that time. His enthusiasm and fascinating research theme that is relatively close to my previous work and I intend to do in the future, had convinced me to join his laboratory. Also, throughout my doctoral program, thanks for being such a wonderful mentor, for nurturing research skills, and fostering my future academic career.

I would like to thank my supervisors, Prof. Masakazu Nakamura and Prof. Hisao Yanagi, for providing a comfortable discussing atmosphere and for all the positive feedback. I would also like to thank Assoc. Prof. Kiyotaka Sasagawa, for his patience in guiding and invaluable assistance during the program. Also, for the fruitful discussion in overcoming research's hindrance, which provides a solid background of the lens-free fluorescent images system, that is something new for me.

I would also like to thank Prof. Takashi Tokuda (has been transferred to Tokyo Institute of Technology), Assoc. Prof. Toshihiko Noda (has been transferred to the Toyohashi University of Technology), Assoc. Prof. Hiroyuki Tashiro, Assistant Professor Makito Haruta, and Assistant Professor Hironari Takehara for every technical support required to do productive research activities during my doctoral program. I would also like to appreciate our lab's secretary, Ms. Ryoko Fukuzawa, who always helps me to deal with the administrative aspects and paperwork. Also, for her helps in settling my daughter's pre-school the first time we arrived in Japan.

To be honest, this thesis would have never seen the light of day without helps and supports from a lot of a wonderful person in such direct or indirect ways. It would be impossible to mention everyone individually in the following couple of pages, but be assured that all help is appreciated. For all current members of the Photonic Device Science Laboratory group, thank you all for giving a pleasant environment to work in and all the fun activities we have done. I feel we are more likely a family than just a research partner—all the best to all of you. Also, the laboratory staff who always help whenever I had a technical problem. Special thanks to Dr. Yasumi Ohta, who always shares her positive energy and continuously giving the presents to the member's lab. Notably, for her kind supported when we had a hard time because of my wife's health problems in my third's doctoral year. Thank you very much.

All the Indonesian friends and communities in NAIST that make it feel like home," *Terima kasih banyak dan sampai jumpa di Indonesia*." My family in Indonesia, my parents, siblings, for all the loves, supports, and prayers. All your intangibles support has made encouraged me, in one way or another, and keep believing that with difficulties, there is an easiness. Finally, and as always, I am eternally grateful to my wife, Neneng Sri Wahyuningsih, for being at my side. You sacrificed a lot for me in this journey. My daughters, Aisha and Athiya, thank you for continually teaching me love and sincerity, and for all the smiles and laughs every time I reach home. You are my mood booster. Hopefully, I can be an excellent partner and enlightening father for you. Without all of you, nothing that I do would make much sense.

Contents

Table of Figures

1 Introduction

The term “neuroscience” was introduced in the mid-1960s, where different disciplines worked together cooperatively in response to resolve complicated and extensive problems recently emerged. Neuroscience can be defined as a multidisciplinary science that analyzes the nervous system to understand the biological basis for behavior. Members of the neuroscience research group mostly come from mathematics, engineering, biology, chemistry, etc. Neuroscience study today spans a wide range of endeavors from the molecular biology of nerve cells and medical aspects of the nervous system to the biological basis of behavior, emotion, and cognitive [1]. Those various fields focus on unique elements, but they often work in the intersection area.

Among those broad fields of neuroscience, behavioral neuroscience is one of the fastest-growing research themes in recent years. This discipline attempts to understand information processing in an organism’s nervous system in response to its environment. The next section briefly discusses the benefit and experimental method of behavioral experiments, followed by imaging modalities commonly used to perform behavioral experiments, including the advantages and disadvantages of each modality. Among those imaging modalities, an implantable CMOS image sensor will have more exploration as it will be used as an imaging platform at work. The section ends with the research statement and an outline of the thesis structure.

1.1 Behavioral Experiment

Performing behavioral experiments is one way to understand the functional brain neural cells and its underlying mechanism related to psychological and physical activities [2], [3]. The

neural activities of specific brain area must be measured while observing the behavioral treatment experiment in awake and freely moving conditions, e.g., how animal solves problems or when they are under stress or pain circumstances. This freely moving condition, which is resembling the animal's typical life, provides more sensible behavior data than that in using anesthetics and physical restraints with head-fixed optical microscopy methods.

Various type of behavioral experiment through animal studies has been developed so far including a model for the neuropsychiatric disorders from alcohol and drug addiction [4], [5], and observing anxiety-and depression-like behavior of mice as a risk factor for Parkinson's disease [6]. Another example of the behavioral experiment is measuring protease activities in the hippocampal CA1 region during the artificial epilepsy induction and long-term observation of the gamma-Aminobutyric acid (GABA)—a primary inhibitory neurotransmitter that decreases neuron's action potential—changes in the amygdala in corresponding with the acute stress [7].

Furthermore, a behavioral experiment is essential in gaining our understanding of the brain function to fight several neurological diseases that harmed humankind's health, such as Alzheimer's and Parkinson's disease. In 2015, Alzheimer's Disease International—the international federation of Alzheimer associations throughout the world—estimated people suffered by dementia around the world about 131.5 million by 2050. Alzheimer's disease is the most common form of dementia and possibly contributes to 60−70% of cases. Figure 1.1 shows the infographic of the projected number of people living with dementia by 2050 [8]. In addition to dementia, another neurodegenerative disease, i.e., Parkinson's disease, will affect about 9.3 million people by 2030 [9]. From that number of the projected cases, it is clear that the

neurodegenerative disease is becoming one of the significant human health problems in the future.

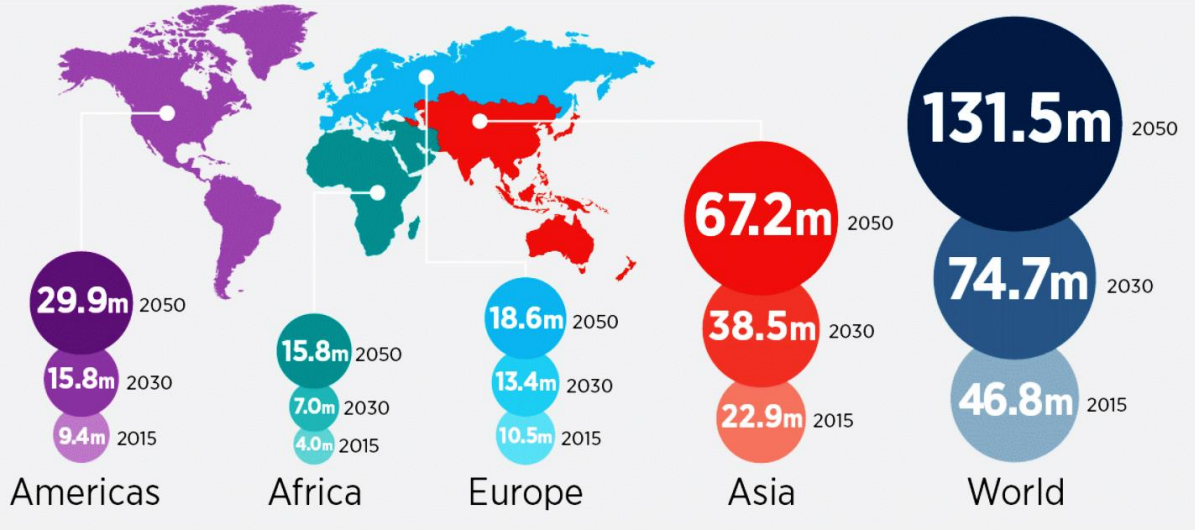

Figure 1.1 Projected number of people living with dementia by 2050
The people living with dementia estimated to increase every year, and it will reach about 131.5 million in around the world by 2050. Asia will be the main contributor to this trend for about 50% of the total number for every predicted year [8].

To date, the underlying mechanism of Alzheimer's is not understood yet. This syndrome is associated with the disease of the brain in the form of disturbance of multiple higher cortical functions, including memory, thinking, orientation, calculation, language, and judgment [10]. Those activities are related to the specific brain that is called the hippocampus. Many researchers suggested that this hippocampus region plays a critical role in the learning and memory process [11], [12]. Also, it has been reported that regional measures of hippocampal atrophy are one of the strongest predictors of Alzheimer’s disease progression [13]. Therefore,

developing a high-performance imaging device that can observe the neural activity, for instance, in the hippocampal region, is essential in the effort of understanding the underlying mechanism of some neurodegenerative disease.

Practically, even the ultimate goal in behavioral neuroscience is to understand the human brain function and its underlying mechanism; it is common practice in science to apply the new protocols on rodents before testing in human populations. Correspondingly, this situation also happened in the behavioral experiments that observe a neural activity of rodents as a target experiment. As consequences, when it comes to the imaging modalities for behavioral experiments that attempt to reveal the interconnection between neural function and the external stimulus, the dimension of the imaging device should be taken into account. The implanted device should small enough so it will not obstruct the rodent's mobility. By doing so, the behavioral experiments can be performed under almost free moving conditions that resembling its natural environment.

1.2 Imaging Modalities for Behavioral Experiment

Fluorescence imaging is probably the contrast method that is most widely used for behavioral experiments because of its superior chemical specificity that leads to high-quality images of neural cells. This excellent specificity results from the selection of a particular fluorophore that has specific excitation and emission light. Various types of fluorescent markers are commercially available and can be used to observe the neuron cell activity during the behavioral experiment. By exploiting this superior detection specificity, three fluorescence imaging modalities for brain neuron cell observation have been developed so far: (1) optical fiber-based imaging, (2) miniaturized fluorescence microscopy, (3) implantable image sensor. Figure 1.2 shows the illustration of these imaging methods [7].

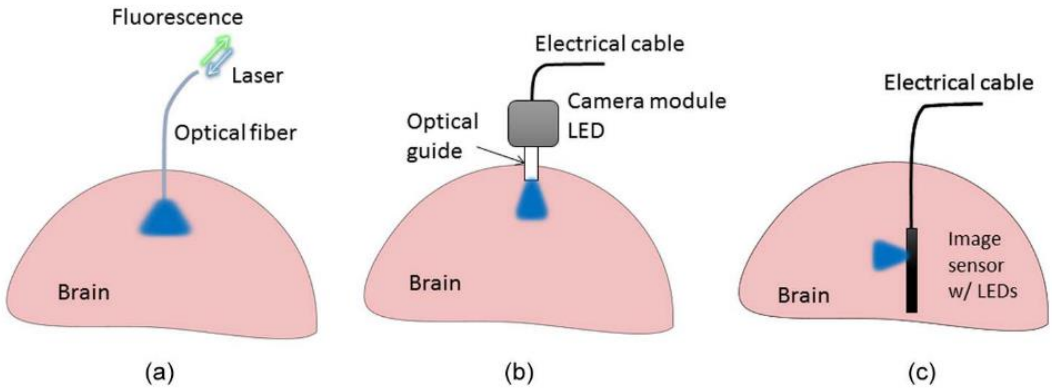

Figure 1.2 Three fluorescence imaging modalities for behavioral experiments
(a) Optical fiber transmitted excitations from the light source and emission from the target. A table-top fluorescence microscope typically controls both processes and yields a high-quality fluorescent image, (b) Miniaturized microscopy used an optical guide to reach the deep brain area. The mounted microscope captures the fluorescent image. A wire supplies the electricity for the image sensor and excitation light and sends the image to the external device. (c) Ultra-small image sensor and micro-LED excitation light were directly inserted in the deep brain area and captured the fluorescent image. The captured image travel electrically via wire to the external circuit for the next stage of the image processing [7].

1.2.1 Optical Fiber-Probe Microscope

The first category is a typical conventional epifluorescence microscope that uses optical fiber as a light guide for accessing a deep brain area. Inserting a standard optical fiber to the brain will not cause significant damages to the brain. The microscope is assigned separately from the observation target and sends the excitation light into the rodent's brain and receiving the light emitted out of it via optical fiber. This fiber-probe imaging system generates a high spatial resolution image capable of observing the individual cells corresponding with the fluorescence microscope specification used in the experiment. Another benefit of fluorescence imaging with a fiber-probe is the possibility to exploit the multimode optical fiber, which

provides the various delivering light modes in a single probe, in realizing a high-resolution endoscopic system in the deep brain region [14]–[16].

The fiber-probe imaging device does not harm the mouse's brain as its diameter is commonly less than 125 μm. By having a small dimension and low invasiveness, this fiber-probe platform can be used to perform a parallel multisite optical dynamic brain interrogation in freely moving animals. Doronina-Amitonova *et al.* utilized a fiber-probe microscope to interrogate the ipsilateral and contralateral hemisphere region in response to a tactile stimulation simultaneously. An epifluorescence microscope delivers the excitation light and receives the GFP emission light from the brain tissue through the fiber-probe (Figure 1.3 (a)). A multisite experiment of two different mouse's brain regions utilized two optical fiber mounted on its head (inset of Figure 1.3 (b)). During the unilateral whisker stimulation, the eGFP fluorescence signal of the contralateral (red circles) is growing in comparison with ipsilateral. This result is comparable with the *in vitro immunohistochemical* studies performed by Mack *et al*. (1992), which reported that the sensory information from whiskers is to be processed by the contralateral hemisphere ofsomatosensory cortex [17], [18].

However, utilizing the optical-probe fluorescence imaging system in particular behavioral experiments is challenging. Mounting an optical fiber—which is more rigid and fragile than wire—on the rodent's head has decreased the rodent's mobility. Thus, this imaging system can only perform a non-intense moving behavioral experiment, such as feeding and whisker stimulation, as mentioned before. In addition to its limited mobility, the fiber-based imaging system also has an inherent drawback in the form of a finite field-of-view. The imaging area is very dependent on the dimension of optical fiber.

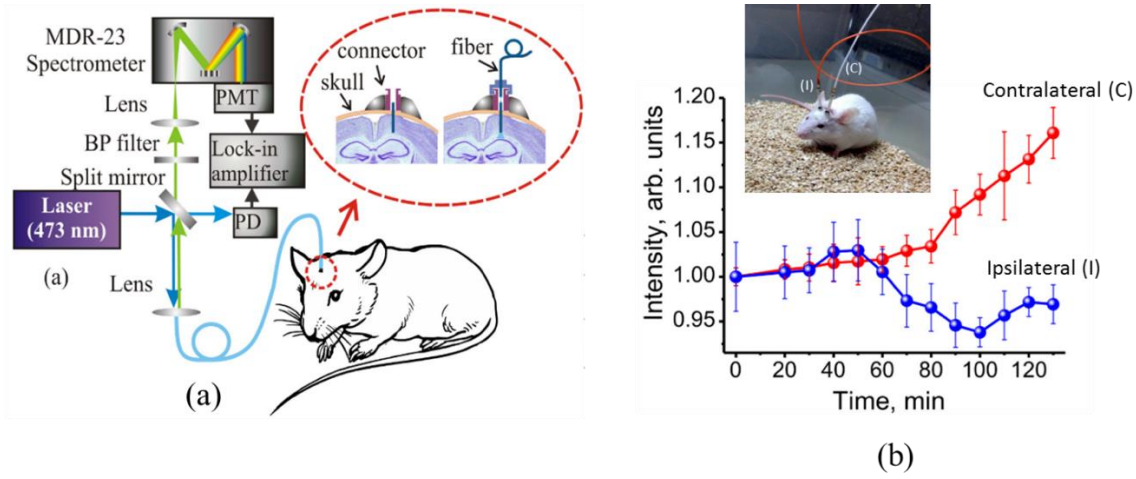

Figure 1.3 Fiber-probe microscope for multisite neural activity interrogation in a freely moving mouse.
(a) Schematic of the epifluorescence microscope that utilized the optical fiber-probe to reach the deep brain region of the mouse. Both excitation and emission light travel through the optical fiber. The inset figure shows the fiber-optic interface in the mouse's head. (b) Fluorescence response from eGFP measured simultaneously for an ipsilateral (blue circles) and a contralateral (red circles) hemisphere following a tactile whisker stimulation. During the stimulus, the contralateral area emitted a higher fluorescence emission than the ipsilateral, which confirmed the connection between whisker and contralateral connection [17].

1.2.2 Miniaturized Microscopy

The miniaturized microscopy means reducing the lens-based fluorescence microscope into a mountable size that does not limit rodent's physical activity [19], [20]. Thanks to the advancement in semiconductor and optical manufacture, this miniaturized microscopy can weight up to 1.9 g [19]. The University of California, Los Angles (UCLA), has developed another type of open-source midget microscopy called "Miniscope," which is a little bit larger (about 2.6 g in weight) [21]. Figure 1.4 (a) shows the mice with the Miniscope mounted in its head. Looking to its cross-sectional structure as seen in Figure 1.4 (b), the miniaturized microscopy has similar arrangements with the table-top fluorescence microscopy with a LED excitation light source, emission filter, lens, dichroic mirror, and CMOS imager.

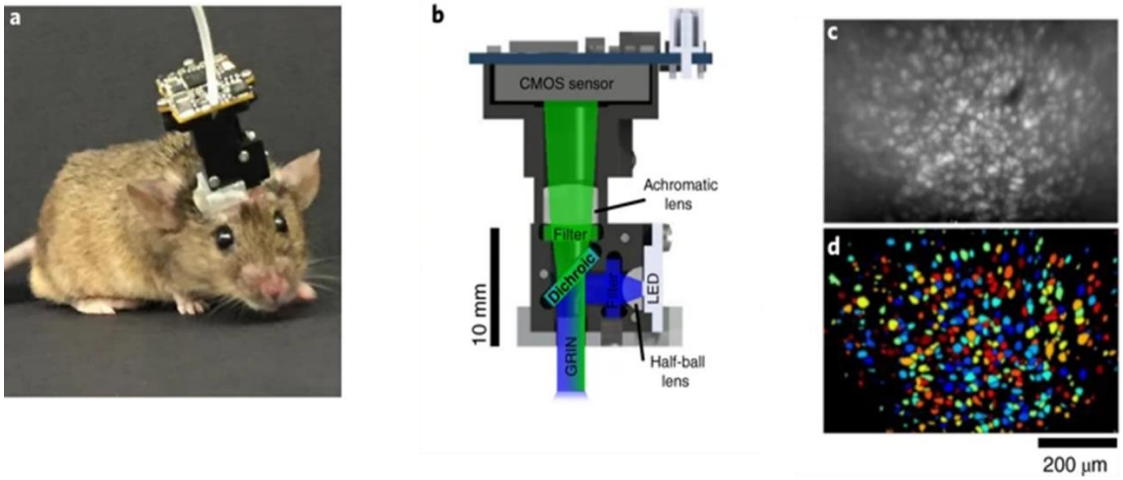

Figure 1.4 Open-source miniaturized microscopy UCLA Miniscope
(a) A mouse with a head-mounted Miniscope ready for the behavioral experiment. (b) The structure of Miniscope comprises CMOS sensor, lens, dichroic mirror, LED excitation light (blue path), and emission light (green path) passes through a GRIN lens. (c) Fluorescent image is recorded from hippocampal CA1 pyramidal neurons and (d) its corresponding spatial footprints of the identified neurons [21].

Since the imaging structure is similar to lens-based fluorescence microscopy, this imaging device has a high spatial resolution. It can distinguish the individual cells' fluorescence emission as s seen in Figure 1.4 (c) and (d). Moreover, by introducing a GRIN lens-probe rather than the conventional optical fiber to reach the deep brain area, the field-of-view of midget microscopy is very much improved than the fiber-probe fluorescence imaging.

Most of the excitation light used in this midget microscopy is LEDs owing to a small dimension and easy to integrates with other CMOS circuits. Yet, another group developed that so-called laser speckle contrast imaging (LSCI) method by utilizing laser excitation light via optical fiber. However, this additional optical fiber has escalated the weight up to 7 g and limited the rodent mobility [22].

Notwithstanding with capability to be mounted in a rodent's head, the midget microscopy is still too heavy for a very intense moving condition in a behavioral experiment like running

and swimming. The tiniest fabricated microscopy is 10% of the weight of a typical mouse. Also, it is impossible to perform a multisite experiment that is essential in revealing the different brain region relationships using this microscopy. As seen in Figure 1.4 (a), a single imaging device had already occupied the rodent's head.

1.2.3 Implantable CMOS Image sensor

In an effort to resemble a freely moving animal in natural conditions, an implantable CMOS image sensor is a promising imaging modality because of its measly physical embodiments [23]. The absence of optical components in this system has significantly reduced the system's size. For the implanted device, an inevitable trade-off exists between field-of-view and invasiveness features. Practically, it is difficult to establish a proper value of the area detection and low invasiveness simultaneously. Therefore, the image sensor is designed according to the type and area of target detections.

The examples include planar-type imaging devices that are placed on the brain surface to observe a blood flow [24] and hemodynamic response [25], [26]. This planar sensor does not require the low invasiveness as it is assigned on the brain surface. Thus, its CMOS image sensor contains more pixel number for a wide field-of-view and several excitation LEDs. Even with a planar structure, the implantable CMOS image sensor's dimension remains small and lightweight so that it accommodated for two different brain areas implantation. This multisite detection is essential in understanding the behavioral, which is mostly embroiling complex processes from various brain areas rather than from a single site. Figure 1.5 shows the planar-image sensor utilized for a multisite experiment in the mouse's brain surface (left and right side) in the response of the optical stimulus from the eye.

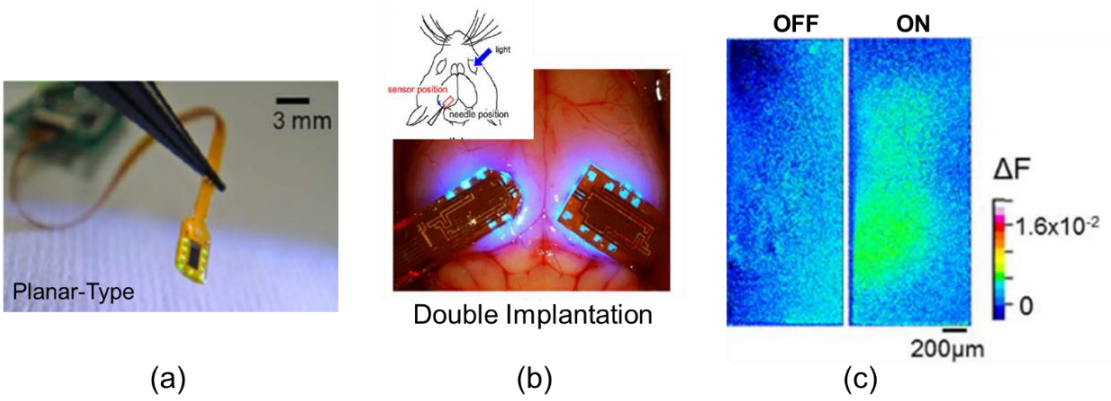

Figure 1.5 Planar CMOS image sensor for a brain surface observation
(a) A small planar-type implantable device comprises a CMOS image sensor and LED excitation light. (b) Photograph of two planar sensors on the left and right visual cortex of the mouse brain. The LED excited the brain surface, and the image sensor perceived the GFP emission from the brain. (c) The fluorescent image in a pseudocolor representation shows responses in the visual cortex arise (ON) in response to the light stimulation to the eye [15].

In contrast, the needle-type sensor that is intended for the deep brain region sighting has a delicate and taper structure for low invasiveness features. This needle-type sensor has been used to measures the protease activities by artificially inducing epilepsy in the mouse's abdomen [7], observes the nicotine's effect to dopamine (DA) neurons in the ventral tegmental area (VTA) rats [27], and for the optical theranostic applications in a deep tissue [28].

One of the challenging parts of an implantable fluorescence CMOS sensor is achieving a high spatial resolution and contrast image. The undirected fluorescence emission, which declines faster as a distance function from the target than its excitation counterpart, leads to low signal-to-background levels. Moreover, the fluorescence emission is incoherent, and thus incompatible with any image processing method based on the source-shifting technique, such as holographic digital reconstruction and related super-resolution techniques [29].

From the hardware standpoint, the emission filter of the lensless imaging system has a poor rejection performance due to the absence of an objective lens that collects the scattered ray components from the sample as in the lens-based device. The high angled scattered light is

problematic for a typical interference filter as it will pass through the multilayer structure produced that so-called "*Blue Shifting*." Another type of emission filter is an absorption filter. Aside from its straightforward in use, the absorption filter has advantages for its independent spectral response from the angled incident light. However, a thicker absorption filter layer is required to absorb the scattered excitation light from the objects, which expense the spatial resolution degradation due to the increasing distance from objects to the image sensor. Also, under immense excitation light, the absorption filter generates autofluorescence that will reduce the background image contrast.

A recently developed hybrid emission filter for lensless setup comprises an interference filter, and an absorption filter via a fiber optic plate (FOP) exhibited a high-performance excitation light rejection ratio of approximately 10^8:1 at a wavelength of 450 nm [19], [20]. Notwithstanding this accomplishment, the FOP that plays as a substrate for the interference filter and to protect the absorption filter surface from scratch has escalated the device thickness into the millimeter range. Thus, this solid hybrid filter structure is not suitable for an implantable imaging system, particularly to observes the neuron cells in the deep brain region. One way in assigning the hybrid filter and image sensors for in vivo experiment is to separate the filter from its substrate and then deposits merely the filter on the CMOS sensor.

1.3 Purpose of this Research

This thesis comprises work in fabricating and evaluating the thin composite filter constructed on implantable lensless fluorescent imager for deep brain neuron cell observation. The composite filter, which contains a short-pass interference filter and absorption filters, generated a band-pass transmission spectrum close to a green fluorescent protein (GFP) as the target emission detection. I proposed two methods of transferring a filter from its substrate to

the image sensor: laser lift-off (LLO) that relies on laser ablation and plasma etching that uses a chemical etching reaction.

The filter evaluation discloses the yield-rate of both fabrication methods in materializing the thin composite filter through physical and optical filter examination. The imaging performance of the assembled filter and image sensor was evaluated by perceiving the microsphere fluorescence emission and then calculating the spatial resolution. Once the spatial resolution was obtained, the fabricated device entered in vitro experiment to identify the GFP emission from the genetically modified brain slice. The blue laser was selected as excitation light for its narrow spectrum that benefits in exciting the GFP excitation without emitting the green light as exhibited in typical LEDs. The laser excitation was coupled to the optical fiber for gaining a controllable illumination direction.

The organization of this thesis is: **Section 2** introduces the background knowledge of the implantable image sensor started from a basic of CMOS sensor structure and its detection mechanism. I also briefly shows our previous device for the GFP detection and the pros and cons of a typical emission filter for lensless fluorescence microscopy. At the end of this section, I explain the schematic of the proposed image sensor covering its thin composite filter structure and fiber-coupled laser excitation. **Section 3** discusses the concept and mechanism of filter separation used to fabricate a thin composite filter started by laser lift-off (LLO) and then followed by a plasma etching method. **Section 4** provides a filter evaluation for both LLO and plasma etching methods. For LLO, the assessment includes the physical and optical properties of the filter after separation and imaging quality of the fabricated device. While for plasma etching, evaluation only for physical properties to check the capability in yielding a large and uniform emission filter and the spectral response of band-pass filter after the etching process. Finally, **Section 5** summarizes the results, and I also present a short outlook.

2 Implantable CMOS Fluorescence Imager

Implantable fluorescence device combines the selectivity of fluorescence technique and the advancement of CMOS technology in providing ultra-small imager yet contains many pixels for achieving wide field-of-view. Over the years, researchers have devoted considerable attention to implementing this low-invasive imaging modality for behavioral experiments, revealing the brain function by observing the dynamic of neuron cells corresponding with the particular activities.

This chapter briefly introduces the essential component of the proposed implantable fluorescence micro-imager, includes CMOS image sensor structure as the central imaging function, a brief explanation of a well-known biological marker in a behavioral experiment: GFP, followed by our previous implantable fluorescent imager for GFP detection, state-of-the-art emission filter for lens-free setup, and utilization of composite emission filter and laser excitation light.

2.1 CMOS Image Sensor

The first generation of complementary-metal-oxide-semiconductor (CMOS) image sensor, which was introduced in the mid-1960s, was MOS diodes-based. Yet, this CMOS version has not entered commercial production because of its poor performance and large pixel size at that time. Almost at the same period, George Smith and Willard Boyle at Bell Labs invented a different type of solid-state imaging device, charge-coupled devices (CCDs). The full analog CCDs had successfully embraced the market owing to their superior dynamic range, lower fixed-pattern noise (FPN), smaller pixels, and higher sensitivity to light [30]. Yet, the story does not end in such ways. In the early 1990s, the improved CMOS image sensor re-emerged as a

vision sensor technology pioneered by universities and small companies; even the image quality was still not as good as CCDs. Thanks to the CMOS technology advancement, since then, CMOS image sensors have been developed progressively, and the current version based on active pixel sensor (APS) is becoming the dominant player replacing the incumbent image-sensing technology, CCDs [31].

The essential properties that justify the expeditious advancements of CMOS sensors over CCDs are large-scale functional integration and low-voltage operation. CMOS image sensors exploit almost the same silicon chip technology used in microprocessor systems with some supplementary process, e.g., pinned photodiodes. Thus, it is possible to integrate CMOS sensors with the functional circuit to improve the performance and even realizing a smart CMOS sensor with versatile functionality. In addition, like CMOS integrated circuits, CMOS image sensors operate at considerably lower voltages than CCDs, typically between 1.8 and 5 V. Low-voltage operation corresponds with low power consumption. The easiness in integration and low power consumption features are desirable in consumer markets that demand compactness, long battery life, and low production cost [32].

To date, CMOS image sensors pervade almost all aspects of modern imaging applications includes consumer electronics (digital camera, smartphone-based camera, camcorder, etc.), automotive, security and surveillance, robotic vision, etc. Come with wide dynamic range, high speed, and high sensitivity, CMOS image sensors have extended to outlandish research areas, biotechnology, and biomedicine [33]. In a few key areas of biomedical research, the CMOS sensor is becoming indispensable elements in behavioral experiments [27], [34]–[36], cell imaging [37]–[40], point-of-care diagnostics [41]–[44], etc. Specifically, for behavioral experiments, as explained in Section 1.2, several CMOS-based micro-imaging modalities have been developed in the form of miniaturized microscopy, optical-fiber based, and implantable

imager. In the next subsection, I briefly explain implantable CMOS imagers for a behavioral experiment that has been developed by our laboratory so far.

2.2 Our Previous Implantable Fluorescent Imager

In a behavioral experiment, which relies on imaging cells activity in a living organism, a green fluorescent protein (GFP) is the most widely used biological marker [45] owing to its well-known stability and easiness insertion to the protein without altering the location and function of host-protein [46]. GFP insertion encoded host-protein to mark the expression of the molecular or cellular events explicitly. For instance, researchers mapped the transgenic mouse brain using a different type of GFP [47], [48]. On the other hand, the GFP can be used for visualizing experimental tumors, inflammation, and wound-healing [49], and observing dopamine in the central nervous system for addictive behaviors [50]. Another example of GFP application is for tagging the channelrhodopsin (ChR2) in optogenetic applications [51].

One of the essential green fluorescent indicator protein that enables reliable measurement of synaptic calcium signals (Ca^{2+})-probe is GCaMP, which is initially developed by Nakai *et al*. at the end of 2000. The unique properties of GCaMP are its high signal-to-noise and significant fluorescence emission corresponding to the presence of Ca^{2+} in the environment. The Ca^{2+} binding mechanism, as mentioned in their paper, is "When Ca^{2+} binds to CaM, conformational changes due to the Ca^{2+}–CaM–M13 interaction induce a subsequent conformational change in cpEGFP so that the fluorescence intensity changes" [52]. The first transgenic mouse genetically modified by the GCaMP was reported to examine the postsynaptic signaling in smooth muscle [53]. Since then, the various type of GCaMP has been developed for a better detection capability [54]–[56].

Our previous work demonstrated the possibility of detection GFP emission *in vivo* using a micro-imaging device implanted on the mouse head under freely moving conditions. This experiment utilized the needle-type sensor that benefits in low invasive features to reach the amygdala area for acute restraint stress behavioral observation [7]. A similar needle-type was also used to monitor the neural activities in the ventral tegmental area (VTA) in the deep brain region in response to the nicotine intake simultaneously. The image sensor perceived the different excitation dopamine (DA) in correspond with the nicotine assignment [27]. Figure 2.1 shows the fluorescent imager used for DA observation in the VTA region.

The fabricated needle-type sensor has a small dimension to keep the low invasive feature (Figure 2.1 (a)). From the schematic shown in Figure 2.1 (b), the implantable device comprises the CMOS image sensor, blue LEDs excitation light, and fluorescence filter to enhance the GFP emission selectivity. All components were assembled on the flexible substrate to circumvent the rigidity that can lead to a device's fracture during the implantation. Figure 2.1 (c) shows the photograph of the imaging device mounted on the rat's head. The time-lapse fluorescence monitoring, as shown in Figure 2.1 (d), indicate the difference DA on VTA region excitation after being administrated by the various nicotine concentration. The needle-sensor perceived the aggregate GFP emission from the neuron colony in corresponding with the nicotine intake. Neuron cell activities in the VTA region are raised as the number of nicotine intake is increasing. However, the fabricated device unable to distinguish the GFP emission from individual cells as the spatial resolution is 22.3 μm.

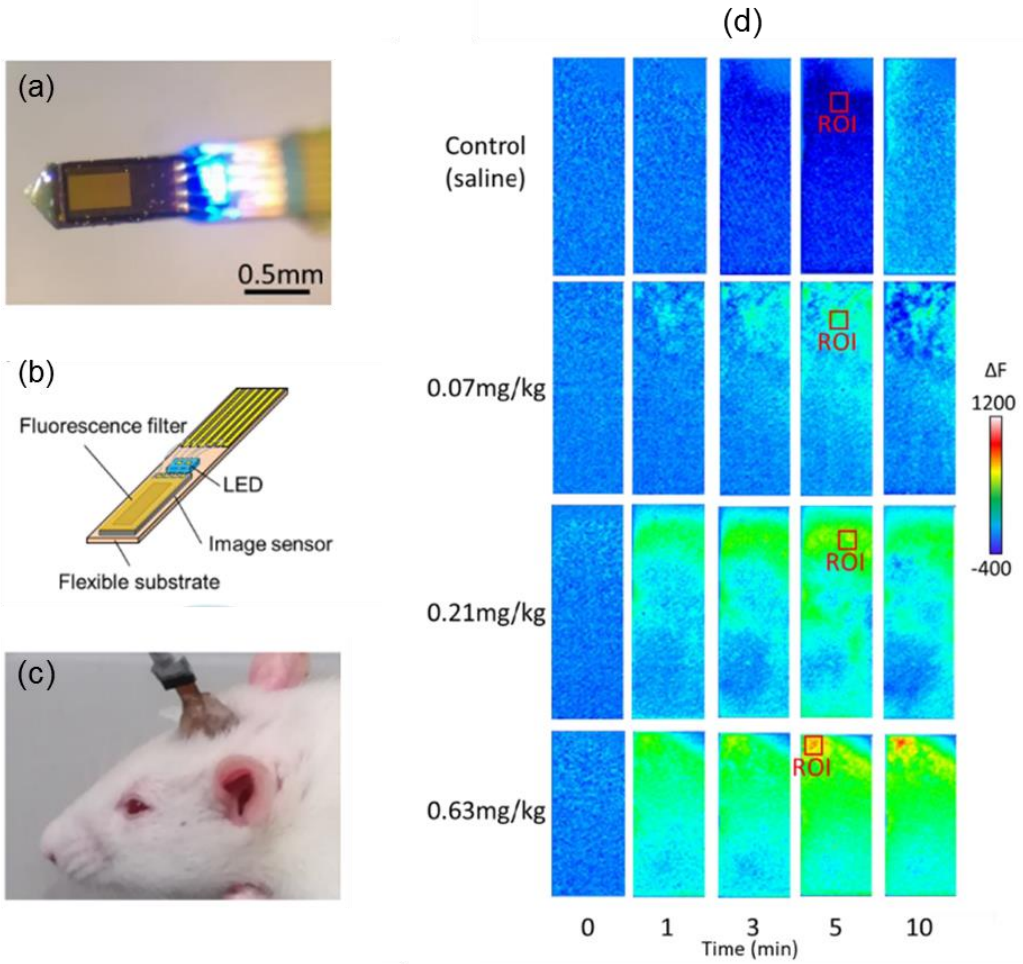

Figure 2.1 Fluorescent imager for Dopamine (DA) observation on VTA region
(a) Photograph of the fabricated needle-type sensor integrated with blue excitation light. (b) The schematic of the implantable device comprises an image sensor, fluorescence filter, and LED light source. All components were attached to the flexible substrate. (c) Fluorescence imager mounted on the rat's head (d) Time-lapse fluorescence images of the rat's VTA administrated with various nicotine concentrations from 0.07 mg/kg to 0.63 mg/kg compared with control [27].

In light of the low invasive feature to reach the deep brain area of rodent's brains, in this research, we designed needle-type image sensors, which contain 40 × 400 pixels. The foundry then fabricated these needle sensors using 0.35-μm 2-poly 4-metal standard CMOS technology

of Austria Mikro Systeme (AMS). The final chip dimension is 500 μm width, 5100 μm length, and 150 μm thickness, as seen in Figure 2.2 (b).

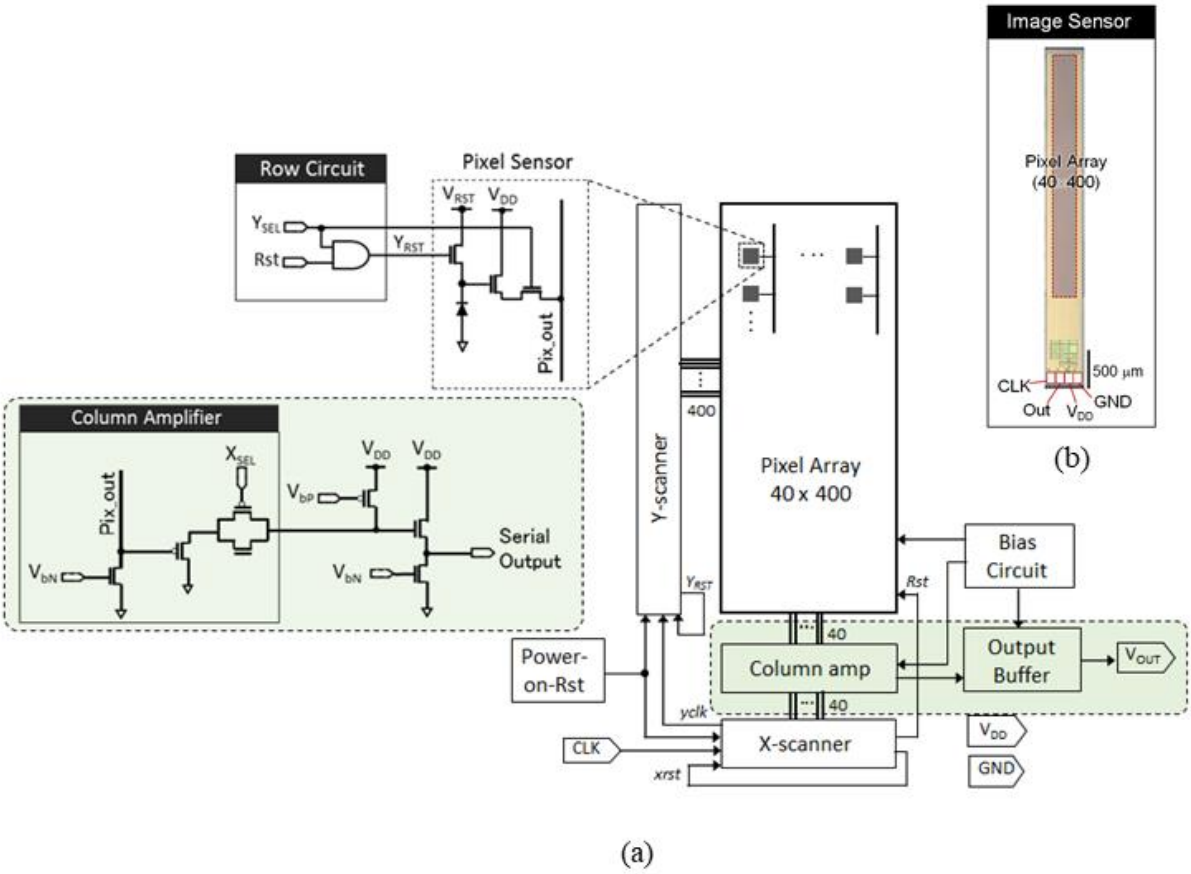

Figure 2.2 CMOS image sensor circuitry.
(a) Schematic diagram of the needle-type CMOS image sensor that comprises pixel array based on three-transistor active pixel sensor (3-Tr APS) structure, Y-scanner for row selectivity, column amplifier and output buffer circuit, and X-scanner for column addressing. (b) Microphotograph of the CMOS needle sensor with the four pads connector (V_{DD}, GND, CLK, and V_{OUT}).

Figure 2.2 (a) depicts the schematic circuit of a needle CMOS sensor. It comprises a 40 × 400 active pixel array, control circuitry for selecting the pixels via a *Y-scanne*r (row) at the left-

side, and column amplifier and *X-scanner* at the bottom of the pixel array. Bias circuit and power-on-reset are supporting circuitry for the imaging process. For the imaging function, we used a pixel array with a size of 7.5 μm × 7.5 μm/pixels to provide sufficient spatial resolution for imaging the colony of the brain neural cell. This pixel utilizes a three-transistor active pixel sensor (3-Tr APS) for transducing the optical to an electrical voltage. As seen in the pixel sensor schematic, 3-Tr APS comprises a photodetector and three transistors for switching and a source follower circuit.

The operation of an APS is as follows. At the beginning of detection, the photodiode (PD) is reset by sending the Y_{RST} command activating the switch. This action forced the PD to a specific voltage level. Next, the integration period started by turned off the Y_{RST} transistor, which makes PD is electrically floated. During this period, the incident light produces carriers and accumulated in the PD junction capacitance; the voltage of PD decreases proportionally to the input light intensity. Thus, by measuring the voltage drop, we can calculate the total incident light. After an accumulation of time, the Y_{SEL} turned on the switch and then transferred the PD levels of selected pixels to the vertical output line, *Pix_out*. After the voltage reading process, the Y_{RST} is off and then repeats a similar approach for the next pixel.

The operational sequence of the pixel selectivity relies on the *Y-scanner* for selecting the light-sensing rows one-by-one. Every pixel in the selected rows connects to the column circuitry, which comprises the source follower circuit and column selecting transistor switch, X_{SEL}, via each column signal line. The column amplifier output and the buffer circuit maintains the signal before sending it out to the next data processing stage. For this data communication and electrical function, the image sensor has four pads connectors, V_{DD}, *GND*, *CLK*, and V_{OUT}, as seen in Figure 2.2(b). Table 2-1 shows the image sensor specifications.

Aside from the needle-type sensor I have explained above, we also designed a planar-type image sensor contains 120 × 268 pixels. This image sensor is three times wider yet about a half shorter than the needle-type sensor. Despite the pixel number differences, the planar type uses the same fabrication process based on AMS technology; the imaging mechanism relies on 3-Tr APS and the similar concept of pixel scanning and data transfer to the external circuit with the needle-type. Practically, researchers use this planar-type sensor for brain surface observation that requires a wide field-of-view without concerning the invasiveness. In this work, I used a planar sensor to evaluate the capability of various filter fabrication methods, as explained in the Filter Fabrication section.

Table 2-1 Specifications of the image sensor

Process technology	0.35-μm 2-poly 4-metal standard CMOS process
Supply voltage (V)	3.3
Chip size (μm^2)	500 × 5100
Pixel type	3-transistor active pixel sensor
Pixel size (μm^2)	7.5 × 7.5
Pixel array size	40 × 400
Photodiode type	Nwell-Psub

Bringing CMOS technology to fluorescence imaging, particularly in the lens-free setup, need to consider one essential key: detection selectivity. As explained before, the CMOS image sensor detection mechanism relies on Si-photodiode, which has broad-spectrum detection ranging from ultraviolet to infrared region. In contrast, fluorescence imaging detects

a specific range from the observation target emission. Therefore, adding the selectivity feature to the CMOS fluorescence device is compulsory. One of the most common methods to improve the selectivity is applying an emission filter—absorption or interference filter type—on the surface of the CMOS image sensor. In the next section, I briefly discuss the commonly used emission filter in CMOS-based imaging systems. It will cover the concept of fluorescence detection, followed by the pros and cons of each filter, and ended by the explanation of a composite filter equipped with laser excitation for the proposed implantable device.

2.3 Emission Filters for Fluorescence Detection

2.3.1 Fluorescence Detection

For the fluorescence imaging system, an emission filter is a crucial component in separating the excitation light from the fluorescence emission. The filter separation is essential because the excitation light is typically brighter than the fluorescence signal, in the order of magnitude about 10^{-4} to 10^{-6} of the excitation light [57]. The emission filter significantly reduces the excitation light entering the detector while allowing passes as much of the emission photon as possible.

Figure 2.3 illustrates the relationship between the emission filter and the spectrum of a typical fluorophore. This material absorbs light in one range of wavelengths and re-emit the longer wavelength fluorescence light. The excitation spectrum has a peak at λ_{ex}, and the emission spectrum has a maximum at λ_{em}. The distance between λ_{ex} and λ_{em} defines that so-called the *Stokes Shift*. *Stokes Shift* can be as small as 10 nm or as large as 150 nm, depending on the fluorophore [58].

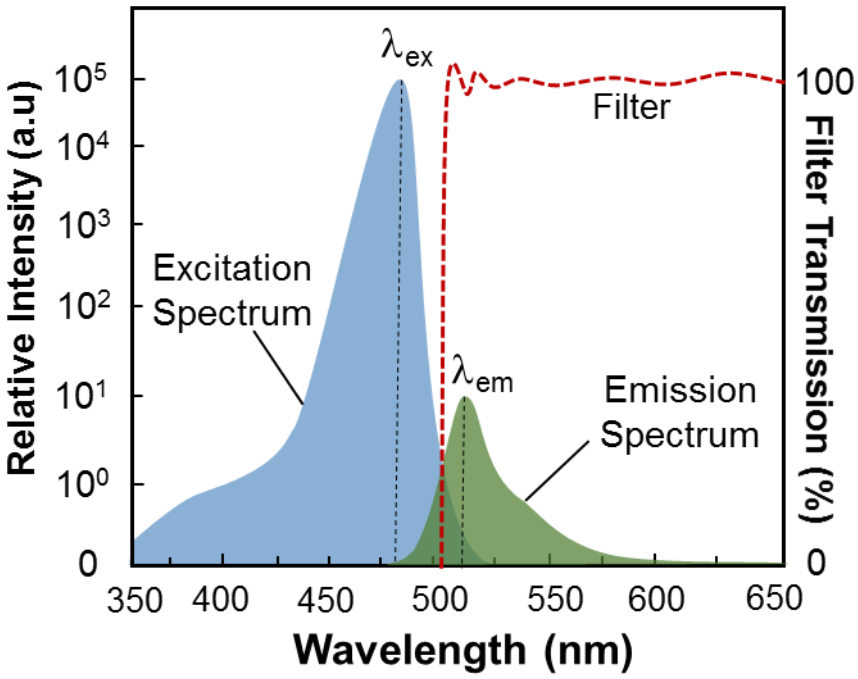

Figure 2.3 Relation of the fluorophore, excitation source, and emission filter.
The relative intensity of the typical spectrum of the fluorophore is the excitation (left) and emission (right), in arbitrary units. The distance between excitation peaks, λ_{ex}, and emission peaks, λ_{em}, is called *Stoke Shifts*. The emission filter (dashed line) must transmit the emitted fluorescent light and reject the excitation light [58].

Suppose the fluorophore is excited at an out of peak excitation, the fluorescence spectrum is unchanged, but the amplitude emission is lower than if it is excited at λ_{ex} [59]. In general, the number of photons emitted is much smaller than the amount absorbed, reflecting the existence of non-radiative pathways for the decay of the fluorophore from its excited state. The ratio of the emitted to absorbed photons is the *quantum yield* of the fluorophore.

Four parameters that characterize optical filters are rejection levels in the stop-band (the wavelengths that are blocked), transmission levels in the passband (the wavelengths that are transmitted), and the location and sharpness of the transition between them, respectively known as the absorption edge and the absorption edge width. Ideally, the absorption edge should be

perfectly steep and located to the right of λ_{ex} and to the left of the entire emission spectrum. In reality, these levels are unattainable, and the stopband transitions to the passband span over several wavelengths.

2.3.2 State-of-the-art Art of Single Emission Filters

The earliest filter used for micro-imaging were interference filters. An interference filter comprises multiple thin layers of dielectric materials with different refractive indices stacked alternately. The advantages with interference filters are; they are compatible with integrated circuitry due to its standard and low-temperature fabrication process and easy to manage an arbitrary and very steep rejection band edge by changing layer arrangements. Also, since the filter reflects incident light in the stop-band, it almost absent from auto-fluorescence even in immensely excitation light illumination.

On the other hand, a disadvantage of interference filters is that the spectral response depends on the angle of incidence of the incoming light, as illustrated in Figure 2.4. This spectral response shifting resulted from different light paths traveling in the multilayer filter in response to the increase of angle of incidence (AOI) light. As seen in Figure 2.4 (a), when the light reaches the filter in a normal incident angle (0° AOI), the light traveled in the exact distance with the filter thickness *x*, which is traditionally designed $\lambda/4$ of the wavelength rejection band.

As the AOI on an interference filter increases, the optical path length through the filter layers increases, which causes the cut-on and cut-off wavelengths to decrease. As a result, the spectral shifted to a shorter wavelength that is so-called "*Blue Shifting*" (Figure 2.4 (b)). The effect of oblique light not only moved the filter spectral to a shorter region but also shallowed the slope, which decreases the filter selectivity. Chediak *et al.* reported that the spectrum edge

of distributed Bragg reflectors (DBRs) could shift by as much as 80 nm as the incidence angle is varied from 0° to 50° [60].

The spectral shifting almost does not emerge in the lens-based fluorescence imaging because the emission from a sample is collimated by the objective lens and then reaches the interference filter in a normal incidence angle. In contrast, for the lensless imaging devices, this angle dependence is becoming a significant drawback due to its sample close proximity to the sensor array (<100 μm) and the absence of light collimation process from the lens. Thus, the scattered light from the sample, which is mostly in the angled direction, passes through the interference filter and reaches the image sensor [61].

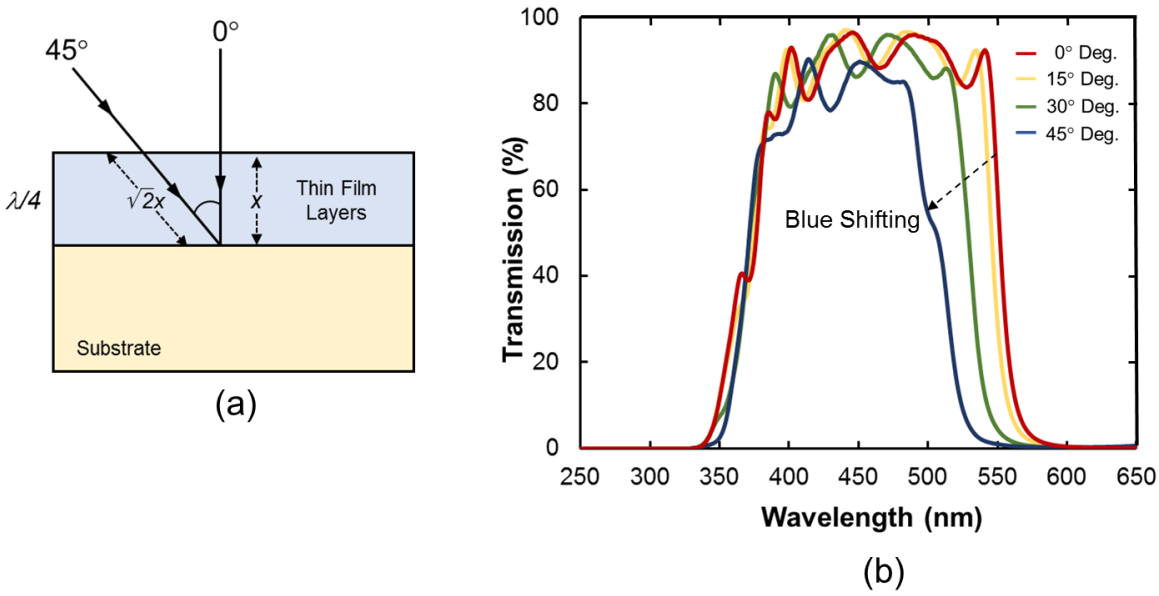

Figure 2.4 Blue shifting of interference filter in a high angle of incidence (AOI)
(a) Schematic of the incoming light path on the thin film layer of the interference filter. In a normal angle of incidence (0° AOI), light travel at *x* distance, which is associated λ/4 of defined wavelength rejection, and it is reflected. In contrast, in an angled incident (45° AOI), light travel in a longer path than *x*, and it is not reflected instead passes to the substrate. In this circumstance, the band-edge transmission spectrum filter shifted to a shorter wavelength that is so-called "*Blue Shifting*," as seen in a short-pass interference filter (b). The high AOI also shallowed the steep cut-off band.

From the manufacturer's standpoint, another disadvantage of the interference filter is stringent in layer thickness for a specific rejection band. A variation of a few nanometers in the width of the layers can cause significant errors in the cutoff wavelength, which can reach ± 50 nm [58]. Also, in correspondence with the existing fabrication method, the high-performance interference filter can only be deposited on a rigid and stable substrate such as glass, sapphire, and silicon. Integrating the filter directly on the CMOS image sensor requires a complicated process to compensate for the materials mismatches. To date, several researchers had used the interference filter for their lens-free fluorescence imaging device [61]–[63].

Absorption filters are an alternative to interference filters. These filters have high absorption at the excitation wavelength and low absorption at the emission wavelength. They followed by Beer-Lambert law for liquids; $I = I_0 e^{-\alpha x}$, where I is the intensity of the light after the filter, I_0 is the intensity of the incident light, α is the absorption coefficient, a wavelength-dependent constant, and x the filter thickness. The advantages with the absorption filter is a more straightforward fabrication than for interference filters since it requires only a single layer and no tight layer thickness tolerances. Another advantage is that, unlike interference filters, the spectral response of the filters is independent of the angle of incidence. Also, since the filter absorbs almost all the light, there is no scattered component light from the filter reflection that may decrease the image contrast. Owing to these merits, absorption has been widely used for lens-free fluorescence imaging over the years [7], [28], [39], [58], [61], [64]–[66].

A disadvantage of absorption filters is their limited spectral response customizability, which depends on the fluorophore characteristics, compared with the interference filter. Also, a pigment-based or dye absorption filters have a moderately steep edge, which can be problematic for a fluorophore with very short *Stoke Shift*. Moreover, in intense excitation illumination,

increasing the absorption filter thickness not only degrades the achievable spatial resolution [29] but also image quality because of auto-fluorescence produced by the filter [67].

2.3.3 Composite Emission Filter

In the quest of a decent emission filter for a lens-free fluorescence imaging device, a hybrid structure of absorption filter and interference filter offers promising results. Richard *et al.* (2009) reported that the hybrid filter structure compensated each filter drawback in the ways that the interference filter tightens the pass-band spectrum profile while the absorption filter makes the system independent of the incidence angle. The total rejection ratio of the hybrid filter is 43 dB at 530 nm (excitation) and ~2 dB at 650 nm (emission) with a total thickness of 2.8 μm and a roll-off (edge bandwidth) of ~100 nm. The schematic of the hybrid filter and its spectral response in comparison with a single emission filter is shown in Figure 2.5 [68].

It is important to note that since the absorption filter deposited on the interference layer and directly contacted the microfluidic channel as a detection area, the absorption filter received much excitation light intensity and tend to generate auto-fluorescence. According to Figure Figure 2.5 (b), this auto-fluorescence light operated in the same region with the transmission spectrum interference filter, and it thus passed the interference filter and reached the photodiode. On some level, the presence of auto-fluorescence degraded the image contrast. Therefore, the absorption filters for this hybrid filter structures require more stringent criteria that are not only must have a pass-band associated with the target detection emission but also produce low auto-fluorescence emission at the same time.

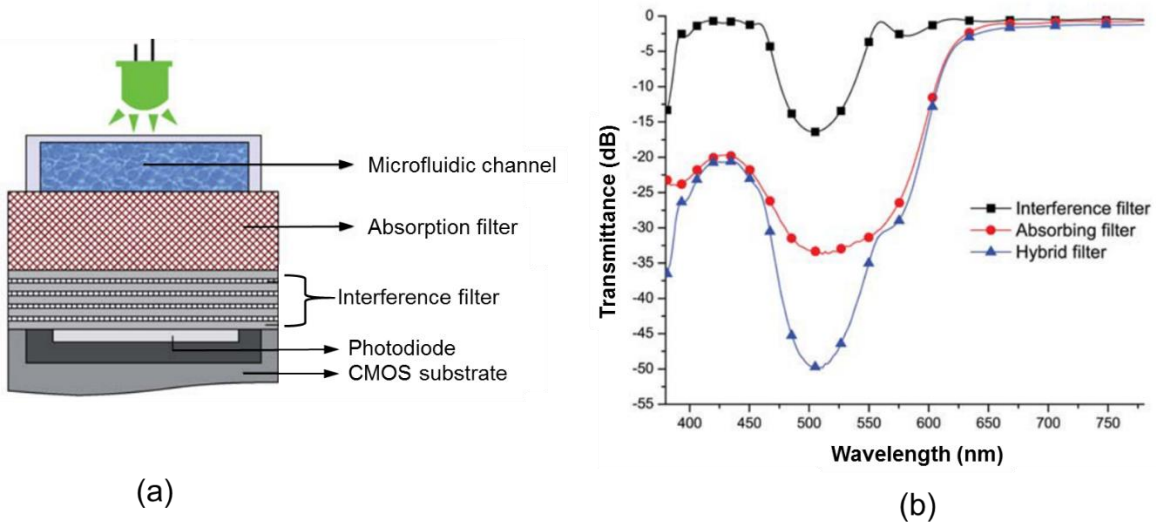

Figure 2.5 Hybrid filter integrated with the microfluidic channel
(a) Schematic of hybrid filter on-chip integrated with the analytical device. The hybrid filter comprises an interference filter attached directly on the CMOS sensor and an absorption filter deposited on the interference filter beneath of the microfluidic channel. The complementary structure of the hybrid filter compensates for each drawback of a single filter (b) Spectral response of the hybrid filter compared to the single filter. The total rejection ratio at 532 nm is 43 dB [68].

To utterly liberate from auto-fluorescence drawbacks, Sasagawa *et al.* (2018) proposed a hybrid filter with different filter arrangements. In contrast with the previous composite filter structure, the interference filter was assigned in the uppermost layer and directly exposed to the excitation light, while the absorption filter was beneath the interference filter and directly contacted with the CMOS image sensor. A fiber optic plate (FOP) emerged between the interference filter and absorption filter to protect the absorption filter and maintains the spatial resolution.

Figure 2.6 shows the schematic of the new hybrid emission filter structure and its rejection ratio and image comparison with the single emission filter. From its structure, as seen in Figure 2.6 (a), the interference filter reflected most incoming excitation light without generating any auto-fluorescence. The angled scattered excitation light, which has a lower intensity than its

initial light, passed through the interference filter and is absorbed by the absorption filter before reach the CMOS detector.

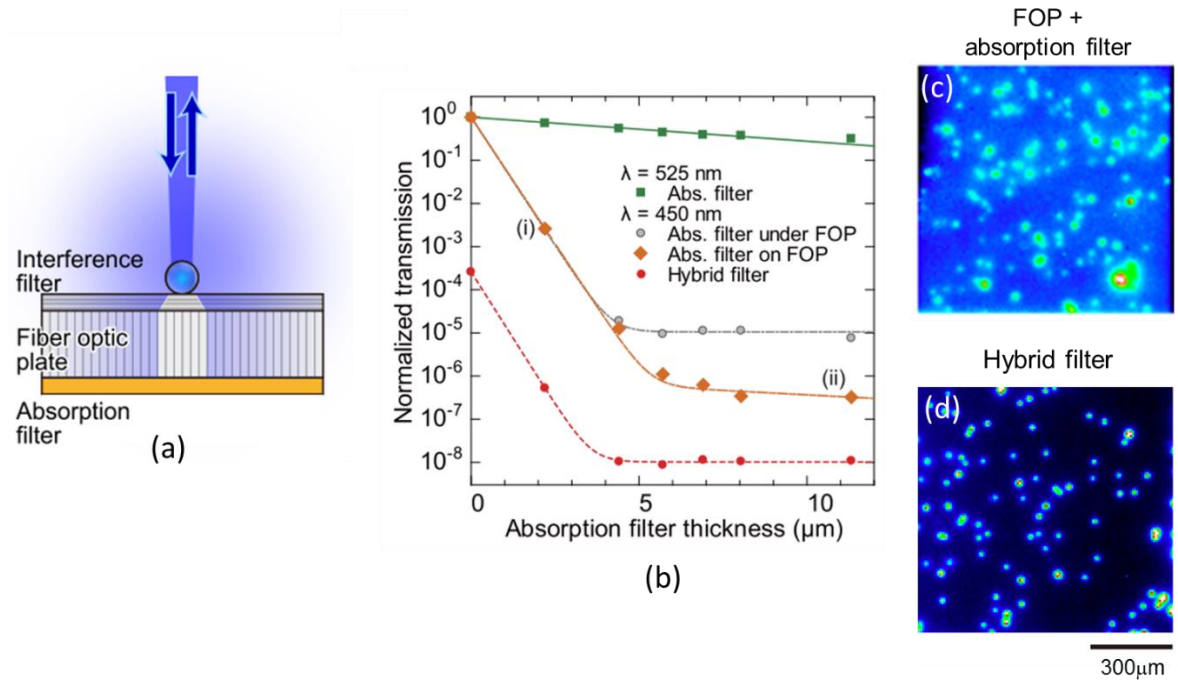

Figure 2.6 New hybrid filter structure and its imaging performance
(a) Schematic of a new hybrid filter comprises an interference filter in the top layer, a fiber optic plate (FOP) in the middle, and an absorption filter in the bottom layer. The interference filter reflects light in the normal incidence angle. The high-angle scattered light passed the interference filter and then is absorbed by the absorption filter. (b) Comparison of the emission filter transmission as a function of absorption filter thickness. The hybrid filter reduced the excitation filter at the lowest point 10^{-8} from its initial intensity. Compared to the fluorescent image from a single absorption filter (c), the hybrid filter shows a higher contrast fluorescent image (d) [67].

Imaging performance evaluation showed that the new hybrid structure filter exhibited a high excitation rejection of approximately 10^8:1 at 450 nm (Figure 2.6 (b)). This rejection number is comparable with the bulky-interference filter at the normal incidence angle. Spatial resolution examination using 2.5−4.5 μm microsphere showed the hybrid filter generated a

higher contrast image compared to a single absorption filter (Figure 2.6 (b)). The spatial resolution of this imaging device with a hybrid filter is 12 μm. By having the capability to produce high contrast and high spatial resolution image, this lens-free imaging system can identify individual HEK293 cells in a time-lapse imaging experiment [67].

Despite its superior rejection, the hybrid filter typically used a thick glass substrate to keep the interference filter structure. For instance, it can reach 2.5 mm thickness. Adapting a hybrid filter with its thick substrate to an implantable device is impossible as it destroys the animal's brain. Thus, the filter should be separated from its substrate and then applied to the CMOS sensor. However, constructing a thin hybrid filter on the image sensor is a demanding work in reality. The strategy on how to integrate the hybrid filter and implantable micro-imager is described in the Filter Fabrication section. Correspondingly, in the next subsection, I briefly discuss the detail of the hybrid filter structure used for implantable devices, followed by the utilization of blue laser excitation light for improving the rejection performance.

2.4 Composite Emission Filter and Laser Excitation

I designed the hybrid or composite filter to produce a band-pass transmission spectrum close to GFP emission as the target detection. As seen in Figure 2.7, the GFP has an excitation peak (λ_{ex}) at 488 nm and an emission peak (λ_{em}) at 507 nm. Since the *Stokes Shift* of GFP is very narrow, the emission filter should separate the excitation light from the emission precisely. In this situation, the trade-off between selectivity and intensity exists. Placing the emission filter at GFP emission peak (λ_{em}) results in the highest detection of emission intensity. Yet, it jeopardizes the separation capability as it is too close to the excitation region. Thus, for an excellent emission detection, two important points should be considered: (a) steep pass-band spectrum of emission filter, and (b) narrow spectrum of excitation light. By selecting a narrow

spectrum of excitation light, even if its spectrum is matching with the peak excitation (λ_{ex}), its excitation spectrum would not reach the emission area.

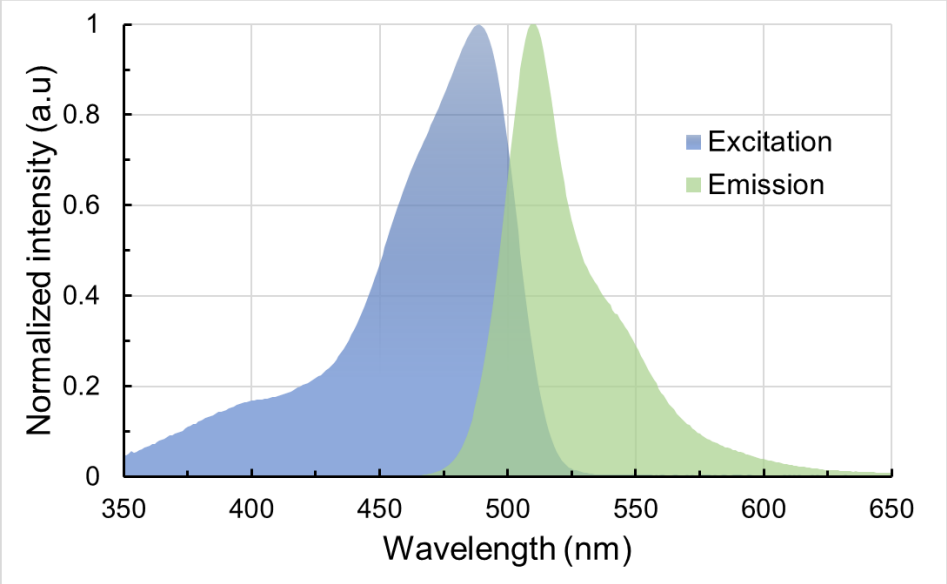

Figure 2.7 Excitation and emission spectrum of eGFP
Excitation and emission peaks of enhance-GFP (e-GFP) are λ_{ex}: 488 nm and λ_{em}: 507 nm. The *Stoke Shifts* are very short. The overlap spectrum between excitation and emission is 475 nm and 525 nm.

Figure 2.8 illustrates the proposed fluorescence imaging device mechanism in achieving a high rejection performance emission filter and perceiving emission light from the GFP. The proposed imaging system combined composite filter, which is comprising a 550 nm short-pass interference filter and yellow and green absorption filters. A sandwich-like filter plays an essential role in preserving the device thickness and maintaining the complementary filter merits simultaneously. For the excitation light, I selected a blue laser that coupled on the optical fiber and irradiated light parallel to the image surface.

The coalescence of each filter spectrum is expected to produce a band-pass transmission spectrum close to the GFP emission, as seen in Figure 2.8 (b). The short-pass interference filter was selected to reflect all the light longer than 550 nm, which typically comes from red-fluorescence generated by the biological tissue. Blue shifting due to the high angle excitation light in a short-pass interference filter is more manageable in the way that it shifts the pass-band closer to the emission region. In contrast, the blue shifting of long-pass interference moves the band-edge of filter spectral response close to the excitation region. When the incoming light reaches the critical angle, the long-pass loses its reflection capability and passes the excitation light entirely.

The yellow and green filters are responsible for suppressing the excitation light and allowing the emission from GFP at the same time. Both filters transmit the light in their transmission spectrum and absorb unwanted light out of its spectral response. From these characteristics, the absorption filter act like the pass filter at a specific wavelength. As the second layer in the composite structure, the yellow filter absorbs the blue excitation light. Yet, under the intense excitation light condition, a radiative process frequently occurred, and some energy was emitted as fluorescent light out of the absorption band that so-called auto-fluorescence, lowering the GFP emission detection [30].

Consequently, a limitation exists while improving the excitation rejection level by increasing the absorption filter thickness. To address this limitation, I placed the green absorption filter structure beneath the yellow filter. Although the auto-fluorescence exists from the yellow filter, that emission is absorbed by the green filter and be prevented from reaching the image sensor. Moreover, the green filter ensures that the image sensor merely detects GFP green emission. Table 2.2 summarize the advantage and limitation of various emission filter compared to the proposed thin composite filter.

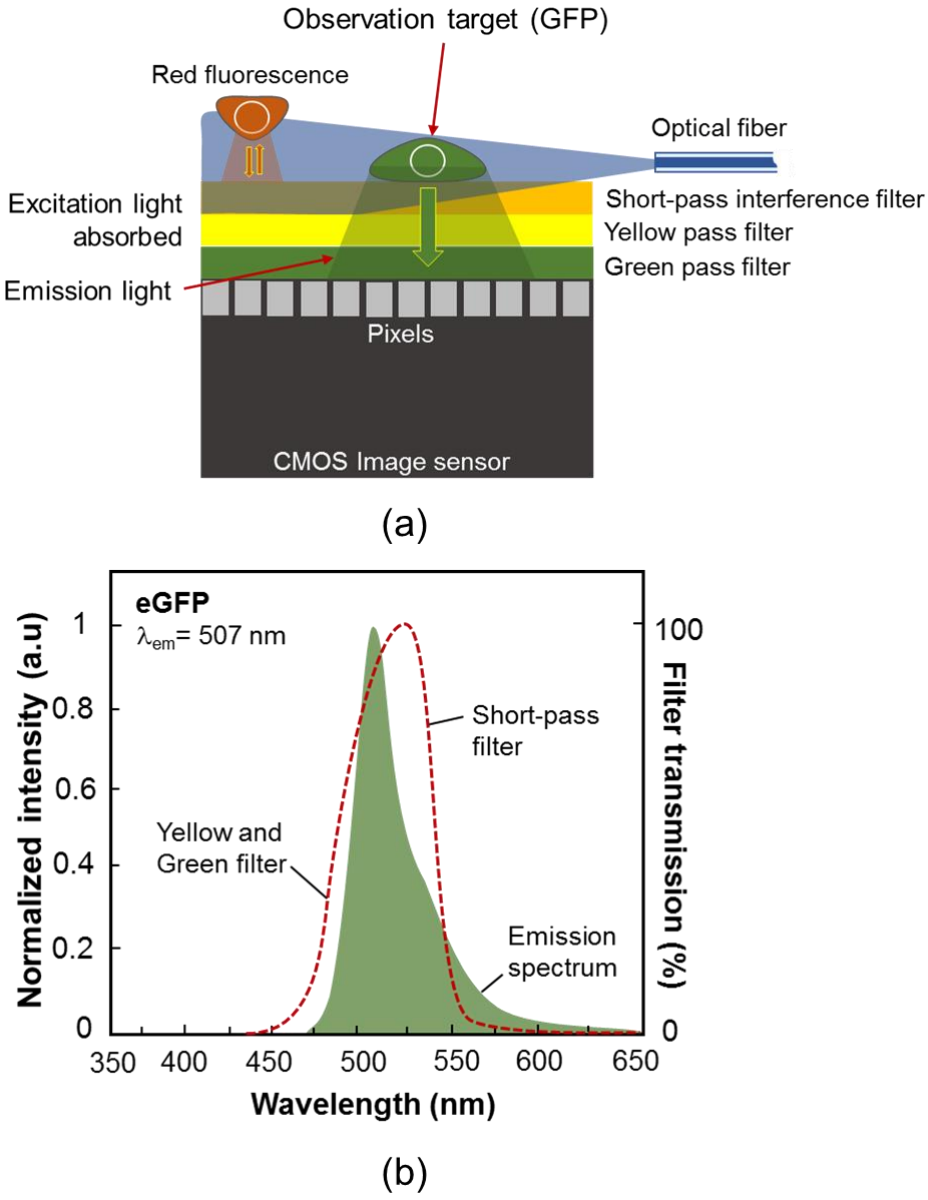

Figure 2.8 Schematic of the proposed fluorescence imaging device
(a) A schematic of the proposed device comprises a thin multilayer filter and parallel fiber-coupled laser excitation light. The uppermost layer is a short-pass interference filter and yellow and green absorption filter deposited beneath it, respectively. The observation target is GFP that placed directly on the filter surface. The GFP emission passes through the filter and reaches the image sensor. In contrast, the unwanted red-fluorescence from biological substances will be reflected by the short-pass filter (b). The expected transmission spectrum of the composite filter is the band-pass transmission spectrum (red dash line) that close to the GFP emission region (green area). This band-pass profile is resulting from the overlapping of each filter spectrum.

Table 2.2 The type of emission filter for an implantable CMOS imaging device

The type of emission filter	Filter structure	Advantages	Limitations
Interference filter [62], [63][69]	Interference filter (single layer)	● High rejection ratio (normal angle) ● Almost absent from auto-fluorescence ● Flexibility in spectral response design	● The rejection band is angle-dependent ● It comes with a bulky-glass substrate
Absorption filter [39][70][71], [72]	Absorption filter (single layer)	● Relatively inexpensive and easy to use ● Spectral response: independent of angle of incidence. ● Allows for very thin filter deposition	● Generates auto-fluorescence ● Inadequate slope and low peak transmittance ● High background noise image
On-chip hybrid filter [68]	Absorption filter (1st layer) Interference filter (2nd layer)	● Moderate rejection ratio (~ 43dB) ● Free from angle-dependence	● Requires stringent absorption filter: low auto-fluorescence ● Complicated fabrication process
Thick hybrid filter [67]	Interference filter (1st layer) Fiber optic plate (2nd layer) Absorption filter (3rd layer)	● High rejection ratio (~ 10^8: 1 at 450 nm) ● High contrast image, less background noise ● Wide field-of-view image	● Stacking filters is demanding ● Thick and not compatible for implantation
Thin composite filter (this work)	Interference filter (1st layer) Absorption filters (2nd layer)	● Thin filter for low invasiveness feature ● Preserves the complementary filter feature ● Flexibility in band-pass transmission design	● Challenging in depositing a thin filter ● The filter is a bit fragile

As mentioned before, the second pivotal point in obtaining a high rejection is using a narrow excitation light source, which has no green part inherently. To do so, I selected a blue laser (λ = 473 nm) instead of LEDs as an excitation light source. Compared to the GFP emission (λ_{ex} = 488 nm), the laser excitation wavelength is shorter than the GFP emission peaks. Exciting the GFP, not in its excitation peak, implies to the smaller number of photons absorbed by the GFP, and it thus produces a more moderate emission intensity. Nevertheless, since the blue laser offers a very narrow spectrum, which is almost no overlap with the GFP emission spectrum, thus blue laser can circumvent the undesirable detection of green light, which is inherently emitted from a blue light-emitting diode (LED).

Coupling the blue laser to a low-numerical-aperture (NA) optical fiber minimizes auto-fluorescence from the tissue through a finite-controllable illumination direction. A disperse excitation light is absorbed not only by the GFP but also by other pigmented substances in the brain tissue, which have maximum absorbance in the blue region as well [73]. Furthermore, assigning the optical fiber parallel to the image sensor decouples the illumination and detection of optical pathways (Figure 2.8 (a)); the excitation and emission light travel in a distinct path through the sample, which may improve the rejection and selectivity and avoiding overexposure detection.

2.5 Summary

Three critical components of the proposed fluorescent micro-imager for neuron cell observation in the deep brain are CMOS sensor, composite emission filter, and fiber-coupled blue laser excitation. For image detection, the CMOS image sensor relies on a wide-spectrum Si-photodiode of 3-Tr APS, which is integrated with buffer, row and column scanning, and amplifier circuit. I used two types of sensors: a needle-type (40 × 400 pixels) and a planar type

(120 × 268 pixels). Both sensors have identical fabrication processes, imaging mechanisms, and pixel scanning and data transfer. The needle-type is intended for reaching the deep-brain region with no excess tissue damage from the implantation process. Conversely, the planar type image sensor is for brain surface observation that provides a wide field-of-view.

Since the detection selectivity is a key in a fluorescence technique, an additional filter for isolating the emission light is mandatory. To date, two types of filters have been widely used as an emission filter in fluorescence imaging: an interference filter and an absorption filter. The interference filter reflects the light in the rejection band and producing no auto-fluorescence. But its spectral response is angle-dependence, which is becoming a significant drawback for contact imaging due to the proximity of object interest to the sensor. In contrast, the absorption filter spectral response is angle-independent, yet it generates auto-fluorescence under intense excitation light illumination. Complementing both filters in a hybrid filter structure compensates each filter's shortcomings. The proposed hybrid or composite filter comprises a 550-short pass interference filter and yellow and green absorption filters. These filters were selected to realize a band-pass spectrum close to GFP as the target detection. Combined with blue laser excitation coupled in the optical fiber, this imaging modality is expected to produce high rejection performance and fluorescent images.

3 Fabrication Methods

We live amid the plentiful of microstructure fabrication methods. Every technique has its unique pros and cons. Therefore, we need to understand the necessary features that should exist from products and the crucial factor to gain a high-yield fabrication rate. In particular, to fabricate a thin composite filter, which comprises an interference filter and absorption filters, the critical point is assembling the interference filter on the image sensor. By considering existing fabrication outside, this interference filter can be constructed using two approaches: deposit the filter on the image sensor or transfer the filter from other sources. Constructing the filter on the image sensor requires a high cost and sophisticated processing to compensate for the material mismatches. Therefore, the work presented in this thesis exploited the transferred method using laser lift-off (LLO) and plasma etching process.

On the other hand, handling the dye-based absorption filter is much simpler. We can deposit the filter solution on the pre-fabricated interference filter using a typical spin coating technique. This wet thin-film method relies on filter viscosity and rotation speed to control the absorption layer thickness. In this filter fabrication, the spin coating was used to construct the composite filter before enter the separation process using both LLO and plasma etching methods.

This section deals with an overview of the LLO and plasma etching, physics and concepts behind each technique, and their utilization for the composite filter fabrication. In the end is a summary and detailed discussion of the LLO and plasma etching process, how it can transfer a filter onto an arbitrary surface.

3.1 Laser Lift-Off Method

3.1.1 Overview

Laser, an acronym for light amplification by stimulated emission of radiation, is becoming a powerful tool in material processing. The loose coverage of material processing used here involves every action, procedure, or method to fabricate a particular structure of materials efficiently. Interestingly, the trend in material processing, especially in microelectronic manufacture, is getting denser, smaller, and thinner. Such trends open the possibility for the laser that has unique properties to take into account. Like electromagnetic radiation, laser interacts with materials in the form of absorption or transmission incorporated with energy and wavelength properties. When laser operates in non-contact mode, it furnishes a manageable material processing that is safe from an environmentally harmful substance like in wet chemistry processing [74].

When the microelectronic production requires thin layer separation, the lift-off (LLO) process is particularly suitable. The concept involves transferring the functional layers from its bulky-substrate to a new host substrate, which is lighter, thinner, and has a better thermal or electrical properties [75]. The LLO process enables high-selectivity separation through the selection of proper wavelength, optical system, and fluence of irradiation. Such a laser process has been used, particularly in semiconductor materials, for developing more efficient LED structure [76]–[81], laser diode with two-output wavelength [82] or assembled in a metal-substrate [83], and flexible electronic device [84]–[86].

In the next subsection, I introduce the LLO mechanism and essential points to be considered in semiconductor fabrication. After that, the logical and technical explanation of filter and CMOS sensor assembly using the LLO method.

3.1.2 Laser Lift-Off (LLO) Mechanism

The LLO process separates the functional layer by selective laser ablation. To successfully separates, the LLO process requires two essential ingredients: energy and selectivity. Energy from a laser beam is responsible for interface layer dissociation. While selectivity is related to the material hallmarks (e.g., bandgap and absorption coefficient) that determine in which area the decomposition occurred.

The well-known GaN separation is a prominent example of how laser energy and selectivity are taken into account in the LLO process for semiconductor materials. Figure 3.1 illustrates the schematic of the laser lift-off process for GaN layer separation and the transferred GaN layer after separation. A high-pulsed laser irradiates the interface area of sapphire and GaN and created heats to dissociate the GaN into its components. After laser irradiation, the GaN layer is then separated by applying external forces and transferred to the new substrate.

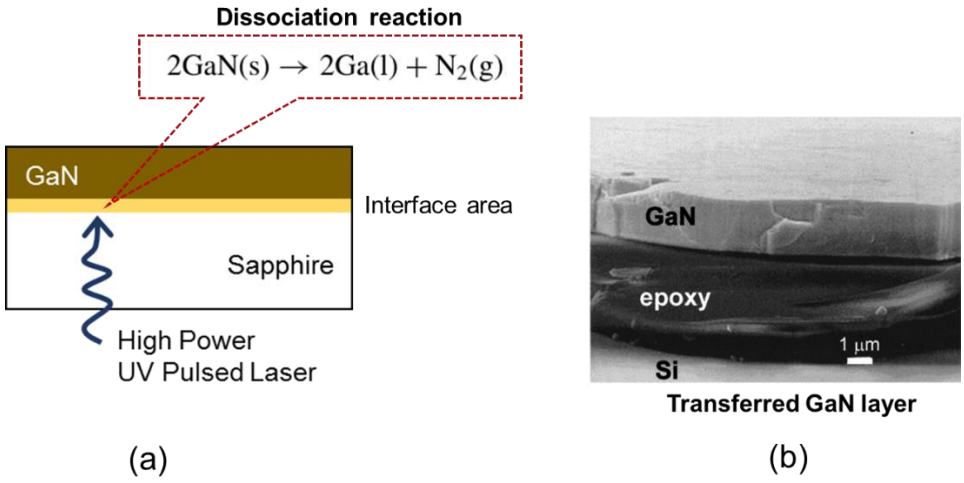

Figure 3.1 Laser lift-off for separating the GaN layer
(a) Schematic of the laser lift-off process in separating the GaN layer from its sapphire substrate. A high pulsed laser passed the sapphire and reached the interface area. Due to the selectivity, the GaN layer absorbed the laser energy. It generated heat to decompose the GaN into its components (b) A transferred GaN layer attached to silicon after laser lift-off.

Figure 3.2 describes the schematic of the vertical GaN-LEDs fabrication using the LLO process [87]. The commercially purchased GaN LED comes with a sapphire substrate. This LED structure is glued with a metal substrate on the opposite side of the sapphire using epoxy. Next, the high-intensity UV excimer laser exposed the LED from the sapphire side. As the sapphire is transparent, the laser energy is absorbed by GaN and converted into thermal energy alongside the interface area. After reaching a critical temperature, GaN is becoming thermodynamically unstable and starting to dissociate into its substance. Thus, by applying an external force to this structure, the functional GaN LED layer can be easily separated from the sapphire.

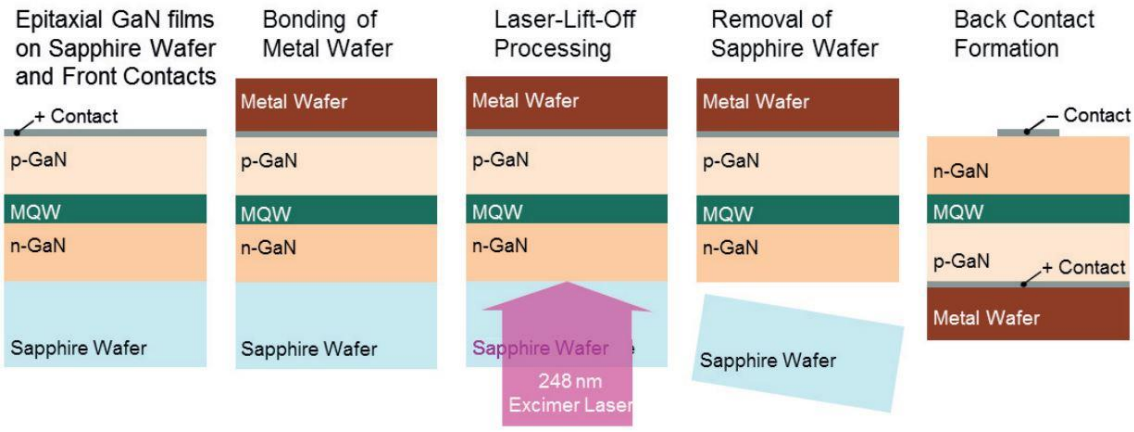

Figure 3.2 Fabrication of vertical GaN-LEDs via laser lift-off
An intended metal wafer is bonded on the opposite side of the sapphire substrate using specific glue. The excimer laser is then illuminated on the sapphire substrate, creates a decomposition in the interface area, and by applying a mechanical action, the sapphire can be separated. The final stage is to make a back contact for electrical function [87].

As mentioned earlier, examining how much laser energy is required to separate the GaN from its substrate is essential in LLO Process. Wong *et al*. reported that by using a single 600 mJ/cm^2 of 38 ns KrF (248 nm) excimer laser pulse, the commercially 3-µm GaN layer

decomposition critical temperature is between 900 − 1000°C [76], [77]. While Ueda *et al*. found that by using another type of laser source, i.e., third harmonic Nd:YAG laser, the 4-μm GaN started to decompose at 850°C by fluence at 260 mJ/cm^2. At that critical temperature, decomposition merely happened for GaN, not for the sapphire. This selective decomposition is due to the different energy bonds between sapphire and GaN. Saphire has energy bond higher than GaN; 17.35 eV/atom versus 8.92 eV/atom, respectively [88], [89]. Therefore, sapphire is more thermally stable than GaN. Maintaining laser fluence in the level providing the critical temperature is the key yielding spotless and large-free standing GaN layers. The increase of the fluence results in the blown-off of the GaN films is possibly caused by the increased vapor pressure of N_2 gas formed at the interface. In contrast, the reduction of the fluence results in insufficient delaminating [78].

Alongside with energy, selectivity is the trademark of laser lift-off processing. For GaN-sapphire materials, selectivity is enabled by the transparency of sapphire and the strong absorption of GaN to the laser. Both transparency and strong absorption are determined by the interaction of incoming light in the form of photonic energy, E_{hv}, and the bandgap energy of the material, E_G. The UV laser processing using KrF excimer laser radiation, E_{hv}, is 5 eV at 248 nm [77]. This photon energy is lower than sapphire bandgap E_S that is 9.9 eV [90]. Consequently, the photons weakly interact with the sapphire, allowing the photons to pass through the semiconductor material. The sapphire is becoming transparent to the laser irradiation.

In contrast, owing bandgap energy of 3.4–3.5 eV [91], GaN strongly absorbs the photons, causing the electron to move up from valance band E_V into the conduction band E_C. In a non-radiative transition mode, the electron then relaxes to the band edges and releases excess energy in the form of heat. As mentioned before, this heat decomposes ultra-thin GaN (~ 50 nm in

thickness) and decreases the interface bond. Figure 3.3 shows the band diagram of the laser, sapphire, and GaN [90].

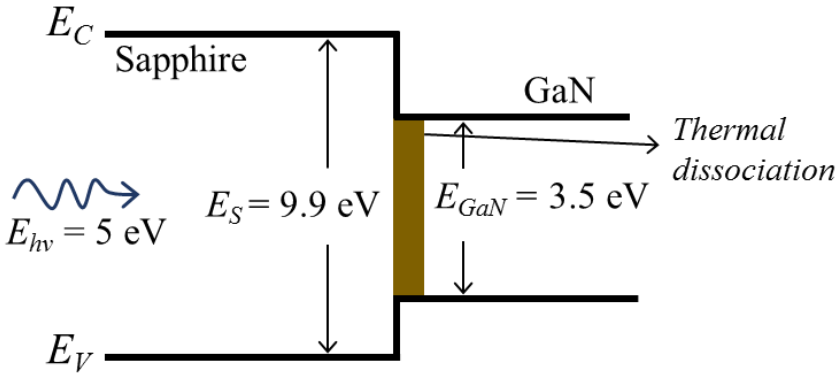

Figure 3.3 Band diagram of sapphire, laser photon, and GaN layer
As the sapphire bandgap energy, E_S, is higher than photonic energy, E_{hv}, sapphire has a weak interaction with the photon. While, as the band energy is lower than E_{hv}, GaN strongly absorbs the photon energy and release the excessive energy as thermal energy that decomposes the GaN layer [90].

3.1.3 Composite Filter Fabrication Using LLO

The crucial step in a composite filter fabrication is maintaining a thin layer of a free-standing interference filter that can be simply integrated with the CMOS sensor in a lens-free setup. A thin and free-standing interference filter benefits in accomplishing the low invasiveness feature of the implantable device. To do so, since the commercial interference filter, mostly available with a thick glass-substrate (~ 5mm), we need to do the filter separation in a very similar way to GaN LEDs by using the LLO process. After that, the exfoliated filter layer was transferred to the CMOS image sensor rather than metal as in GaN. Practically, the successful filter separation requires careful handling of laser energy ablation and irradiation time, which are indeed different from that of the GaN separation.

As explained in Section 2.4, I used a pre-fabricated 550-nm short-pass interference filter with ultraviolet (UV)-grade fused silica substrate (49-826, Edmund Optics, USA). The fused silica substrate was selected because it is transparent to the laser used for the LLO process (fourth harmonic of Nd:YAG laser at 266 nm). In contrast, the interference filter, which is mostly made of SiO_2 and TiO_2 or Ta_2O_5 for low and high refractive index materials, respectively, selectively absorbs the laser and generates heat on the interface area. This absorption selectivity can be explained by investigating the interference structure and bandgap energy of its filter constituent in comparison with the photon energy from the laser, similar to the GaN selectivity explained above.

Figure 3.4 (a) illustrates the multilayer filter structure of the interference filter composed of an alternate low and high refractive index material constructed on the fused silica glass. The lowermost dielectric layer directly contacted with the substrate is a high refractive material, e.g., TiO_2 or Ta_2O_5. Compared to the energy photon of fourth harmonic of Nd:YAG laser at 266 nm (E_{hv} = 4.66 – 4.7 eV) [92], [93], both high refractive materials have lower energy band 3.2 eV and 3.75 eV for TiO_2 or Ta_2O_5, respectively [94][95]. Therefore, the high refractive index material absorbs the excitation light from the laser and generates heat to separate the filter from the substrate. Conversely, the fused silica and SiO_2 have similar bandgap energy, E_{FS}, ranging between 7.52 – 9.6 eV [96], [97] that is indeed higher than the photon energy, E_{hv}. Thus, those materials have a weak interaction with the laser excitation. The band diagram of fused silica, photon form 4th harmonics Nd:YAG laser, and TiO_2 as a high refractive index material can be seen in Figure 3.4 (b). The transmission spectrum of the interference filter confirmed that 550-nm short pass interference does not pass the 4th harmonics Nd:YAG laser (Figure 3.4 (c)).

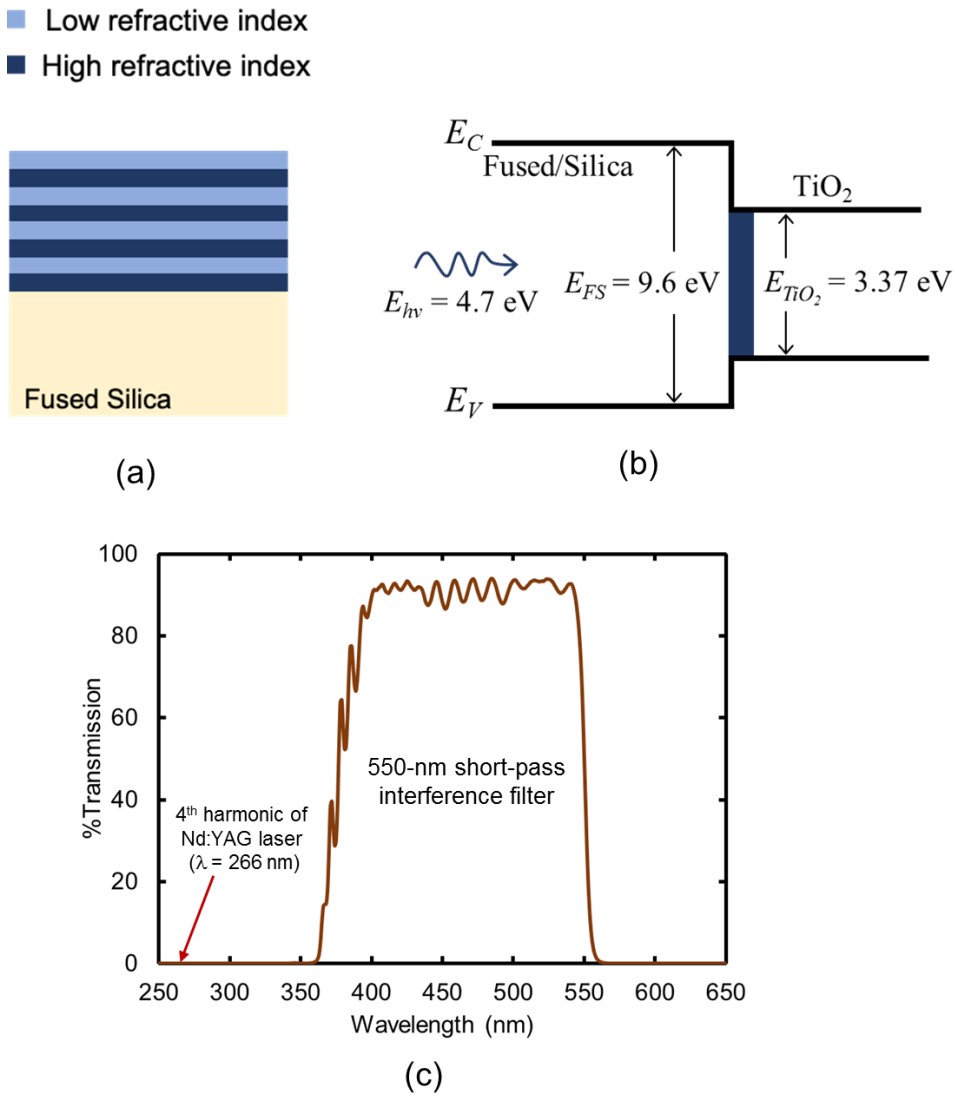

Figure 3.4 Interference filter selectivity from laser irradiation
(a) The interference filter comprises an alternate structure of high and low refractive index materials. The high refractive index materials are the lowermost layer directly contacted with the substrate (fused silica). (b) As the fused silica has higher band energy, E_{FS}, than photon energy from laser, E_{hv}, the substrate interacts weakly and become transparent to the laser. Conversely, the high refractive material, for instance, TiO_2, has a lower energy band, E_{TiO2}, than E_{hv}, so that TiO_2 absorbs the laser energy and excite the electron to the conductive band. The excess energy is real released as thermal energy to decompose the interface area. (c) The 550-nm short pass interference filter band-edge started from 350 nm and absorbed the Nd:YAG laser (λ = 266 nm).

Figure 3.5 illustrates the composite filter separation using the LLO process. The first stage is depositing the absorption filters into an interference filter to construct the sandwich-like

composite filter using a spin coating technique. Before the deposition process, the interference filter was cleaned with acetone, IPA, and de-ionized (DI) water sequentially and then dehydrated using a high-pressure N_2 gas blasting. Next, the yellow and green absorption filters were deposited on the interference filter using a spin coating technique, sequentially. The yellow absorption filter was made by mixing a Valifast Yellow 3150 (Orient Chemical, Japan), cyclopentanone (Wako, Japan), and NOA63 (Norland Product, USA) in a weight ratio of 1:2:1. This mixture was then spin-coated on the interference filter surface (1000 rpm, 15 s, produce thickness roughly 5 μm) and cured by UV irradiation for 30 s, and then heated at 150°C for 45 min to strengthen the filter hardness. Subsequently, a green absorption filter was directly spin-coated on the yellow filter layer (1000 rpm, 15 s) and cured by UV irradiation for 30 s and soft-baked (120 °C, 2 min), and then hard-baked at 200 °C for 20 min. Finally, the fabricated devices were cured at room temperature for 24 h to ensure the filter rigorousness before the attachment with the image sensor.

After the deposition process, a needle-type CMOS image sensor chip was fixed onto the filter layers using transparent epoxy resin (Z-1; Nissin resin, Japan) and cured by heat treatment at 120°C for 25 min. To get a highly uniform transferred layer, I placed the image sensor in the center of the spin-coated composite filter. The pixel area of the image sensor is directly contacted the uppermost filter. Following this assembly step, a high-precision laser with the fourth harmonic pulses, Q-switched Nd: YAG laser, λ = 266 nm (Callisto VL-C30, V Technology Co., Ltd.) cut the filter layer alongside the image sensor size. This cutting process is intended to isolate the filter area for laser irradiation; only the filter assembled with the sensor will be irradiated by the laser.

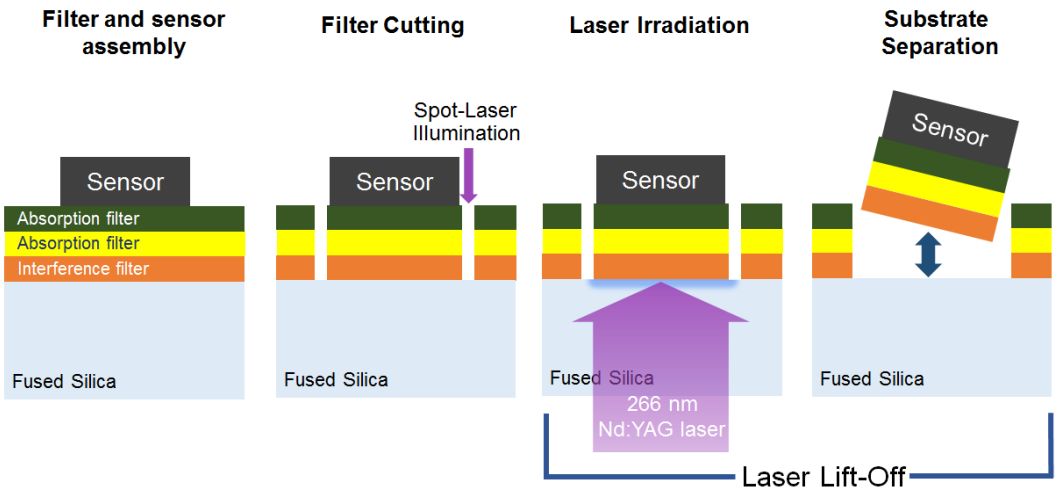

Figure 3.5 Integration of thin composite filter and image sensor by LLO process
A cleaned interference filter is the starting point. Next, the yellow and green absorption filters are deposited on the interference filter by the spin coating process sequentially and then attached with the CMOS sensor using epoxy. The composite filter is then cut alongside the sensor using ultra-thin laser illumination. The laser lift-off is started by illuminating the high power laser from the fused silica resulting in filter decomposition in the interface area. Finally, the assembled filter and sensor were gently separated by applying an external force.

Following the cutting filter step, the LLO process is started by applying a high-power pulsed laser from the backside of the fused silica substrate. I used the same yet a lower energy laser source (the fourth harmonic pulses, Q-switched Nd: YAG laser, λ = 266 nm) for the cutting process by changing the objective lens setup. High-power laser irradiation passed through a transparent fused-silica substrate and reach the interface area where the laser energy is selectively absorbed by the filter layer resulted in filter decomposition. To ensure that decomposition emerged over the filter area entirely, I used the laser lift-off processing that so-called step-and-repeat technique [87], where a continuous rectangular laser spot (~140 μm x 140 μm) is stitched in a stepwise irradiation process. After the laser irradiation, the filters were manually separated from the substrate by applying an external force.

The next step is integrating the free-standing CMOS sensor with a board function for electrical functionality and physical protection. As seen in Figure 3.6 (a), the integration process can be described as follows:

1. *Pads cleaning*: removing a filter covered CMOS sensor connection pads using, likewise, identical laser setting with the LLO process yet in discrete and localizing irradiation mode.
2. *PCB assembly*: a fabricated device was bonded on the designated printed circuit board (PCB) using epoxy resin (Z-1; Nissin resin, Japan) by heating at 120°C for 30 min for immobilization. This PCB is a simple electrical circuit for signal conditioning before wire transmission to the main circuitry.
3. *Electrical wiring*: the CMOS sensor connector pads were connected to the PCB via aluminum (Al) wires using a wire bonder (7700CP, West Bond Inc., Anaheim, CA, USA). Then, epoxy resin (Z-1; Nissin resin, Japan) was added and heated at 120°C for 25 min for wire protection.
4. *Parylene coating*: for waterproofing and biocompatibility features, the fabricated device was coated with a Parylene-C film using a Parylene coating chamber (PDS2010 Specialty Coating Systems, NIST, USA). The parylene thickness is maintained to be lower than three micrometers for retaining the small invasiveness feature.

Figure 3.6 (b) shows the fabricated device after the integration process. The total thickness is 166 μm: the CMOS sensor and composite filter thickness are 150 μm and 16 μm, respectively. This thickness level is acceptable to measure the fluorescence emission in the deep brain region as it is thin enough to limit damage to surrounding tissue as it is inserted in the brain [7].

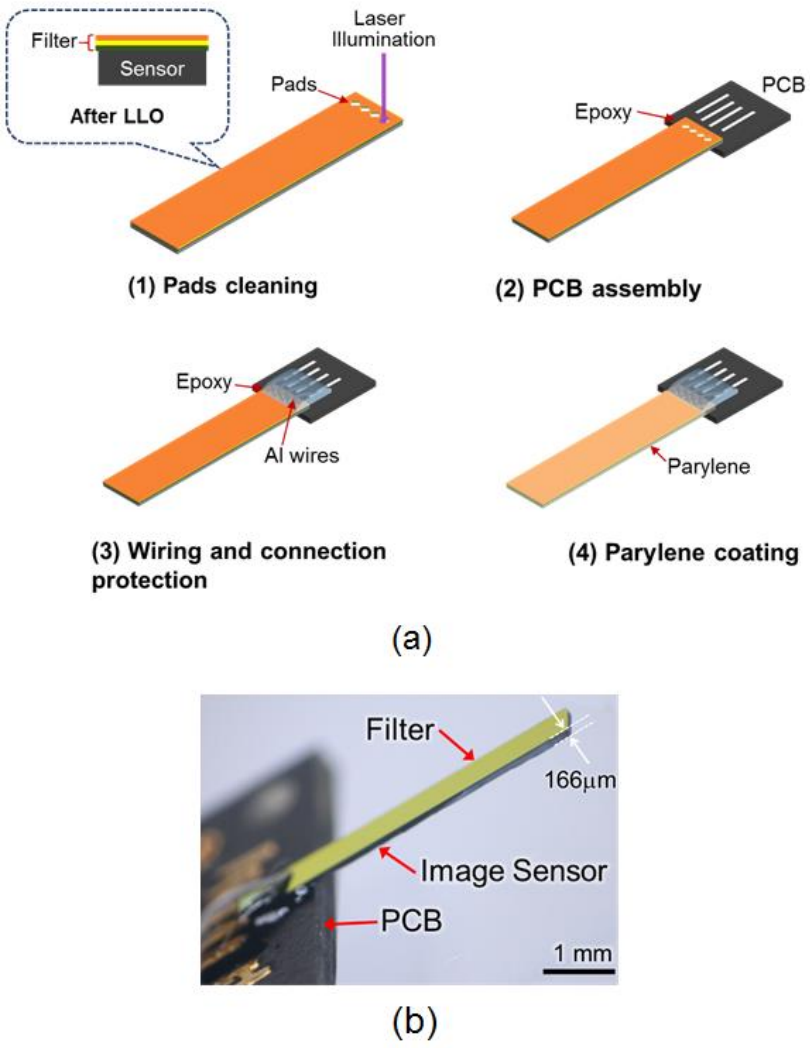

Figure 3.6 Integration of the image sensor and external components
(1) Removal of the filter on the sensor pads is done by localize-laser illumination, creating four unmasked pads. (2) Immobilize the image sensor to the PCB using epoxy. (3) Connect the sensor and the PCB using aluminum (Al) wire and protect the connection using epoxy. (4) Cover the filter surface with the Parylene for waterproofing and biocompatibility features. (b) Photograph of the fabricated device comprises an image sensor, composite filter, and PCB.

However, in a practical application, increasing device thickness due to the presence of optical fiber should be considered. For instance, it appends about 100 μm for a multimode optical fiber, which escalates the damage of the brain during the insertion process. One way to resolve this thickness issue is by utilizing an on-chip waveguide instead of a bulky-optical fiber

for delivering the excitation light. This light waveguide can be flexibly designed according to the light intensity required for the specific applications. Yet, the implementation of the on-chip waveguide on the fluorescence imager is beyond the scope of this thesis. The total weight of the fabricated device, including PCB, is about 0.05 g.

3.2 Plasma Etching Method

Plasma is the fourth state of matter, along with a solid, liquid, and gas. Plasma has very similar characteristics with gas (i.e., it does not hold any shape until confined) except that it has sufficient energy to free electrons from atoms or molecules and to allow both species, ion, and electron, to coexist. In short, plasma is an ionized gas.

In 1992, Bosch Corporate Research introduced the plasma etching technique for silicon through reactive ion etching (RIE) equipment for the first time. The plasma etching technique, which is then so-called "*Bosch Process*," combines gaseous etchant and ion bombardment for removal materials in the plasma environment [20]. The "*Bosch Process*" is nowadays the most widely used RIE silicon plasma etching technology and the key of today's key technology in micro-electro-mechanical systems (MEMS) product for automotive [21], [22], consumer electronics [21], [23], and IoT (internet of things) applications [24], [25].

In the next subsection, I briefly describe the mechanism of the "*Bosch Process*" in yielding high-aspect-ratio silicon microstructures and then bring its advancement into fabricating a large size and free-standing composite filter for the lens-free implantable imaging system.

3.2.1 Plasma Etching Mechanism

The "*Bosch Process*" relies on alternately cyclic etching and protection film deposition (passivation) by quick gas switching. Fluorine, typically from SF_6 gas, is the most widely used silicon etchant due to its higher etch rate than chlorine and bromine. On the other hand,

fluoropolymer, typically C_4F_8, acts as film protection of the sidewall so that the ion bombardment occurs in a vertical direction. The performance of the Bosch process can be affected by many parameters, such as the gas flow rate, etching chamber pressure, temperature, bias power, and the duration of the etching period and passivation period [98].

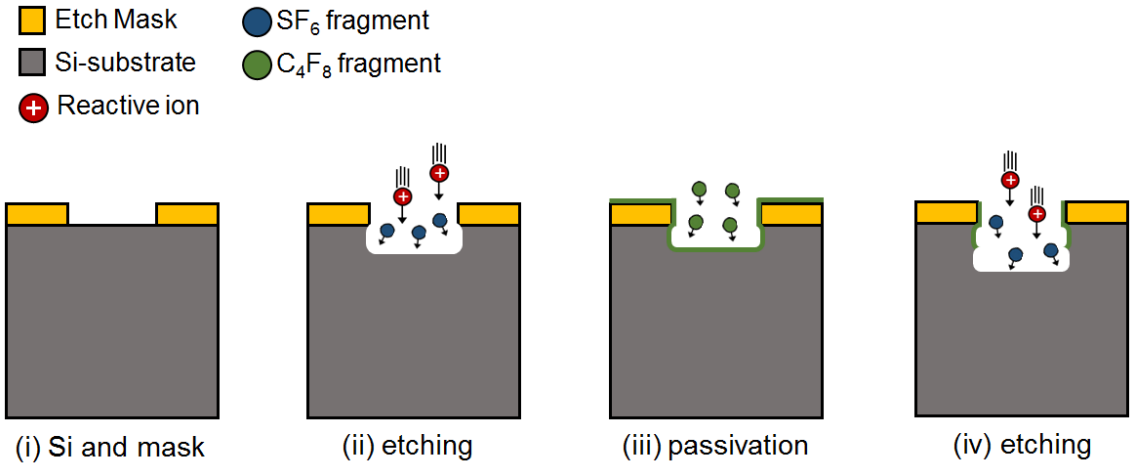

Figure 3.7 The Bosch Process for high aspect ratio Si-microstructure
(i) Mask navigates the etch direction merely in the unmasked area. (ii) Reactive-ions and fluorine are accelerated towards materials and forms the trench area. (iii) Fluoropolymer thin film covers all areas, particularly for sidewall protection. (iv) Reactive-ions eradicate the protection film at the lowermost area, and fluorine chemically reacts with Si to forms the further trench.

Figure 3.7 illustrates the "Bosch Process" of silicon microstructure. An etch mask is placed at the surface to navigates the etching direction. The SF_6 and C_4F_8 gases are pulsed alternately: with the help of reactive ions, an SF_6 fragment etched a few micrometers of silicon. Next, a C_4F_8 pulse is then applied. A fluoropolymer protective film is deposited all over the wafer, including the sidewall of the first trench. The next reactive ions remove the polymer film from

the trench bottom, but the sidewalls do not experience ion bombardment and remain protected (though are slightly etched by fluorine radicals). After removing the protective film from the trench bottom, SF_6 etching of silicon can continue making a deeper trench. The next C_4F_8 pulse deposits a new protective film, and then another SF_6 pulse is fed into the reactor. This alternate process occurs until it reaches a designated trench depth.

3.2.2 Composite Filter Fabrication Using Plasma Etching

The central idea behind the fabrication is composing the composite filter on Si-substrate instead of on a typical glass and then utilizing the etching minus passivation phase of the "Bosch Process" to eliminate Si selectively, leaving merely the assembled free-standing filter. We first designed the operational band of interference filter using dedicated optical software and then ordered the company to use a Silicon wafer as a substrate. The substrate differences, which is not a typical glass, does not affect the optical properties of the fabricated filter. To evaluate the effectiveness of plasma etching for emission filter fabrication, we used two types of interference filter: long-pass and band-pass interference filter. Evaluation is delimited only for physical and optical filter characterization.

Figure 3.8 shows the schematic of filter fabrication using plasma etching. Since the pre-fabricated filter was deposited on a 12.7 cm-diameter type-p silicon (100) wafer and 600 μm thickness, firstly, the wafer was manually diced using a diamond cutter into a 1 cm^2 size for handling easiness. The separated square filter is then cleaned using acetone, IPA, and DI water in an ultrasonic bath for 5 min each process sequentially. Afterward, the filter preparation for the etching process that can be described as follows:

a) *Filter deposition*: I used a single yellow absorption filter to reduce the filter thickness and thus improves the spatial resolution. A Valifast Yellow 3150 (Orient Chemical, Japan),

cyclopentanone (Wako, Japan), and mixed GA epoxy (Check at IFRC) were mixed in a weight ratio of 1:2:1. The mixed GA epoxy was made from catalyst GA-H-1 (catalyst) and epoxy GA-R-1 (type) in a weight ratio of 1:5 beforehand. The mixed filter dye was then spin-coated onto the interference filter at 3000 rpm, then cured by heat treatment at 120 °C for 20 min. Next, the composite filter was cured at tom temperature for 24 h to improve the structure solidity.

b) *Chip assembly*: the CMOS sensor was attached to the yellow filter using transparent epoxy resin (Z-1; Nissin resin, Japan) and cured by heat treatment at 120°C for 25 min. The pixel area of the CMOS sensor was directly contacted with the filter surface.

c) *Silicon etching*: the assembled filter was attached to a micro-cover glass using polyvinyl alcohol (PVA). This glass was then immobilized to another Kapton-tape-masked Silicon wafer using a high-vacuum silicon grease. The final assembly step before etching was placing the samples into an RIE machine holder (MUC-21 APS, Sumitomo Precision Products Co., Ltd., Japan). Additionally, PVA protects the CMOS sensor sides from being attacked by the SF_6 plasma during the etching process. In the RIE machine setup, the Si-substrate is on the uppermost part, which is directly exposed by the SF_6 plasma. By applying a continuous flow of SF_6 gas at 130 sccm and coil RF at 812 watts, a 100-μm Si-substrate thickness can be etched in 50 min altogether.

d) *Filter cutting*: the etched filter is then carefully handled for the laser cutting process by applying a high energy laser to remove the excess filter area.

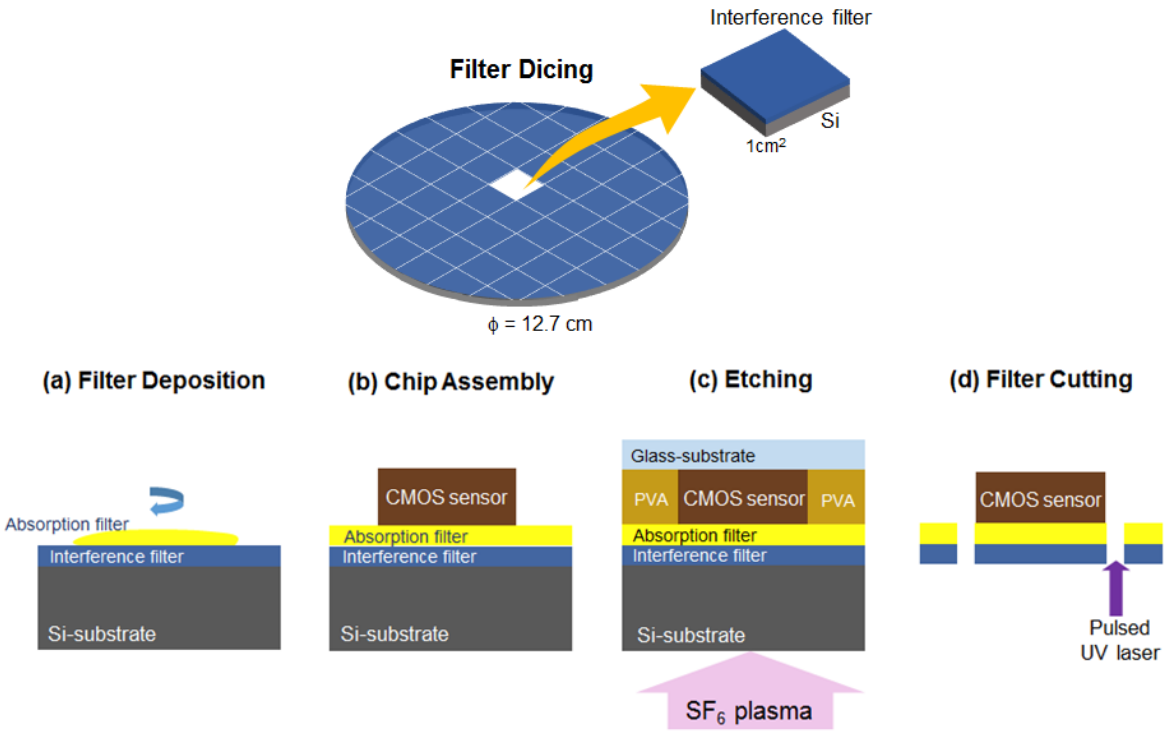

Figure 3.8 Composite filter fabrication using plasma etching
The interference filter was diced into a square shape for handling. (a) The yellow absorption filter was coated onto the interference filter surface. (b) Chip assembly using epoxy and heat treatment. (c) The assembled device was protected by PVA and attached to a glass substrate. The Si-side was then directly exposed to SF_6 plasma. (d) After etching, Si-substrate was utterly eradicated. Finally, the laser irradiation removed an excess filter.

In this work, as for the preliminary stage, I investigated the SF_6 plasma etching capability using an interference filter instead of a composite filter for the sake of sample preparation simplicity. However, this filter structure differences merely embroils the technical aspect of the assembly process. Indeed, it will not affect the filter quality after the etching process. Additionally, I delimited the evaluation only for etching capability in yielding a large-size and free-standing interference filter. Thus, there was no further assembly work with electrical wiring and parylene coating as in the LLO process.

3.3 Summary

In this chapter, two composite filter fabrications methods were discussed: LLO process and plasma etching. Both processes aim to separate the filter from its substrate, glass, and Si-wafer, respectively. LLO process relies on the thermal disassociation reaction that occurred on the interface area of target layers and substrate. Adapting the LLO process for GaN separation, two interdependence ingredients for a successful separation are laser energy and materials selectivity. The fluence of the laser beam should strong enough to heat the interface area and reach the critical temperature for disassociation, approximately 900−1000 °C for GaN structure [76], [77], yet not be too strong as it can deteriorate the layer. Filter separation using the LLO process requires laser fluence adjustment regarding its materials composition. The second composite filter fabrication utilized the etching phase of the so-called “Bosch Process” to remove Si, in which the filter was deposited beforehand, leaving the merely free-standing filter. Several essential fabrication steps were employed before the LLO and etching processes, e.g., multilayer filter coating, device assembly, and pre-treatment of filter separation. In particular, after the LLO process, the fabricated device was then connected to an external circuit and coated with parylene coating for the performance imaging evaluation.

4 Filter Evaluation

Successful composite filter fabrication for high-rejection lensless fluorescent imager can be identified at least in two domains: (1) succeeded in depositing the filter on the sensor flawlessly, (2) the fabricated device perceives the GFP emission selectively.

Before reporting the yield filter profile from both fabrication methods, LLO and plasma etching, I briefly discuss the transmission spectrum of an interference filter and absorption filters utilized for generating a band-pass spectrum profile of fabricated composite filter. Next, the examination of the fabricated filter after the LLO and etching process in terms of physical and optical properties examination, followed by an excitation light and spectral response profile followed by spatial resolution calculation from the microsphere emission. The last stage is examining the imaging performance by observing the GFP emission from gene-modified brain slice with laser and microscope excitation light. Filter evaluation for the plasma etching method is merely a physical observation, whether the filter is successfully deposited with no cracks.

4.1 LLO-Based Filter Fabrication

4.1.1 Physical and Optical Filter Profile

As mentioned in Section 2.4, the composite filter comprises a 550-nm short-pass interference and yellow and green absorption filter. Such a filter composition was selected to realize a high-rejection band-pass spectral response close to GFP emission as the target detection. Figure 4.1 shows each filter transmission spectrum and laser excitation I used in my fluorescent imaging system. Both absorption filters, yellow and green, are responsible for absorbing the blue excitation light and its scattered components from the tissue. In case the yellow filter generated the auto-fluorescence due to immense excitation light intensity, the

green filter absorbs such emission and ensures only green light from GFP emission can reach the image sensor. On the other hand, a very steep short-pass interference filter reflects all the light longer than 550-nm. From these filters and laser transmission profiles, the fluorescence imaging system is expected to detect the GFP emission accurately and absence from other unwanted incoming light.

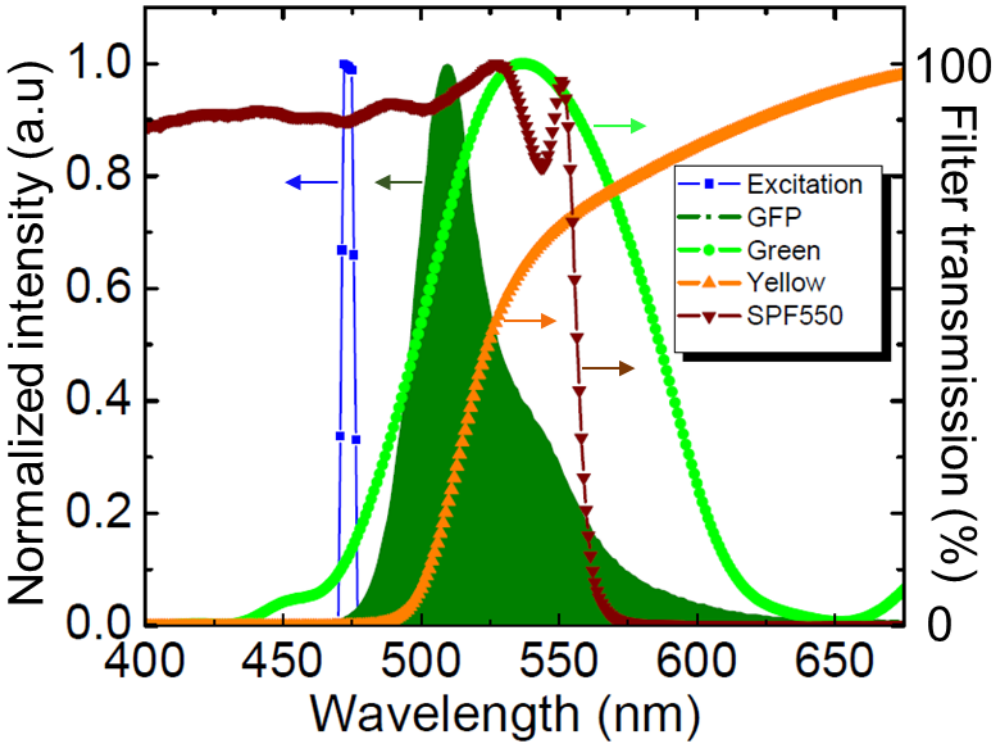

Figure 4.1 Transmission spectrum of filters and laser excitation light
Normalized intensity of blue laser excitation, a 550-nm short-pass interference filter, and yellow and absorption filter compared to the GFP emission. The blue laser has a very narrow spectrum and almost no overlap with the GFP emission region. The green and yellow filters are responsible for absorbing all the light that comes to the image sensor, and the short-pass filter is responsible for reflecting all light longer than 550 nm that is commonly generated from the red-fluorescence.

After the LLO process, the first evaluation is to confirm the effect of high energy laser ablation on the composite filter. The laser ablation's effect can be either in the form of physical

damages, e.g., crack or a coarse surface, or it deteriorates the multilayer filter structure and then changes the filter's rejection band. The surface of the exfoliated filter was visually examined to check the presence of laser ablation footprint and filter crack, followed by surface filter profiling to measure the laser ablation effects on the interference filter quantitatively. The optical examination was conducted by comparing the filter rejection band before and after the LLO process

Figure 4.2 (a) shows the photograph of a needle-type sensor assembled with a composite filter after the final assembly stage. Notably, the composite filter is successfully transferred from a fused-silica substrate to the needle-type sensor with no crack observed. Yet, the enlarged picture of the filter surface shows an inhomogeneous profile with a noticeable laser ablation footprint alongside the image sensor. Three different laser footprints emerged from stitch and stepwise of the laser illumination during the LLO process. As the rectangular laser spot size is about 140 μm x 140 μm, it is required four different paths to decompose the filter image sensor entirely. The difference filter surface for each laser path resulted from the unbalanced thermal distribution during laser ablation, which leads to inhomogeneous filter decomposition. This uneven heat distribution is possibly caused by the non-uniform filter thickness generated from the flawed spin coating process.

Additionally, overlap areas notably observed between two adjacent laser path illuminations. Delmdahl *et al.* (2012) have reported similar overlap patterns when using the stepwise laser illumination process. They stated that the depth of shallow trenches in the overlap area is below 100 nm [75]. To examine the surface profile quantitatively, I used a surface profiler (ET200, Kosaka Laboratory, Japan) over the selected area. As seen in Figure 4.2 (b), the inhomogeneous surface varies about ± 0.02 μm from its initial position, with some outlier peaks from the

impurities observed. The overlap laser path area and other visibly coarse surfaces indeed have more height variation.

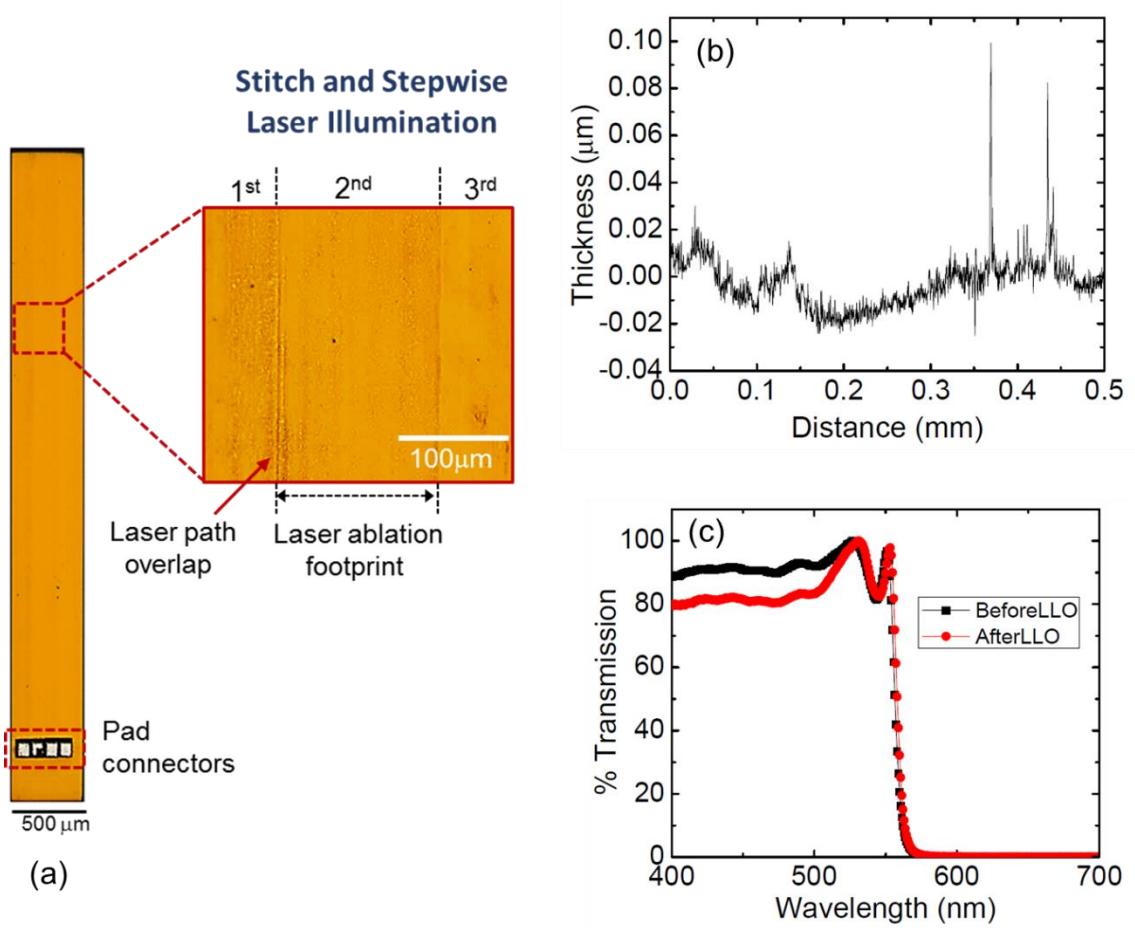

Figure 4.2 Needle-type sensor and composite filter integration after LLO
(a) Assembled composite filter on the needle-type sensor after the LLO process and the enlarged image was showing the inhomogeneous surface filter, where the laser ablation footprints emerged. These artifacts resulted from stepwise of three consecutive finite-laser illumination path. Overlap areas notably perceived between two laser illumination paths, (b) Surface filter shows an inhomogeneous profile generated from the laser ablation process, (c) transmission spectrum comparison before and after the LLO. The filter rejection band is unchanged.

To confirm whether the inhomogeneous filter surface affecting the filter rejection spectrum, I compared the transmission spectrum of the interference filter before and after the lift-off process. As can be seen in Figure 4.2 (c), both filters exhibited similar transmission patterns.

From these results, we can state that although LLO had generated a coarse surface filter, its rejection is unchanged and does not affect the final spectrum of the composite filter. However, the rough surface of the exfoliated filter scattered more light and lowered transmission of about 10% than that of un-exfoliated. These filter artifacts should be considered as one of the LLO fabrication drawbacks, which can affect the fabricated device performance.

Different results from the LLO process emerged for a planar-type sensor. The LLO process was incapable of separating the large filter of the planar-type image sensor flawlessly. Noticeable crack on the filter surface appeared during laser irradiation and after separation, as seen in Figure 4.3. Instantaneous cracks during laser irradiation are possibly caused by disproportionate heat distribution and thermal expansion differences of the delaminated and non-delaminated filter area (Figure 4.3 (a)). In particular, the crack mostly emerged in the edge filter area, where the heat generated by laser ablation could not propagate over the trench. Thus, as the energy is confined in a limited space, heat is getting accumulated until it reached the level that can deteriorate the filter. This unbalanced heat and thermal expansion disparities are not that high for the needle-type sensor because of its finite dimension in comparison with the planar type. Heat is proportionally distributed throughout delaminated and non-delaminated areas.

Analogous with GaN layer separation, the relieved compressive stress and vaporization pressure of N_2 from the decomposition mainly caused crack after laser irradiation. One solution to address this crack issue is by optimizing the fluence of laser irradiation. Moreover, from the layer thickness' standpoint, a thinner GaN layer is more natural to crack as it has more compressive stress released than a thicker GaN layer [78]. However, increasing the absorption filter thickness reduces the compressive stress and avoid the crack degrades the spatial resolution of the imaging device.

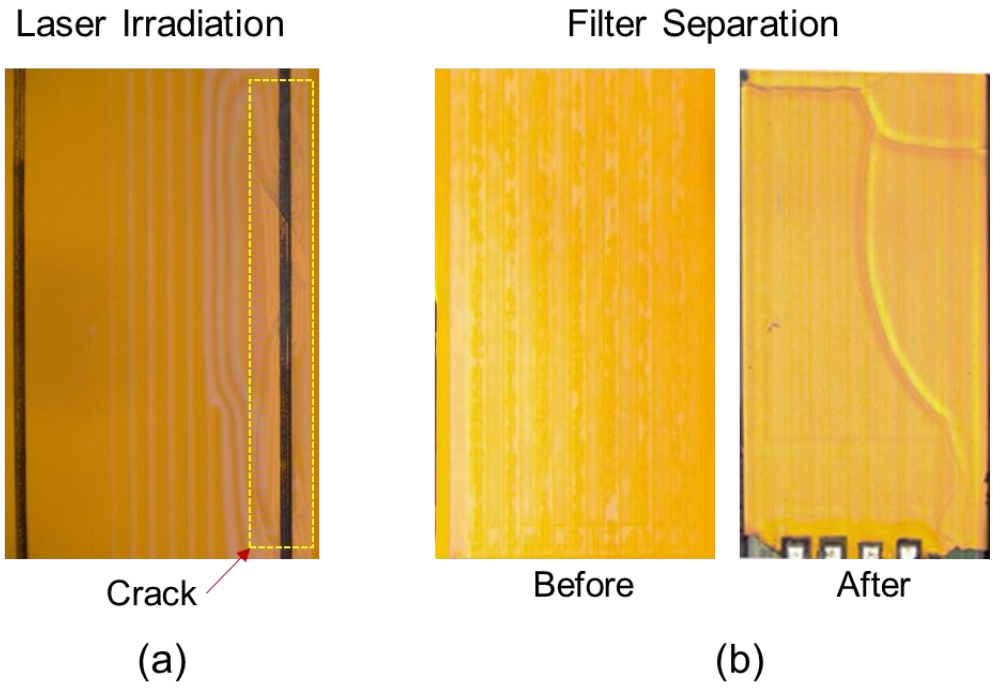

Figure 4.3 Filter crack on the planar type sensor
(a) An instantaneous crack emerged during laser irradiation due to the thermal expansion disparity. In particular, the crack mostly occurred in the filter edge area where the trench (black line) obstruct thermal distribution abroad. (b) Crack also emerged during the separation process. After the successful irradiation that kept the filter un-cracked, ensuring whether it was already separated from the substrate is challenging. A vivid crack emerged when an external force applied to separate the filter at the time where some area remains attached to the substrate due to the defective of the laser ablation process.

Although the filter was absent from instantaneous cracks during irradiation, the crack may occur during the separation process. Figure 4.3 (b) shows a free-crack filter before the separation stage. Practically, it was challenging to verify the filter status immediately after irradiation, whether it completely separated from the substrate. In many cases, some filter areas are remaining attached to the substrate because of the initial decomposition process. Thus, when the excessive force applied to separate the filter mechanically, the crack occurred along the

surface. It is, therefore, imperative that the LLO process is sufficiently robust for a limited-size, yet is failed for a large filter separation.

4.1.2 Laser Excitation Profile

In light of providing high quality excitation light for GFP emission, the narrow spectrum of blue laser (λ = 473) was selected and coupled to a multimode optical fiber (ϕ_{core} = 25 μm, NA = 0.1). To achieve an ultra-fine dimension, I removed the fiber coating part, leaving merely the cladding and core sections with a total diameter is 125 μm. As the laser transmitted to the fiber, the coupling loss, which means how much energy loss during the transmission from one to another fiber, is calculated by comparing the output power and input power in the logarithmic scale. It is found that the coupling loss in optical fiber transmission is 1.5 dB. This number is relatively high yet still acceptable for implantable fluorescence device applications.

After calculating the coupling loss, the next step evaluates the laser beam profile by observing its irradiation path in the fluorescent dye. The experiment setup is shown in Figure 4.4 (a) where the assembled optical fiber and an image sensor was immersed in 100 μM of green-yellow Uranine-filled glass cuvette from the vertical side. The tapered optical fiber was placed onto PCB on the topside of the cuvette. A blue laser illuminated the sample and generated an observable fluorescence emission, as can be seen in (Figure 4.4 (b)). The low-NA multimode optical fiber delivers a narrow beam alongside the image sensor area. As we used a typical laser beam with no optical treatment, the laser intensity did not uniformly propagate throughout the sample. It was observed that the intensity in the center of the light path is higher than in other areas. Figure 4.4 (c) shows the intensity profile in the region denoted with the yellow line, (b) fitted with Gaussian distribution. The full half-width maximum (FWHM) of laser intensity is 35.52 μm.

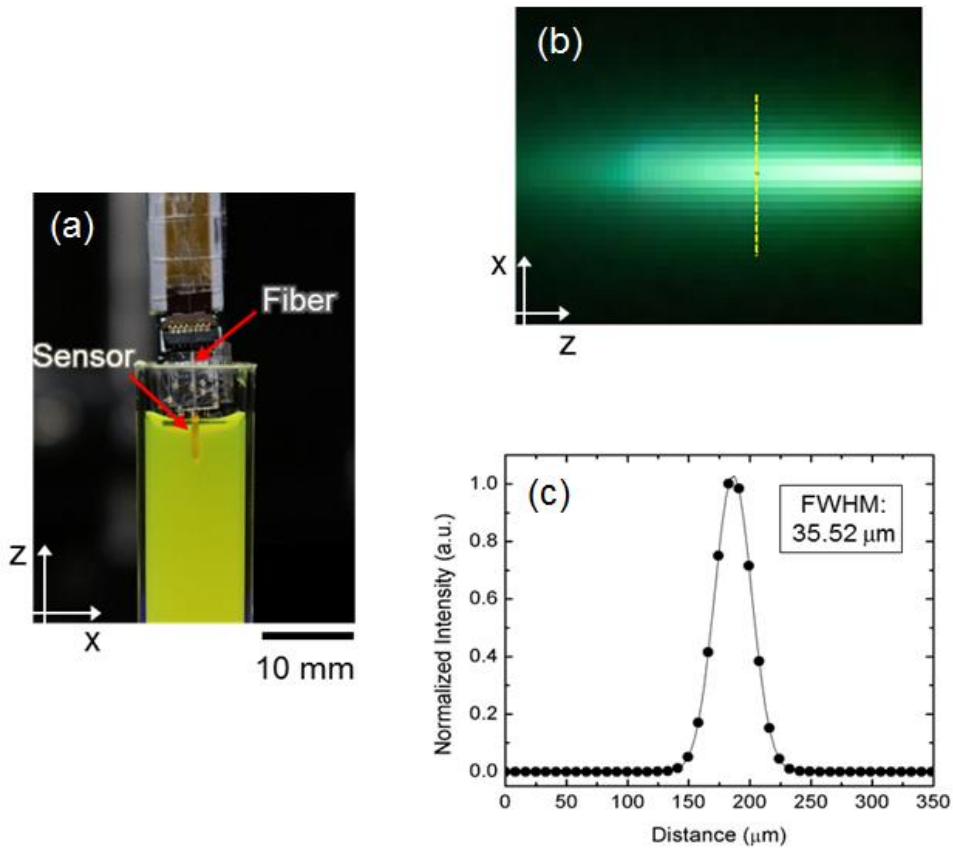

Figure 4.4 Laser excitation intensity profile
(a) Photograph of fiber-coupled laser assembled with the image sensor in the Uranine-filled glass cuvette. (b) Lateral views for the light-sheet thickness. (c) Light intensity profile alongside the yellow line at the light profile (b) that is fitted with the Gaussian distribution. The full-width-half-maximum (FWHM) is 35.52 μm.

The laser distribution is relatively small in comparison with the image sensor width so that the whole pixel area could not be covered in single laser irradiation. Thus, different excitation light directions are required to irradiate different places and then applied the image processing to concatenate images into a single final image. In addition, the disperse observation targets (i.e., GFP in the brain or microspheres) receive different light intensity depending on their

relative position to the laser path. The observation targets in the central light beam received the highest excitation light intensity than the other observation targets. This uneven excitation light distribution leads to a difference in fluorescence emission intensity over the area detection.

4.1.3 Pixel Sensitivity Characteristics

To thoroughly characterize the composite filter response to the incident light, I performed the pixel sensitivity measurement. The image sensor with the composite filter assembled on it measured the intensity of each pixel while being irradiated by a broad spectrum light source ranging from 400 to 675 nm (MicroHR Spectrometer, Horiba, Japan). To imitate the non-collimated incident light that reaches the sensor, I replaced an objective lens from the instruments by an optical aperture to localize the light beam on the sensor imaging area. I measured the pixel sensitivity at the normal incidence angle, which is the optimum angle for the interference filter to operate in its rejection band and the oblique incidence angle from 10 to 40 degrees. This angled incidence light measuring is to confirm the blue-shifting artifact of a composite filter that comes from its short-pass interference filter. Also, this angled light can be assumed as a scattered excitation light that traveled in a random path over the tissue in the real brain observation experiment.

As shown in Figure 4.5, the pixel sensitivity spectrum of the composite filter exhibited a band-pass transmission spectrum in the range 510–570 nm, which is relatively closed with GFP emission (λ_{em} = 507 nm). All lights out of the transmission band were significantly reduced. This band-pass transmission profile results from the complementary filter mechanism. The short-pass interference filter reflects a wavelength that is longer than 570 nm. Conversely, the yellow and green absorption filter absorbs light that is shorter than 510 nm. From this band-

pass transmission profile, the composite filter should suppress scattered excitation light and auto-fluorescence from the tissue, passing merely GFP emission to the sensor.

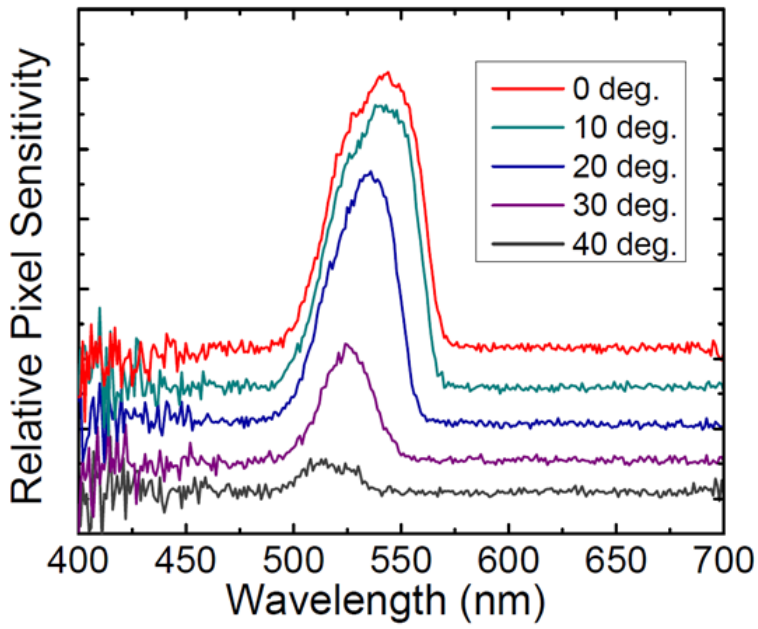

Figure 4.5 Pixel sensitivity spectrum of the composite filter
The composite filter exhibited a band-pass spectrum between 510 and 57 nm in the normal incidence angle (0 degrees). This spectrum is close to the GFP emission (λ_{em} = 507 nm). The right area of band-pass shifted to a shorter wavelength as the increased incidence angle while the left area is almost unchanged. This blue shifting emerged from the short-pass interference filter. The baselines are shifted to improve readability.

The band-pass spectrum shifted to a shorter wavelength by increasing the incident angle. This shifting emerged in the right spectrum, which is resulted from the short-pass interference rejection band. As predicted in Section 2.3, the blue shifting of the short-pass filter moved the pass-band of the composite filter to the shorter wavelength. In this case, force the band-pass spectrum moving closer to the GFP area. Indeed, this transmission spectrum shifting had increased rather than jeopardized the GFP emission detection selectivity.

In contrast, the left spectrum area, which is from the absorption filter, is relatively unchanged for all incident angles. However, since both filter characteristics operated simultaneously, the transmission band is then getting narrowed by an increase of the incident angle. The narrow window of pixel sensitivity implied to the lower sensitivity detection as the number of photons reached the sensor subsides.

The various incidence angle examination confirmed that the interference filter spectrum shifting had lowered the sensitivity yet not changed the window of selectivity. The composite filter transmitted the light in the GFP region in all angle variations. Also, since the proposed device placed the excitation light parallel to the image sensor, which can be treated as a very high incident angle, its excitation light intensity can be sufficiently suppressed.

4.1.4 Spatial Resolution

Spatial resolution is incorporated with the ability to resolve ultra-small objects in the field of view. For implantable fluorescence imagers, spatial resolution helps in determining how much the sensor can distinguish the observation targets (i.e., neuron cells with GFP in it). In this work, the spatial resolution is obtained by observing the emission from micrometer-sized fluorescence microspheres and then calculated the full width half maximum (FWHM) from single emission. This FWHM represents the shortest distance where two overlapping light intensity is resolvable, which means they will look like more than one peak.

I first observed the fluorescence emission from 15-μm diameter yellow-green fluorescent microspheres (F8844, ThermoFisher Scientific, Massachusetts, US). These microspheres emit the emission spectrum close to the GFP (λ_{em} = 515 nm) with an excitation spectrum in the yellow area (λ_{ex} = 505 nm). As mentioned in Section 4.13, this microsphere emission can be detected by the image sensor as its emission is in the filter transmission band. In addition,

compared to the CMOS sensor pixel size, the microsphere dimension is about double, which means these pixels, theoretically, can distinguish every single emission from the microspheres. The microspheres directly contacted to the image sensor to circumvent the spatial resolution degradation because of an additional distance.

Figure 4.6 (a) illustrates the schematic of fluorescence microspheres detection for spatial resolution measurement. The optical fiber was assigned at the edge of the image sensor, where no wire connection to get an utterly parallel laser illumination has. This highest angled excitation light does not affect the filter selectivity, as discussed in Section 4.13. After receiving the excitation light ($P = 100\ \mu W/cm^2$), the microsphere emitted the fluorescence emission that passed through the filter and then reached the pixels.

Figure 4.6 (b) shows various microsphere fluorescence emissions alongside the image sensor. The image denoted some microspheres were in the saturated emission while the others remained in acceptable emission levels (1). These emission differences resulted from a non-uniform laser excitation profile, as discussed in Section 4.1.2. The saturated emission emerged when the microsphere was placed at the center of the laser beam path and received the highest intensity. Contrariwise, unsaturated emission was from the microspheres out of the center of the light beam. The pixels sensor confirmed saturation by recording the maximum bit for all emission and exhibiting a non-Gaussian distribution profile. This saturated microsphere produces larger shapes than its real dimension because of the overwhelming emission, which leads to inaccuracy for the spatial resolution measurement. Therefore, merely unsaturated emissions are taken into account for spatial resolution calculation.

A region of interest (ROI), of around 125 μm × 125 μm dimensions, was selected from the single and unsaturated emission, as denoted with a dashed rectangle in Figure 4.6 b (1). The enlarged picture of ROI is shown in Figure 4.6 b (2). The yellow line alongside the x-pixels of

ROI was the area where the intensity profile extracted from the pixels. The data were then fitted with the Gaussian function, as shown in Figure 4.6 b (3). From this intensity profile, the spatial resolution of the imaging device was calculated in the form of FWHM as 22.3 μm ± 1.21 μm.

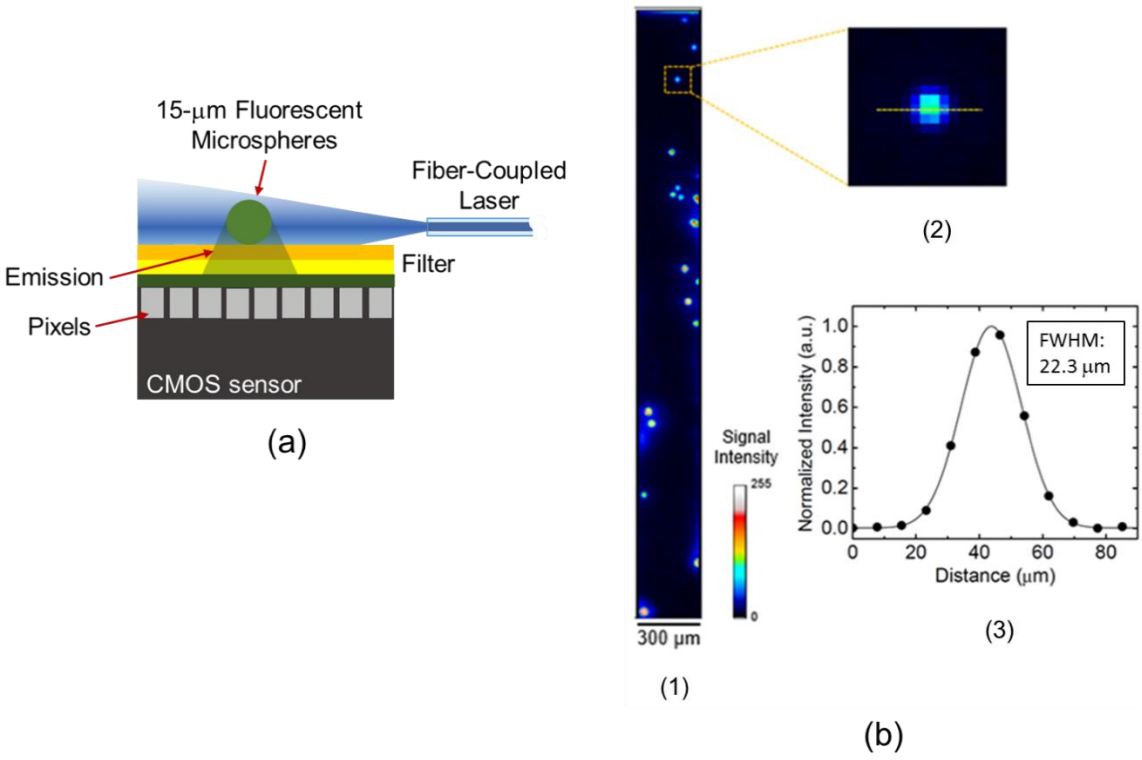

Figure 4.6 15-μm microsphere fluorescence emission with laser excitation light
(a) Schematic of spatial resolution examination by perceiving microsphere fluorescence emission. The microsphere is directly contacted. After excited by blue laser (λ = 473 nm) coupled on parallel optical fiber, the fluorescence emission passed through the filter and reached the pixels sensor. (b) Fluorescent images from yellow-green microspheres over sensor areas (1) and ROI was selected from unsaturated emission for spatial resolution examination (2). The intensity profile alongside the yellow line of (2) of the microsphere was fitted with the Gaussian function. The FWHM of a single emission is 22.3 μm.

The discrepancy profile of the microsphere emission from its actual dimension (ϕ = 15 μm) was due to the emission filter thickness. Although the composite filter is flimsy for such an implantable device, as mentioned in Section 3.1.3 is 16 μm. Still, compared to the microsphere, it is about the same dimension. The filter thickness increased the distance between the microspheres and the image sensor so that the emission light spreads over the filter and then degrades the resolution. Nevertheless, the spatial resolution of the fabricated devices is still acceptable for brain activity observation [99]. One way to improve the spatial resolution of the implantable device is by utilizing the incident-angle-selective pixel technique. In this technique, pixels, which normal and angle-selective, detect different incident angles via the designed metal aperture structure. As a result, the image reconstruction process can acquire a spatial resolution close to the pixel pitch [100]

Additionally, to evaluate the actual limit detection of the fabricated needle sensor, I performed the spatial resolution measurement using a sub-pixel microsphere, the yellow fluorescent particle (FP-3052-2, Spherotech, US), which has a diameter from 2.5 – 4.5 μm. The microsphere excitation spectrum is spanning from 400 to 495 nm and excitation peak (λ_{ex}) close to 480 nm, whereas the emission spectrum ranging from 478 to 560 nm and emission peak (λ_{em}) about 490 nm. Instead of using a non-uniform blue laser as an excitation light source, I used the uniform excitation light from the mercury lamp of a bench-top fluorescence microscope incorporated with an excitation filter to avoid the emission saturation. To imitate the laser excitation set up in the previous experiment, I assigned the image sensor to parallel with the incoming light, as seen in Figure 4.7 (a). The uniform excitation light illuminated the microsphere in relatively identical intensity over the image sensor surface.

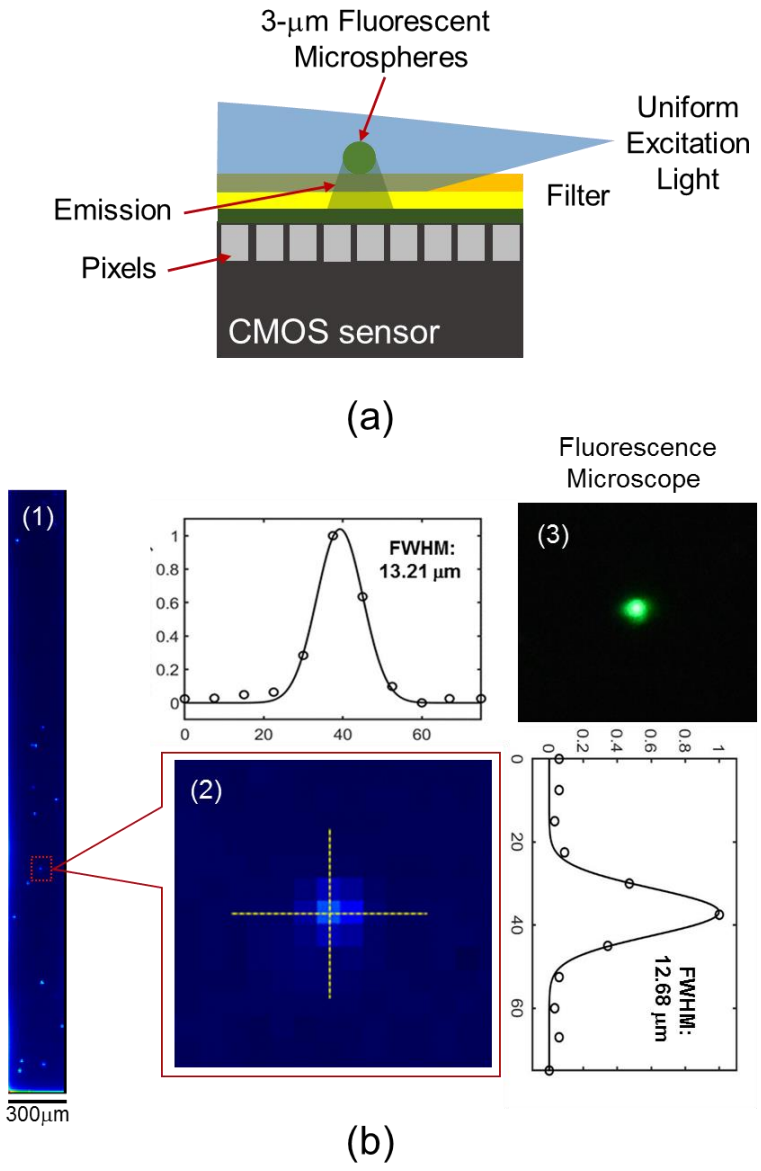

Figure 4.7 Sub-pixels microsphere fluorescence emission with a uniform excitation light

(a) Schematic of sub-pixel microspheres fluorescence emission detection incorporated with uniform excitation light. The needle-type sensor was assigned parallel to the incoming light so that all the sensor area is illuminated in a similar intensity. (b) (1) Fluorescent images captured by the needle-sensor from the microspheres over sensor areas, and (2) ROI was selected from the single emission for spatial resolution examination. The intensity profile alongside the yellow line of an image (2) was fitted with the Gaussian (vertical and horizontal). The average FWHM of a single emission is 12.94 μm. (3) A fluorescent image of single microsphere emission from a fluorescence microscope.

Figure 4.7 (b) shows the fluorescent images from microspheres over the imaging area. It showed that, notably, sub-pixel microsphere emission is much smaller than 15-μm microspheres. Also, employing the uniform excitation light resulted in a homogeneous emission profile perceived by the sensor; all the microsphere are in the unsaturated emission. Yet, the non-homogenous emission profile in the bottom image is generated by the light leakage from the improper black resistance shielding.

The ROI of a single microsphere from (image 1) was selected and enlarged with two yellow lines for evaluating the spatial resolution vertical and horizontal (image 2). The intensity along the yellow lines was then plotted and fitted to the Gaussian distribution. As mentioned at the beginning of this subsection, in microscopy, one standard method to describe the resolution is by calculating the FWHM of optically unresolved structure, which is in this experiment come from a single microsphere emission. However, calculating the spatial resolution from FWHM has a limitation that comes from the sensor pixels size, microspheres size, and filter thickness.

As can be seen in Figure 4.7 (b), the single microsphere emitted a Gaussian intensity profile both vertically and horizontally. The calculated FWHM in the horizontal line is 13.21 μm, and the vertical line is 12.68 μm. Thus the average FWHM, the spatial resolution of needle-type, is 12.94 μm. This number is about half of the spatial resolution from a 15-μm microsphere in the previous experiment. This number of spatial resolution is also close to that of the thick hybrid filter reported by Sasagawa *et al*. [67]. To be more specific and easy to understand, it can be stated that the needle-sensor with 7.5 μm pixels size integrated with a composite filter get the spatial resolution about 13 μm when observing the emission from 3 μm microsphere. The filter thickness, which is about 16 μm, degraded the spatial resolution and caused the discrepancy between the microspheres' size and spatial resolution.

4.1.5 Fluorescent Image from Brain Slice

4.1.5.1 Laser Excitation Utilization

Once the responsivity of the needle sensor to the fluorescence emission and spatial resolution were obtained, I performed an *in vitro* experiment to confirm the real performance detection in biological samples. To do so, I used 100-μm-thick brain slices obtained from an adult mouse (GAD67), which was genetically modified by GFP. All procedures for preparing the animal tissue were carried out following the guidelines of the Nara Institute of Science and Technology.

The brain slice was directly placed onto the surface of the image sensor, as seen in Figure 4.8 (a), while the optical fiber coupled blue laser ($P_{optical}$ = 100 μW/cm^2) in the parallel position to the brain slice. Similar to the microsphere experiment, the optical fiber was assigned at the edge of the image sensor, which has no wire connection to get an utterly parallel laser illumination. It was challenging to get parallel lighting with the optical fiber attached to the PCB because of the wire connection and epoxy (~100 μm height). Applying such an image sensor and optical fiber arrangement in the real implantable device platform, indeed, can be challenging if not impossible, as it can escalate the invasiveness. A promising strategy to address this limitation is by forming an on-chip waveguide on the sensor image that can deliver light in a specific direction yet remain to keep the low invasiveness feature. However, how-to fabricate the on-chip waveguide is out of this research's scope.

In the experiment installation, by separating the optical fiber from the image sensor benefits in obtaining clear images and a wide detection area. During the brain imaging experiment, both fiber and imager sensors can be controlled in vertical movement independently to get the optimum illumination direction and brain slice position relative to the image sensor. Also,

changing the fiber incidence angle allowed the excitation light to reach different areas in the brain slice, which benefit in resolving a finite laser beam issue.

Figure 4.8 (b) illustrates how the blue laser excites three different brain slice areas by changing the optical fiber incident angle, while the fluorescent images for each position are shown in Figure 4.8 (c), accordingly. The light travels from the bottom side of the images. In the first position (image 1), the optical fiber is almost parallel to the image sensor so that the laser beam irradiated the farthermost area of the brain slice. Then, increasing the angle beam by changing the optical fiber position relative to the image surface shifted the irradiation spot on the brain slice; it becomes closer to the light source (images 2 and 3, respectively).

This finite detection area resulted from the non-uniform laser beam profile that cannot reach the imaging area entirely. Thus, some areas did not get enough excitation light to generate an observable emission and turn out to be the opacity areas. Another parameter that may lead to this opacity is the gap that emerged between the brain slice and sensor due to the fiber insertion. In particular, this phenomenon is observed in the image (1) noticeably. Since the optical fiber is almost parallel, theoretically, the bottom area in the image is supposed to get the excitation light as it is the closest area to the fiber. Yet, practically, the gap between the brain slice and sensor suppressed the emission light from the brain slice.

The image processing technique was applied to address the excitation light coverage limitation by combining images from different irradiation spots into a single image. Then, a minor contrast adjustment was used to improve the image clearness. As a result, the image with a wide detection area occupied more than half of the image sensor area. In general, both unprocessed and processed images identify identical bright areas noticeably, and its pattern did not change with the incident angle excitation variation.

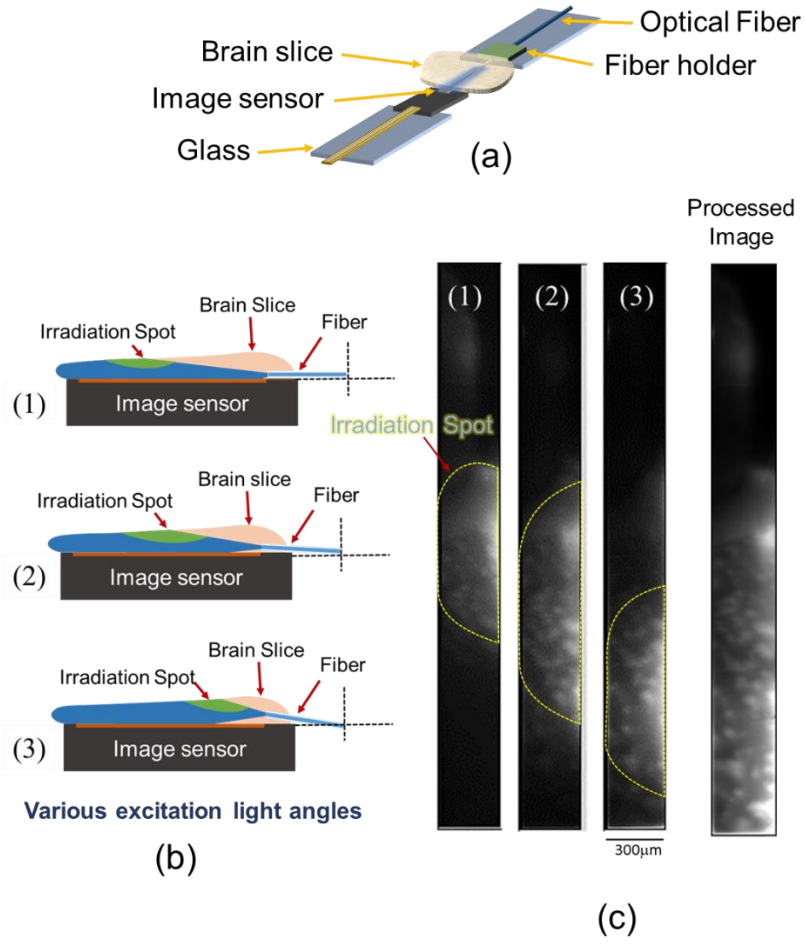

Figure 4.8 GFP emission from brain slice using laser excitation
(a) The experiment setup for fluorescence emission detection with various optical fiber positions, (b) Fluorescent images obtained by the image sensor. The light source travel from the bottom side. (c) Three different light source positions: (1) the furthermost irradiation area, (2) the middle irradiation area, (3) the closest irradiation area. (4) Processed image of different excitation light position for a larger detection area.

Figure 4.9 (a) shows the hippocampus area captured by lens-based fluorescence microscopy (BX51W1, Olympus, Japan). The target detection area was indicated with a yellow dashed rectangle. The detection comparison of the brain slice between the fabricated device and lens-based fluorescence microscopy can be seen in Figure 4.9 (b). In contrast, the fluorescent image obtained using the fabricated device (image 2) can observe a similar pattern with the lower resolution compared to fluorescence microscopy (image 1).

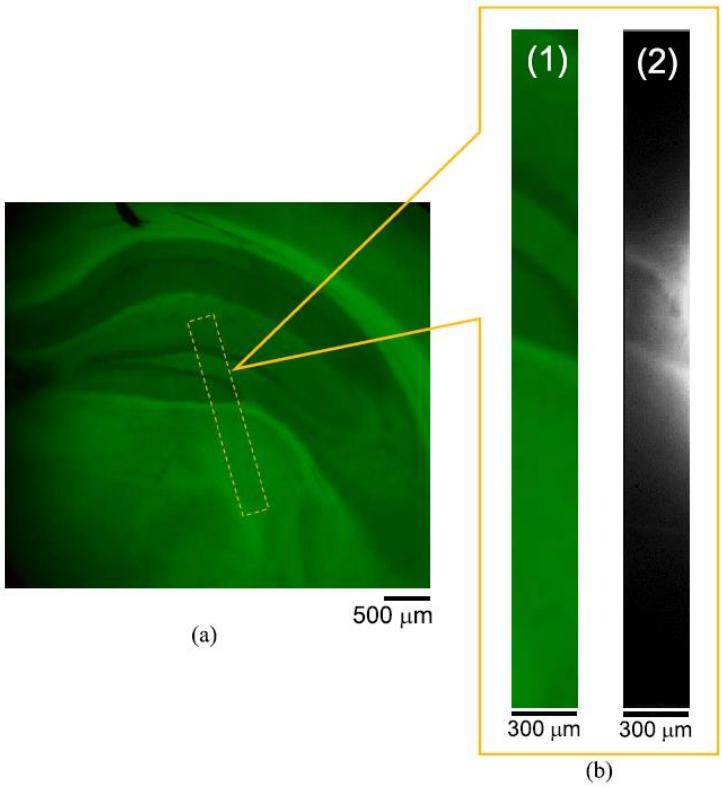

Figure 4.9 Fluorescent image of Hippocampus area
(a) The fluorescent image of the hippocampus area is captured by fluorescence microscopy. (b) The comparison image of a specific area in the hippocampus, denoted by the yellow dashed rectangle at the (a), produced by (1) lens-based fluorescence microscopy, (2) fabricated device.

Additionally, some saturated emission was observed close to the right edge of the device. This saturated pixel resulted from the high intensity of the excitation light and might originate from the leakage light caused by filter defects at the side of the images sensor. This shortcoming can be reduced by reducing the excitation light intensity and applying the black resist on the whole side of the image sensor. It is also important to note that the finite beam of a laser can only irradiate the limited brain area, which is similar to the previous in vitro experiment with three different observation areas.

4.1.5.2 A Uniform Excitation Light Utilization

Up to this point, the GFP detection described above was done by employing a non-uniform excitation light and produced intriguing results. Although the limited detection drawbacks seemly solved by applying post-image processing, investigating the sensor's response under the uniform and broad beam excitation light is inescapable subject to disclose. Illuminating the brain slice by such excitation light confirms the real composite filter performance detection with no interference from the inhomogeneous light beams, as when I used laser excitation. The expected result is a broad area detection, and the image sensor can distinguish GFP emission pattern from the cells, which has happened with the microspheres experiment in Section 4.1.4.

Figure 4.10 (a) shows the schematic of GFP emission detection by a needle sensor in uniform excitation circumstances. Comparable to the microsphere experiment, I employed the Mercury lamp from a bench-top fluorescence microscope incorporated with the blue excitation filter specified for the GFP experiment. The image sensor was placed parallel with the incoming light to provide high uniform light at the brain slice and avoid the sensor for being overexposed. In addition, the normal incident angle was selected to confirm the needle-sensor operation in a bright-field mode. The excitation light beam was controlled wide enough to cover all the imaging area in a single illumination. The brain slice directly contacted with image surface and can be easily moved to reach specific areas detection. The assembled imaging angle can be adjusted to get an optimum emission profile. The optical power of excitation light was selected at 329 μW.

I observed the GFP emission from a 100-μm-thick brain slice extracted from an adult mouse (GAD67). For more specific GFP emission detection, the image sensor was placed on the left side of the striatum region (CPu), as seen in Figure 4.10 (b). The yellow dotted square on the fluorescent image obtained by fluorescence microscopy (BX51W1, Olympus, Japan) indicated

the area where the needle sensor was assigned. The enlarged image of GFP emission from the fluorescence microscope is then compared by the GFP emission detected by the needle sensor.

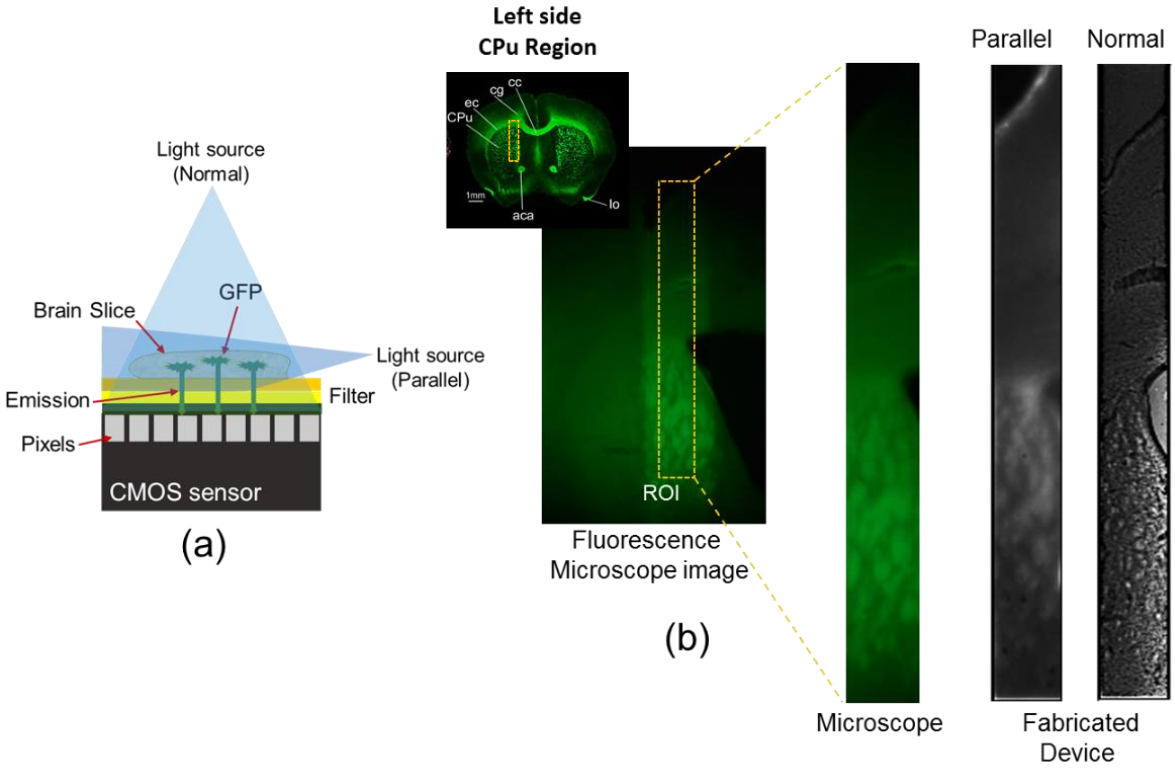

Figure 4.10 GFP emission with a uniform excitation light
(a) The brain slice was assigned on the image sensor surface and excited by the uniform excitation in parallel. (b) Image comparison of the CPu region between the fluorescence microscope and the needle-sensor. The enlarged area of the fluorescence microscope's image from the yellow dotted line (left) is then compared with the fluorescent image from the needle-sensor. The fabricated images with parallel illumination showed an identical GFP emission pattern with the microscope's image. The normal incident light showed that the needle-sensor acts like bright-field microscopy that generated images with no GFP emission.

Notably, under the uniform excitation light, the needle sensor achieved a wide-area detection and resembled the emission pattern exhibited by the lens-based microscope.

Moreover, this needle sensor presented a better contrast fluorescent image under parallel excitation light, compared to the fluorescence microscope's image, specifically, on the upper edge of the brain slice. Under an intense excitation light, which is coming from a normal incident angle, the needle-sensor behaved like a bright-field microscope that perceived the brain-slice image without GFP emission.

4.2 Etching-Based Filter Fabrication

4.2.1 Effect of Si-Substrate Surface in Filter Quality

Plasma etching capability to fabricate a large and high uniformity filter was evaluated by examining the filter surface visually. As mentioned in Section 3.2.3, in the preliminary stage, plasma etching was applied to remove Si-wafer in the single interference filter. I tested two silicon dummy-chip in the different assembly set up, as seen in Figure 4.11 (a): fully contacted (image 1) and partially contacted (image 2) with filter. The partially contacted filter that has a free area in the lowermost image is to investigate the possibility of depositing filters only in the specific area, e.g., the imaging area. This free area can be used for the sensor pads connector. To protect the dummy chip from being etched by the SF_6 gas, all chip areas, including the free area, was covered by PVA. After the etching process, the PVA was dissolved using water, and the free-standing filters were obtained and ready for the next assembly stage.

Figure 4.11 (b) shows a large and spotless interference filter after the etching process; no crack emerged for both fully and partially contacted setup. SF_6 plasma successfully etched Si-wafer and leave the large and high-uniformity interference filter attached to the dummy chips. Also, the partially contacted filter installation (image 2) shows that the filter is assigned only in the designated area (pixel area), whereas in the free area, no filter is attached.

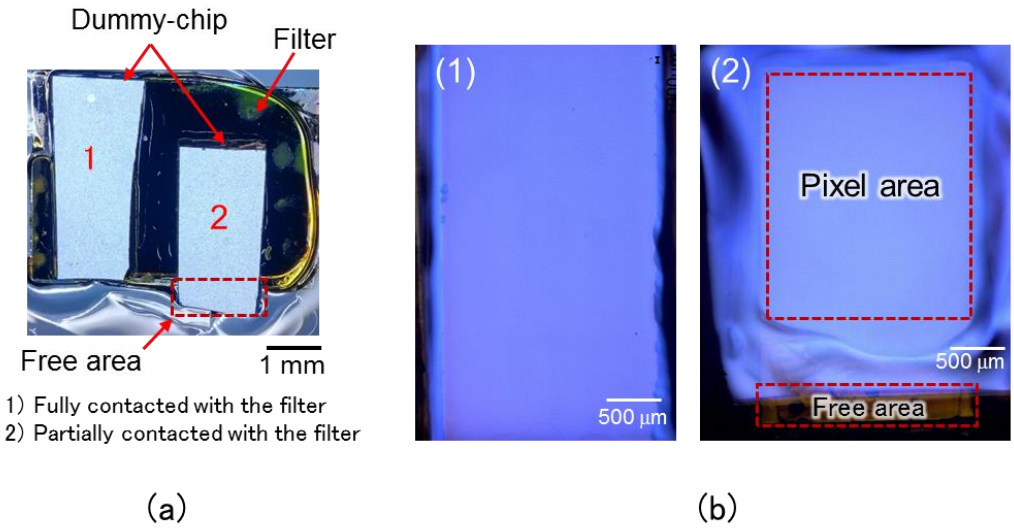

Figure 4.11 Large filter from the plasma etching process
(a) Photograph of the assembled filter and Si-based dummy sensors for the plasma etching process. The dummy chips were directly contacted with the interference filter, and the Si-substrate was in the filter's backside (b) Photograph of the sensors after plasma etching: (1) fully contacted (2) partially contacted with the filter. Both filters showed a large and spotless surface profile. The partially contacted filter provided area that absent from the filter.

It should be noted that there are two types of Silicon wafer surface available in the market nowadays: (a) a mirror-like surface and (b) a coarse surface. The interference filter I used for the preliminary stage has a mirror-like surface. To decipher the plasma etching behavior for various Si-wafer surfaces and its filter quality after the etching process, I performed the etching process using a coarse Si-wafer, where a band-pass spectrum deposited on it. This band-pass spectrum operates close to the GFP region.

Figure 4.12 shows a band-pass interference filter after the etching process that similar to the previous interference filter. Two different particle impurities were observed: small and big particles, as illustrated in Figure 4.12 (a). These small particles emerged in the interface between the filter and sensor that may come from the improper chip and filter assembly stage. On the other hand, big particles appeared in the filter surface as a Si-Substrate.

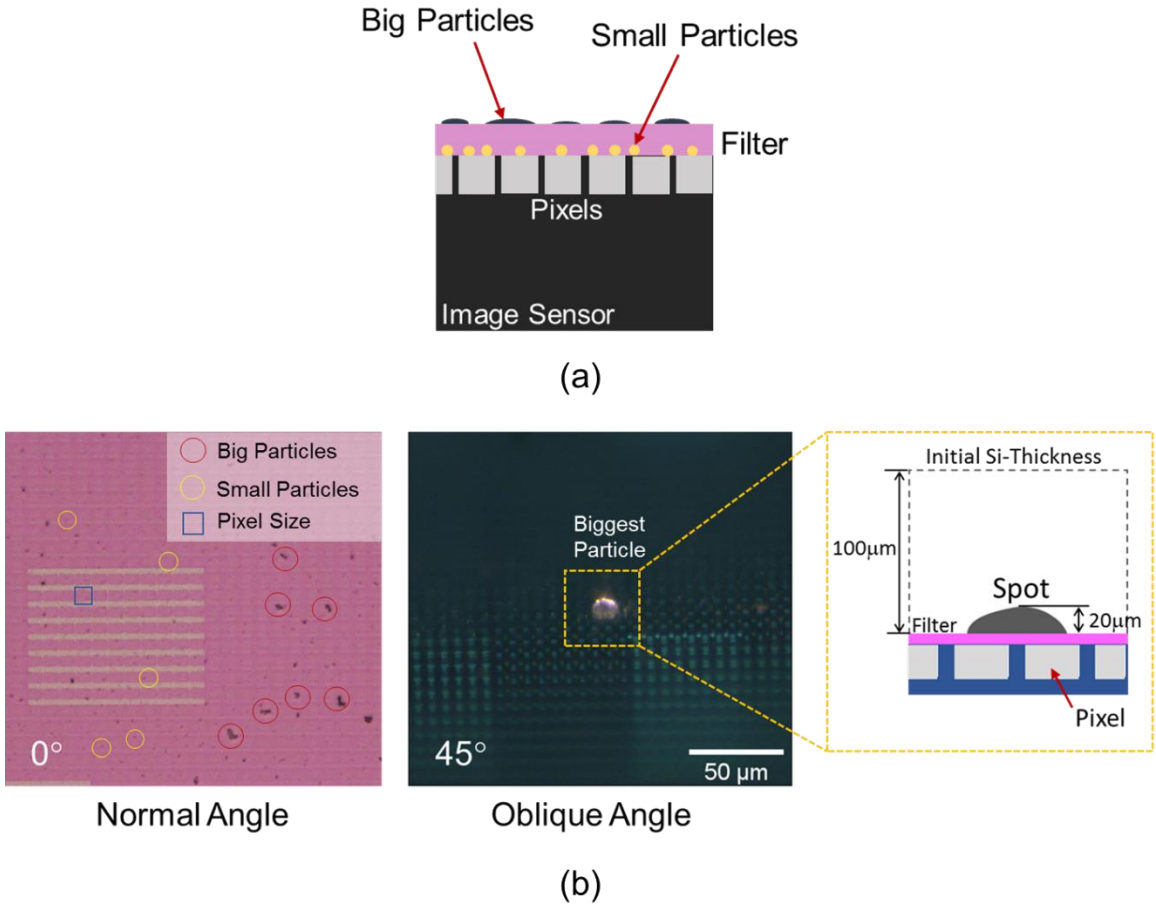

Figure 4.12 Filter profile of coarse Si-wafer surface after plasma etching
(a) Illustration of the small and big particles on the filter after the etching process. (b) Micro-photograph of the filter after the etching process. In a normal angle observation, both small and big particles were observed clearly. Yet, in an oblique angle observation, only big particles were observed. One of the most significant particles has a thickness of about 20 µm. The big particles on the filter surface might come from the imperfect etching process.

The different positions between small and big impurities can be confirmed by observing the filter in the normal incidence angle and oblique angle, as can be seen in Figure 4.12 (b). In the normal angle observation, both particles were observed clearly, and their difference dimension can be distinguished easily. Yet the oblique angle observation showed only the big particles on the filter surface. An in-depth examination of the biggest particle reveals that it has a thickness

of 20 μm, which is about a fifth of the initial Si-wafer width. Practically, for all coarse surface of Si-wafer, these big spot impurities remained exists even by increasing the time etching. One reckoning factor that can explain this phenomenon is that the spot is not a pure Si; it is the kind of Si-compound resulted from imperfect pre-treatment. Since the SF_6 gas chemically reacts only with Si specifically, this compound cannot be removed even in a very long duration of etching time.

To confirm the possibility of Si-compound in the wafer surface, I applied the pre-cleaning using a reactive ion etcher (RIE-10NIT, SAMCO, Japan) to remove all the oxide and dielectric material from the Si-surface. The etcher machine utilized CHF_3 and O_2 with the flow setting 20 sccm/5 sccm, respectively, for a 5-minute cleaning process. After cleaning, the filter is then directly assembled with the required components for the plasma etching process.

Figure 4.13 shows the band-pass filter surface with a pre-cleaning treatment after the etching process. Notably, the normal angle observations showed small particle impurities with no big particle on the filter surface observed. The oblique angle of observation (45°) confirmed the absence of any substances in the filter surface, which means the small particles inserted between the filter and CMOS sensor. From its size, all small particle sizes are relatively in the micrometer range, but they are still big enough to block the pixels from receiving the light. Practically, since the Si-wafer is opaque, it was difficult to confirm the particle's presence in the interface area between the filter and CMOS sensor directly after the assembly process. More effort in the pre-treatment stage is needed to address this particle's impurities problem. However, both filters displayed the possibility to fabricate the large and uniform filters using the plasma etching method.

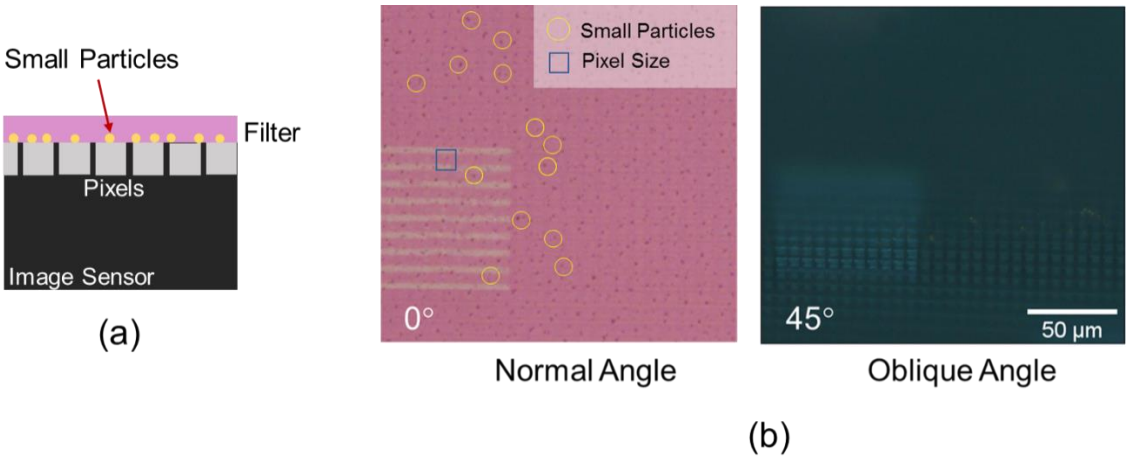

Figure 4.13 Filter profile of coarse Si-wafer surface after dry-cleaning and plasma etching process
(a) Illustration of the small particle impurities inserted on the interface area between the filter and CMOS sensor. (b) These small particles can be observed clearly in a normal angle observation, yet unobservable for oblique angled. Compared to the pixel size, these small particles are relatively big enough to block the incoming light to the pixel.

Following the physical examination, the transmission spectrum of the etched filter was then measured using a spectrophotometer and compared with the GFP emission. The band-pass filter was attached to a micro-cover glass using epoxy and then etched with the identical parameter with the previous etching process. Figure 4.14 shows the band-pass filter transmission spectrum after the etching process and GFP emission: (a) merely band-pass filter, (b) composite filter (band-pass filter and yellow filter) in various incidents of angles of excitation light. Notably, the band-pass filter spectral response is ranging from 500 nm to 560 nm, which is very close to the GFP emission region. For the band-pass filter, like another interference filter, the transmission spectrum was shifting to the shorter wavelength region as the increase of the incident light. At the highest incident angle (45°), most of the transmission spectrum was in the blue region and out of the GFP emission region.

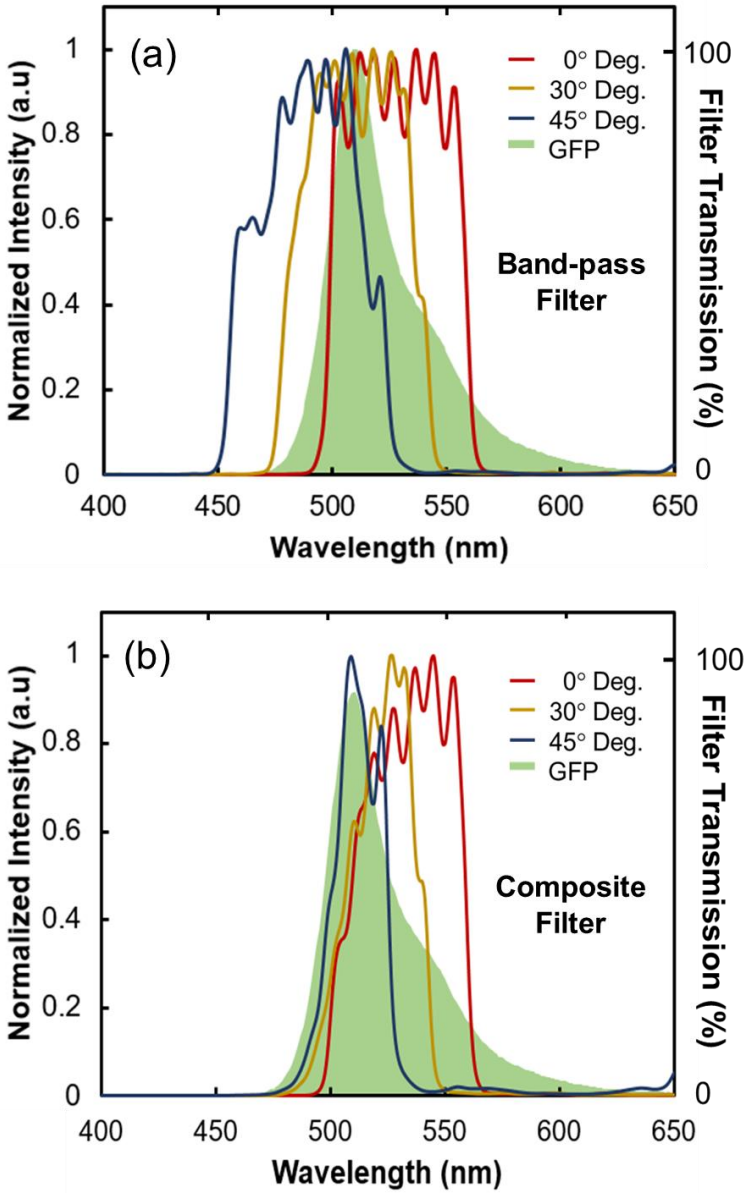

Figure 4.14 Transmission spectrum comparison between the band-pass filter and composite filter

(a) The band-pass transmission spectrum operated closely with the GFP emission in a normal incident angle (0°). The transmission spectrum is then shifting to the short wavelength as the increasing of the incident angle. When the incident angle is 45°most of the transmission spectrum is out of the GFP region. (b) The presence of a yellow filter has changed the transmission spectrum: the short-wavelength region became shallower in corresponding with the yellow filer spectral response. The blue shifting in the composite filter merely occurred at the band-pass spectrum's right side, which is come from the interference filter. The ripples in the transmission band resulted from the optical admittance mismatched between filter and glass substrate.

In contrast with the band-pass filter, the blue shifting of the composite filter merely occurred on the right side of the transmission spectrum, while the left-side of the spectrum is almost unchanged. This different transmission profile is because the left side of the composite filter transmission spectrum is from the yellow absorption filter, which its spectral response is independent of the incident angle. The increasing incident angle has narrower the transmission spectrum of the composite filter. From this transmission spectrum, it can be stated that the composite filter can maintain its transmission band to operate close to the GFP emission in all angles of the incident light.

Another critical point that needs to be considered in the real applications is the ripples at the transmission spectrum. These ripples are observed to swing for about 20% of the transmission. These ripples are probably generated from the optical admittance mismatches between the filter and glass sample and the epoxy. This transmission spectrum profile can degrade the detection performance of the fabricated device.

4.2.2 Large-Emission Filter for Multi-Chip Fabrication

Despite the impurities from the assembly stage, the large and high uniformity filter yielded from the etching process has corroborated the idea of tailoring the plasma etching for multi-chip fluorescent device fabrication. The interference filter was prepared to accommodate a large multi-chip wafer-die with a dimension of 4.5 cm and 2.5 cm in height and width, respectively. This CMOS die has 11 different sensor sizes, as seen in Figure 4.15 (a). The multi-chip die and interference filter were etched using the standard etching process. After the plasma etching process, all Si-substrate was extinct, and the large interference filter deposited on the multi-chip sensor (image b) and ready to enter the next assembly process. Yet, one additional step is required to separate each image sensor using the dicing process.

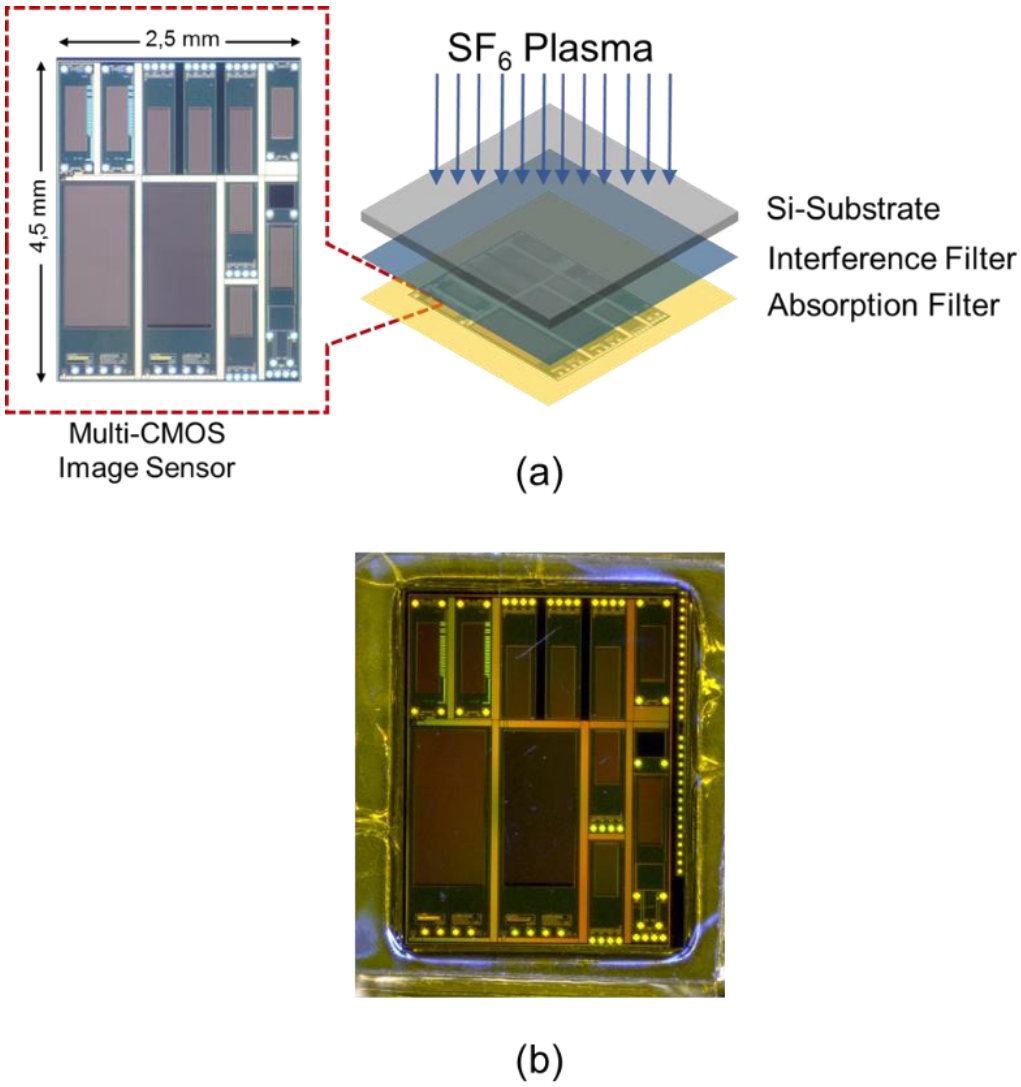

Figure 4.15 Multi-chip and filter integration using plasma etching
(a) Schematic of multi-chip and filter attachment. The multi-chip was attached to the filter using epoxy. In the etching process, the Si-substrate is exposed to the SF_6 plasma. (b) Large and spotless interference filter deposited on a multi-chip wafer after the etching process.

4.3 Discussion and Summary

This section has presented the fabrication and evaluation of a thin composite filter for implantable device application using laser lift-off (LLO) and plasma etching. The LLO process

successfully constructed a filter on a needle-type sensor. Despite the laser ablation footprint observed on the filter surface after LLO, its transmission spectrum is unchanged. To successfully separate the filter flawlessly, maintaining the number of laser energy irradiated and the speed of the stitching process are essential. If the irradiation is too short, because of the rapid laser-probe movement, the high-energy laser does not have enough time to generate heats that can deteriorate the interface bond. In contrast, it required more prolonged exposure to separate the filter using a low energy laser.

The composite filter produced a band-pass spectrum close to the GFP region and achieved the spatial resolution 12, 95 μm. By having this number of spatial resolution, the needle sensor can identify the GFP emission from neuron cells in a brain slice noticeably. By employing a uniform excitation light, the needle sensor perceived an identical pattern with a lens-based fluorescence microscope.

In contrast, the LLO process was incapable of separating the large filter of the planar-type image sensor flawlessly. Noticeable crack on the filter surface emerged during laser irradiation and after separation. An instantaneous crack during laser irradiation is possibly caused by uneven heat distribution and thermal expansion of the delaminated and non-delaminated filter area. For the needle-type sensor with 300 μm in width, it requires about three times repetitive laser irradiation to cover all areas. The heat from laser irradiation will be proportionally distributed over filter areas.

On the other hand, it is difficult to confirm the filter separation condition directly after irradiation, whether it completely separated from the substrate. Sometimes, some filters are remains attached to the substrate because of insufficient energy for decomposition. Thus, when the excessive force applied to separate the filter mechanically, the crack occurred along the surface. Therefore, the LLO process is sufficiently robust to transfer composite filter onto a tiny

image sensor. Yet, this method is exhausted in separating a large and spotless composite filter. Consequently, LLO is not suitable for a multiple image sensor fabrication that traditionally reaches the centimeter range size.

The second fabrication method by utilizing plasma showed promising results: large and high-uniformity filters that cannot be achieved by LLO due to the thermal expansion mismatches. This fabrication merit opens up the way for multi-chip fabrication in a single process that can escalate the lens-free device applications in the future.

5 Conclusion

At this point, I hope the reader has gained the necessary information for fabricating a thin composite filter, specifically, using laser lift-off (LLO) and plasma etching method. Also, the expected filter characteristic and the imaging results from the evaluation section. In this Section, I resume the work done and followed by a short outlook.

5.1 Summary

This thesis has presented a thin composite filter fabrication using LLO and plasma etching for the implantable fluorescence image sensor. As the background of my research, I explored the basic knowledge of behavioral experiments and their available imaging modalities, followed by the basic concept of the CMOS image sensor. To enhance the detection selectivity of the CMOS image sensor, applying an optical filter is necessary.

Practically, the work in obtaining a high-rejection ratio in lensless fluorescence imaging system is started by designing the emission filter to work closely with the GFP as my observation target. In general, two types of emission filters are used for lensless imaging systems: an interference filter and an absorption filter. Both filters have their advantages and disadvantages when it operates in a single-mode that leads to a low rejection-ratio and contrast image. The reason implemented the composite structure—comprises an interference filter and absorption filters in a multilayer structure—rather than a single filter emission filter, is also explored. Also, by utilizing a narrow spectrum laser excitation light rather than a broad spectrum of LED, the fluorescent images of the implantable device can be significantly improved.

Adapting from the semiconductor manufacturing method, LLO was utilized to separate the composite filter from its substrate and transferred to the image sensor. Through nursing the laser ablation energy, the LLO process successfully constructed a filter on a needle-type sensor. The next assembly process integrated the sensor with the required components for imaging functions. However, the LLO failed to separate the large filter because of the thermal expansion issue during laser irradiation and the rudimentary decomposition that generated vivid crack after separation.

Fabricated device evaluation includes physical and optical properties of exfoliated filter, laser excitation profile, spatial measurement, and GFP emission detection from microspheres and brain slice. The spatial resolution of fabricated devices about 13 μm, which is high enough to detect some large-type individual neuron cells in the brain. The in vitro experiment shows that GFP emission from brain slice can be detected noticeably. Moreover, by employing a uniform excitation light source, the sensor resembled emission pattern with the lens-based microscope, which is the gold standard for fluorescence imaging.

Plasma etching is commonly used for high-aspect-ratio Si-based microstructure fabrication that yielded large and homogeneous filters with relatively high reproducibility. These merits can thus be extensively utilized for multi-device fabrication that may pave the way for the massive development of fluorescent micro-imager.

5.2 Outlook

There are many possibilities to continue the work presented in this thesis, especially since I successfully showed the needle sensor capability in perceived GFP emission, which is comparable with the pattern generated by a lens-based microscope. I delimited the improvement in two areas: improves the filter fabrication more effectively and integrates the uniform yet

narrow-spectrum excitation light source with the image sensor in a compact yet lightweight platform.

The preliminary stage shows promising results from the plasma etching method; large and uniform filters can be obtained after the etching process. Yet, some sample preparations need to be improved to avoid impurities during the assembly process. Practically conducting the assembly process in the controllable free-dust environment may resolve this issue. The next work to be done is ensuring the filter and external circuitry integration after etching does not destroy the filter and maintaining the surface as clean as possible from any impurities.

There are also a few experimental works that interesting to pursue, for example, on-chip interference filter deposition in the image sensor. If doing so, the first issue to resolve is how to keep the CMOS image sensor function after multilayer deposition, which requires extreme conditions. Exploiting rigid and stable yet transparent materials to protect the CMOS sensor before the deposition process is an exciting option to be considered.

Another outstanding work including integrates the uniform yet narrow-spectrum excitation light and image sensor for a compact and low invasiveness device. Also, how to manage its light direction relatively parallel with the image surface similar to the fiber-coupled laser setup and light from fluorescence excitation. Employing micro-LEDs with excitation filter and light guide structure deposited on it is a potential approach to get that of assembled high-quality excitation light. Another interesting idea is utilizing the available planar light sources in the form of electroluminescence and an organic LED flexible sheet. Such a light source provides a uniform light in various wavelengths, and it can be placed on the top of the composite filter. Since the light source structure itself is planar, the emitted light will reach all imaging area entirely to produce a uniform illumination over the image sensor.

References

[1] L. Squire, D. Berg, F. E. Bloom, and S. du Lac, *Fundamental Neuroscience*. Academic Press, 2018.

[2] J. N. D. Kerr and W. Denk, "Imaging in vivo: Watching the brain in action," *Nat. Rev. Neurosci.*, vol. 9, no. 3, pp. 195–205, 2008.

[3] J. W. Lichtman and W. Denk, "The big and the small: Challenges of imaging the brain's circuits," *Science (80-.).*, vol. 334, no. 6056, pp. 618–623, 2011.

[4] C. A. Siciliano and K. M. Tye, "Leveraging calcium imaging to illuminate circuit dysfunction in addiction.," *Alcohol*, vol. 74, pp. 47–63, Feb. 2019.

[5] B. N. Kuhn, P. W. Kalivas, and A. C. Bobadilla, "Understanding Addiction Using Animal Models," *Front. Behav. Neurosci.*, vol. 13, no. November, pp. 1–24, 2019.

[6] O. Lopatina *et al.*, "Anxiety- and depression-like behavior in mice lacking the CD157/BST1 gene, a risk factor for Parkinson's disease," *Front. Behav. Neurosci.*, vol. 8, p. 133, 2014.

[7] J. Ohta *et al.*, "Implantable Microimaging Device for Observing Brain Activities of Rodents," *Proc. IEEE*, vol. 105, no. 1, pp. 158–166, 2017.

[8] M. Prince, A. Wimo, M. Guerchet, G.-C. Ali, Y.-T. Wu, and M. Prina, "WorldAlzheimerReport2015.pdf," 2015.

[9] E. R. Dorsey *et al.*, "Projected number of people with Parkinson disease in the most populous nations, 2005 through 2030," *Neurology*, vol. 68, no. 5, pp. 384–386, 2007.

[10] "A public health priority."

[11] Y. Shen, S. M. Specht, D. S. G. Ioline, and R. Li, "The hippocampus: A biological model for studying learning and memory," *Prog. Neurobiol.*, vol. 44, no. 5, pp. 485–496, 1994.

[12] Y. Mu and F. H. Gage, "Adult hippocampal neurogenesis and its role in Alzheimer's disease," *Mol. Neurodegener.*, vol. 6, no. 1, pp. 1–9, 2011.

[13] W. J. P. Henneman *et al.*, "Hippocampal atrophy rates in Alzheimer disease," *Neurology*, vol. 72, no. 11, pp. 999–1007, 2009.

[14] G. Oh, E. Chung, and S. H. Yun, "Optical fibers for high-resolution in vivo microendoscopic fluorescence imaging," *Opt. Fiber Technol.*, vol. 19, pp. 760–771, 2013.

[15] S. Turtaev, I. T. Leite, T. Altwegg-Boussac, J. M. P. Pakan, N. L. Rochefort, and T. Čižmár, "High-fidelity multimode fibre-based endoscopy for deep brain in vivo imaging," *Light Sci. Appl.*, vol. 7, no. 1, 2018.

[16] I. N. Papadopoulos, S. Farahi, C. Moser, and D. Psaltis, "High-resolution, lensless endoscope based on digital scanning through a multimode optical fiber," *Biomed. Opt. Express*, vol. 4, no. 2, p. 260, 2013.

[17] L. V. Doronina-Amitonova *et al.*, "Implantable fiber-optic interface for parallel multisite long-term optical dynamic brain interrogation in freely moving mice," *Sci. Rep.*, vol. 3, pp. 1–8, 2013.

[18] K. J. Mack and P. A. Mack, "Induction of transcription factors in somatosensory cortex after tactile stimulation.," *Brain Res. Mol. Brain Res.*, vol. 12, no. 1–3, pp. 141–147, Jan. 1992.

[19] K. K. Ghosh *et al.*, "Miniaturized integration of a fluorescence microscope," *Nat. Methods*, vol. 8, no. 10, pp. 871–878, 2011.

[20] J. H. Park *et al.*, "Head-mountable high speed camera for optical neural recording," *J. Neurosci. Methods*, vol. 201, no. 2, pp. 290–295, 2011.

[21] D. Aharoni, B. S. Khakh, A. J. Silva, and P. Golshani, "All the light that we can see: a new era in miniaturized microscopy," *Nat. Methods*, vol. 16, no. 1, pp. 11–13, 2019.

[22] J. Senarathna, K. Murari, R. Etienne-Cummings, and N. V. Thakor, "A miniaturized platform for laser speckle contrast imaging," *IEEE Trans. Biomed. Circuits Syst.*, vol. 6, no. 5, pp. 437–445, 2012.

[23] A. Ozcan and E. McLeod, "Lensless Imaging and Sensing," *Annu. Rev. Biomed. Eng.*, vol. 18, no. 1, pp. 77–102, 2016.

[24] M. Haruta *et al.*, "An implantable CMOS device for blood-flow imaging during experiments on freely moving rats," *Jpn. J. Appl. Phys.*, vol. 53, no. 4s, p. 04EL05, 2014.

[25] K. Sasagawa *et al.*, "An Implantable CMOS Image Sensor With Self-Reset Pixels for Functional Brain Imaging," *IEEE Trans. Electron Devices*, vol. 63, no. 1, pp. 215–222, Jan. 2016.

[26] T. Yamaguchi *et al.*, "Implantable self-reset CMOS image sensor and its application to hemodynamic response detection in living mouse brain," *Jpn. J. Appl. Phys.*, vol. 55, no. 4, 2016.

[27] Y. Sunaga, Y. Ohta, Y. M. Akay, J. Ohta, and M. Akay, “Monitoring neural activities in the VTA in response to nicotine intake using a novel implantable microimaging device,” *IEEE Access*, vol. 8, pp. 68013–68020, 2020.

[28] H. Takehara *et al.*, “Implantable micro-optical semiconductor devices for optical theranostics in deep tissue,” *Appl. Phys. Express*, vol. 9, no. 4, p. 47001, 2016.

[29] A. Greenbaum *et al.*, “Imaging without lenses: Achievements and remaining challenges of wide-field on-chip microscopy,” *Nat. Methods*, vol. 9, no. 9, pp. 889–895, 2012.

[30] M. Bigas, E. Cabruja, J. Forest, and J. Salvi, “Review of CMOS image sensors,” *Microelectronics J.*, vol. 37, no. 5, pp. 433–451, 2006.

[31] N. Waltham, “CCD and CMOS sensors,” *ISSI Sci. Reports Ser.*, 2010.

[32] M. Sarkar and A. Theuwissen, “Design of a CMOS Image Sensor. In: A Biologically Inspired CMOS Image Sensor. Studies in Computational Intelligence,” Springer US, 2013, pp. 49–104.

[33] J. Ohta, “Smart CMOS Image Sensors and Applications,” in *Second Edition*, 2019, p. 1.

[34] I. Sigal *et al.*, “Imaging brain activity during seizures in freely behaving rats using a miniature multi-modal imaging system,” *Biomed. Opt. Express*, vol. 7, no. 9, p. 3596, 2016.

[35] P. Miao *et al.*, “Chronic wide-field imaging of brain hemodynamics in behaving animals,” *Biomed. Opt. Express*, vol. 8, no. 1, p. 436, 2017.

[36] V. Matus, E. Eso, S. R. Teli, R. Perez-Jimenez, and S. Zvanovec, “Experimentally derived feasibility of optical camera communications under turbulence and fog conditions,” *Sensors (Switzerland)*, vol. 20, no. 3, 2020.

[37] L. Randers-Eichhorn, C. R. Albano, J. Sipior, W. E. Bentley, and G. Rao, “On-line green fluorescent protein sensor with LED excitation,” *Biotechnol. Bioeng.*, 1997.

[38] N. C. Shaner, P. A. Steinbach, and R. Y. Tsien, “A guide to choosing fluorescent proteins,” 2005.

[39] H. Takehara *et al.*, “On-chip cell analysis platform: Implementation of contact fluorescence microscopy in microfluidic chips,” *AIP Adv.*, vol. 7, no. 9, p. 095213/8, 2017.

[40] W. Zong *et al.*, “Fast high-resolution miniature two-photon microscopy for brain imaging in freely behaving mice,” *Nat. Methods*, vol. 14, no. 7, pp. 713–719, 2017.

[41] S. O'Sullivan *et al.*, "Developments in transduction, connectivity and AI/machine learning for point-of-care testing," *Sensors (Switzerland)*, vol. 19, no. 8, pp. 1–31, 2019.

[42] M. Punjiya, C. H. Moon, and S. S. Nanolab, "Multi-analyte paper-analytical-devices (PAD) with CMOS integration for point-of-Care diagnostics," in *2016 IEEE International Symposium on Circuits and Systems (ISCAS)*, 2016, pp. 2883–2886.

[43] H. Klapproth *et al.*, "Development of a multi-analyte CMOS sensor for point-of-care testing," *Sens. Bio-Sensing Res.*, vol. 5, pp. 117–122, 2015.

[44] Y. Adiguzel and H. Kulah, "CMOS Cell Sensors for Point-of-Care Diagnostics," *Sensors (Basel, Switzerland)*, vol. 12, no. 8. pp. 10042–10066, 2012.

[45] M. Chalfie, Y. Tu, G. Euskirchen, W. W. Ward, and D. C. Prasher, "Green fluorescent protein as a marker for gene expression," *Science (80-.).*, vol. 263, no. 5148, pp. 802–805, 1994.

[46] M. Zimmer, "Green fluorescent protein (GFP): Applications, structure, and related photophysical behavior," *Chem. Rev.*, vol. 102, no. 3, pp. 759–781, 2002.

[47] A. N. van den Pol and P. K. Ghosh, "Selective neuronal expression of green fluorescent protein with cytomegalovirus promoter reveals entire neuronal arbor in transgenic mice.," *J. Neurosci.*, vol. 18, no. 24, pp. 10640–10651, Dec. 1998.

[48] Y. Zuo *et al.*, "Fluorescent proteins expressed in mouse transgenic lines mark subsets of glia, neurons, macrophages, and dendritic cells for vital examination," *J. Neurosci.*, vol. 24, no. 49, pp. 10999–11009, 2004.

[49] K. Jósvay *et al.*, "Besides neuro-imaging, the Thy1-YFP mouse could serve for visualizing experimental tumours, inflammation and wound-healing," *Sci. Rep.*, vol. 4, pp. 1–7, 2014.

[50] X. Wei *et al.*, "Dopamine D1 or D2 receptor-expressing neurons in the central nervous system," *Addict. Biol.*, vol. 23, no. 2, pp. 569–584, 2018.

[51] N. Pokala and E. E. Glater, "Using Optogenetics to Understand Neuronal Mechanisms Underlying Behavior in C. elegans.," *J. Undergrad. Neurosci. Educ.*, vol. 16, no. 2, pp. A152–A158, 2018.

[52] J. Nakai, M. Ohkura, and K. Imoto, "A high signal-to-noise ca2+ probe composed of a single green fluorescent protein," *Nat. Biotechnol.*, vol. 19, no. 2, pp. 137–141, 2001.

[53] G. Ji *et al.*, "Ca2+-sensing transgenic mice: Postsynaptic signaling in smooth muscle," *J. Biol. Chem.*, vol. 279, no. 20, pp. 21461–21468, 2004.

[54] J. Akerboom *et al.*, "Crystal structures of the GCaMP calcium sensor reveal the mechanism of fluorescence signal change and aid rational design," *J. Biol. Chem.*, vol. 284, no. 10, pp. 6455–6464, 2009.

[55] J. Akerboom *et al.*, "Optimization of a GCaMP calcium indicator for neural activity imaging," *J. Neurosci.*, vol. 32, no. 40, pp. 13819–13840, 2012.

[56] T. W. Chen *et al.*, "Ultrasensitive fluorescent proteins for imaging neuronal activity," *Nature*, vol. 499, no. 7458, pp. 295–300, 2013.

[57] J. Reichman, *Handbook of Optical Filters for Fluorescence Microscopy*, no. Chroma Technology Corp., 2010.

[58] M. Dandin, P. Abshire, and E. Smela, "Optical filtering technologies for integrated fluorescence sensors," *Lab Chip*, vol. 7, no. 8, pp. 955–977, 2007.

[59] J. R. Lakowicz, *Principles of Fluorescence Spectroscopy*, 3rd ed. Springer US, 2006.

[60] J. Alex Chediak, Z. Luo, J. Seo, N. Cheung, L. P. Lee, and T. D. Sands, "Heterogeneous integration of CdS filters with GaN LEDs for fluorescence detection microsystems," *Sensors Actuators, A Phys.*, vol. 111, no. 1, pp. 1–7, 2004.

[61] Y. Dattner and O. Yadid-Pecht, "Low light cmos contact imager with an integrated poly-acrylic emission filter for fluorescence detection," *Sensors*, vol. 10, no. 5, pp. 5014–5027, 2010.

[62] R. R. Singh, D. Ho, A. Nilchi, G. Gulak, P. Yau, and R. Genov, "A CMOS/thin-film fluorescence contact imaging microsystem for DNA analysis," *IEEE Trans. Circuits Syst. I Regul. Pap.*, vol. 57, no. 5, pp. 1029–1038, 2010.

[63] K. Sasagawa *et al.*, "Complementary metal-oxide-semiconductor image sensor with microchamber array for fluorescent bead counting," *Jpn. J. Appl. Phys.*, vol. 51, no. 2 PART 2, 2012.

[64] T. Kobayashi *et al.*, "Functional neuroimaging by using an implantable CMOS multimodal device in a freely-moving mouse," in *2011 IEEE Biomedical Circuits and Systems Conference (BioCAS)*, 2011, pp. 110–113.

[65] M. Beiderman, T. Tam, A. Fish, G. Jullien, and O. Yadid-Pecht, “A low-light CMOS Contact Imager With an Emission Filter for Biosensing Applications,” *Biomed. Circuits Syst. IEEE Trans.*, vol. 2, pp. 193–203, 2008.

[66] D. E. Schwartz, P. Gong, and K. L. Shepard, “Time-resolved Förster-resonance-energy-transfer DNA assay on an active CMOS microarray,” *Biosens. Bioelectron.*, vol. 24, no. 3, pp. 383–390, 2008.

[67] K. Sasagawa, A. Kimura, M. Haruta, T. Noda, T. Tokuda, and J. Ohta, “Highly sensitive lens-free fluorescence imaging device enabled by a complementary combination of interference and absorption filters,” *Biomed. Opt. Express*, vol. 9, no. 9, pp. 4329–4344, 2018.

[68] C. Richard, A. Renaudin, V. Aimez, and P. G. Charette, “An integrated hybrid interference and absorption filter for fluorescence detection in lab-on-a-chip devices,” *Lab Chip*, vol. 9, no. 10, pp. 1371–1376, 2009.

[69] A. Hassibi *et al.*, “4.2 A fully integrated CMOS fluorescence biochip for multiplex polymerase chain-reaction (PCR) processes,” in *2017 IEEE International Solid-State Circuits Conference (ISSCC)*, 2017, pp. 68–69.

[70] H. Takehara *et al.*, “Micro-light-pipe array with an excitation attenuation filter for lensless digital enzyme-linked immunosorbent assay,” *Jpn. J. Appl. Phys.*, vol. 55, no. 3, 2016.

[71] S. Pang, C. Han, L. M. Lee, and C. Yang, “Fluorescence microscopy imaging with a Fresnel zone plate array based optofluidic microscope,” *Lab Chip*, vol. 11, no. 21, pp. 3698–3702, 2011.

[72] A. K. Mudraboyina, L. Blockstein, C. C. Luk, N. I. Syed, and O. Yadid-Pecht, “A Novel Lensless Miniature Contact Imaging System for Monitoring Calcium Changes in Live Neurons,” *IEEE Photonics J.*, vol. 6, no. 1, pp. 1–15, Feb. 2014.

[73] H. M. Lai, W. L. Ng, S. M. Gentleman, and W. Wu, “Chemical Probes for Visualizing Intact Animal and Human Brain Tissue,” *Cell Chem. Biol.*, vol. 24, no. 6, pp. 659–672, 2017.

[74] J. Dutta Majumdar and I. Manna, “Laser processing of materials,” *Sadhana - Acad. Proc. Eng. Sci.*, vol. 28, no. 3–4, pp. 495–562, 2003.

[75] R. Delmdahl and J. L. Tapié, “Excimer lasers drive large-area microprocessing,” *Appl. Surf. Sci.*, vol. 258, no. 23, pp. 9123–9127, 2012.

[76] W. S. Wong *et al.*, “Integration of GaN thin films with dissimilar substrate materials by Pd-In metal bonding and laser lift-off,” *J. Electron. Mater.*, vol. 28, no. 12, pp. 1409–1413, 1999.

[77] W. S. Wong, T. Sands, and N. W. Cheung, “Damage-free separation of GaN thin films from sapphire substrates,” *Appl. Phys. Lett.*, vol. 72, no. 5, pp. 599–601, 1998.

[78] T. Ueda, M. Ishida, and M. Yuri, “Separation of thin GaN from sapphire by laser lift-off technique,” *Jpn. J. Appl. Phys.*, vol. 50, p. 041001, 2011.

[79] A. Kawan, S.-J. Yu, and J.-H. Sung, “Study of Laser Lift-Off Process for Fabrication of GaN-Based 365-nm Ultraviolet Absorption Layer Removed Flip Chip LED,” *Trans. Electr. Electron. Mater.*, vol. 19, no. 3, pp. 230–234, Jun. 2018.

[80] W. S. Wong *et al.*, “Fabrication of thin-film InGaN light-emitting diode membranes by laser lift-off,” *Appl. Phys. Lett.*, vol. 75, no. 10, pp. 1360–1362, 1999.

[81] X. Bao *et al.*, “Design and fabrication of AlGaInP-based micro-light-emitting-diode array devices,” *Opt. Laser Technol.*, vol. 78, pp. 34–41, 2016.

[82] M. Miyachi, Y. Kimura, and K. Chikuma, “AlGainN/AlGaInP Two-Wavelength Laser Diodes Fabricated by Wafer-Level Transferring Technique,” *Japanese J. Appl. Physics, Part 2 Lett.*, vol. 43, no. 2 A, 2004.

[83] W. S. Wong, M. Kneissl, P. Mei, D. W. Treat, M. Teepe, and N. M. Johnson, “The Integration of InxGa1-xN Multiple-Quantum-Well Laser Diodes with Copper Substrates by Laser Lift-Off,” *Jpn. J. Appl. Phys.*, vol. 39, no. Part 2, No. 12A, pp. L1203–L1205, Dec. 2000.

[84] J. Chun *et al.*, “Laser lift-off transfer printing of patterned GaN light-emitting diodes from sapphire to flexible substrates using a Cr/Au laser blocking layer,” *Scr. Mater.*, vol. 77, pp. 13–16, 2014.

[85] S. Fang, J. Liang, Z. Liang, Y. Qin, J. Lv, and W. Wang, “Strategy and mechanics for bendable micro-light emitting diode array integrated by polymer,” *Microelectron. Eng.*, vol. 179, pp. 13–17, 2017.

[86] S. J. Kim *et al.*, “High-Performance Flexible Thermoelectric Power Generator Using Laser Multiscanning Lift-Off Process,” *ACS Nano*, vol. 10, no. 12, pp. 10851–10857, 2016.

[87] R. Delmdahl, R. Pätzel, and J. Brune, “Large-area laser-lift-off processing in microelectronics,” *Phys. Procedia*, vol. 41, pp. 241–248, 2013.

[88] T. Fischer, *Materials Science for Engineering Students*. Academic Press, 2009.

[89] S. J. Pearton, *GaN and Related Materials II*. Taylor & Francis Group, 2000.

[90] X. J. Su *et al.*, “Shock-induced brittle cracking in {HVPE}-{GaN} processed by laser lift-off techniques,” *J. Phys. D. Appl. Phys.*, vol. 46, no. 20, p. 205103, May 2013.

[91] I. Vurgaftman and J. R. Meyer, “Band parameters for nitrogen-containing semiconductors,” *J. Appl. Phys.*, vol. 94, no. 6, pp. 3675–3696, 2003.

[92] J. H. Robertson and W. C. Clark, “Laser in Neurosurgery,” Springer, 1998, p. 31.

[93] A. H. Guenther, “Laser-Induced Damage in Optical Materials:2005,” Proceeding of SPIE volume 5991, 2005, p. 4.

[94] C. Dette *et al.*, “TiO2 Anatase with a Bandgap in the Visible Region,” *Nano Lett.*, vol. 14, no. 11, pp. 6533–6538, Nov. 2014.

[95] F. Z. Tepehan, F. E. Ghodsi, N. Ozer, and G. G. Tepehan, “Determination of optical properties of amorphous Ta2O5 films deposited by spin- and dip-coating methods,” *Sol. Energy Mater. Sol. Cells*, vol. 46, no. 4, pp. 311–321, 1997.

[96] E. Gnani, S. Reggiani, R. Colle, and M. Rudan, “Band-structure calculations of SiO/sub 2/ by means of Hartree-Fock and density-functional techniques,” *IEEE Trans. Electron Devices*, vol. 47, no. 10, pp. 1795–1803, Oct. 2000.

[97] G. L. Tan, M. F. Lemon, D. J. Jones, and R. H. French, “Optical properties and London dispersion interaction of amorphous and crystalline SiO2 determined by vacuum ultraviolet spectroscopy and spectroscopic ellipsometry,” *Phys. Rev. B - Condens. Matter Mater. Phys.*, vol. 72, no. 20, pp. 1885–1892, 2005.

[98] T. Xu, Z. Tao, H. Li, X. Tan, and H. Li, “Effects of deep reactive ion etching parameters on etching rate and surface morphology in extremely deep silicon etch process with high aspect ratio,” *Adv. Mech. Eng.*, vol. 9, no. 12, pp. 1–19, 2017.

[99] H. Takehara *et al.*, “Intravital fluorescence imaging of mouse brain using implantable semiconductor devices and epi-illumination of biological tissue,” *Biomed. Opt. Express*, vol. 6, no. 5, pp. 1553–1564, 2015.

[100] K. Sugie, K. Sasagawa, M. C. Guinto, M. Haruta, T. Tokuda, and J. Ohta, “Implantable CMOS image sensor with incident-angle-selective pixels,” *Electron. Lett.*, vol. 55, no. 13, pp. 729–731, 2019.

List of Publications

Journal Article

Erus Rustami, Kiyotaka Sasagawa, Kenji Sugie, Yasumi Ohta, Makito Haruta, Toshihiko Noda, Takashi Tokuda, Jun Ohta, "Needle-Type Imager Sensor With Band-Pass Composite Emission Filter and Parallel Fiber-Coupled Laser Excitation," in IEEE Transactions on Circuits and Systems I: Regular Papers, vol. 67, no. 4, pp. 1082-1091, April 2020, DOI: 10.1109/TCSI.2019.2959592.

Proceedings

Erus Rustami, Kiyotaka Sasagawa, Yasumi Ohta, Makito Haruta, Toshihiko Noda, Takashi Tokuda, Jun Ohta, "A Thin Composite Emission Filter and Fiber Coupled Laser Excitation for Implantable Fluorescence Imager Application," 2019 IEEE International Symposium on Circuits and Systems (ISCAS), Sapporo, Japan, 2019, pp. 1-4, DOI:10.1109/ISCAS.2019.8702179.

Erus Rustami, Kiyotaka Sasagawa, Thanet Pakpuwadon, Yasumi Ohta, Hironari Takehara, Makito Haruta, Jun Ohta, “Fabrication of thin composite emission filter for high performance lens-free fluorescent imager,” Proc. SPIE 11235, Microfluidics, BioMEMs, and Medical Microsystems XVIII, 112350F (21 February 2020): https://doi.org/10.1117/12.2546540

Kiyotaka Sasagawa, **Erus Rustami**, Hironari Takehara, Makito Haruta, Jun Ohta, "An Implantable light source for in vivo fluorescence image sensor" Proc. SPIE 11235,

Microfluidics, BioMEMs, and Medical Microsystems XVIII, 112350U (21 February 2020); https://doi.org/10.1117/12.2545482

International Conferences

[1] **Erus Rustami**, Kiyotaka Sasagawa, Yasumi Ohta, Makito Haruta, Toshihiko Noda, Takashi Tokuda, Jun Ohta, "Implantable CMOS Image Sensor Using Multilayer Filter Emission and Fiber Coupled Laser Excitation" 4th International Workshop on Image Sensor and Imaging Systems (IWISS) on November 27-29, 2018 at Tokyo Institute of Technology, Tokyo, Japan (*poster presenter*).

[2] **Erus Rustami**, KiyotakaSasagawa, YasumiOhta, MakitoHaruta, Toshihiko Noda, Takashi Tokuda, Jun Ohta, " A Thin Composite Emission Filter and Fiber Coupled Laser Excitation for Implantable Fluorescence Imager Application," 2019 IEEE International Symposium on Circuits and Systems (ISCAS) on May 26-29, 2019 at Sapporo Convention Center, Hokkaido, Japan (*oral presenter*).

[3] **Erus Rustami**, Kiyotaka Sasagawa, Yasumi Ohta, Makito Haruta, Toshihiko Noda, Takashi Tokuda, Jun Ohta, " Band-Pass Emission Filter Combined with Fiber Coupled Laser for High-Performance Implantable Fluorescent Imager"10th International Conference on Molecular Electronics & BioElectronics (ICMEBE) on June 25-27, 2019 at Nara Kasugano International Forum, Nara, Japan (*oral presenter*).

Domestic Conferences

[1] **Erus Rustami**, Kiyotaka Sasagawa, Thanet Pakpuwadon, Yasumi Ohta, Hironari Takehara, Makito Haruta, Jun Ohta, "Fabrication of Large-Size and High-Uniformity Thin Composite Emission Filter for Lens-Free Fluorescent Imager" ITE Workshop of Technical Group on

Information Sensing Technologies (ITE-IST) (online) on July 1, 2020, on Tokyo University on Science, Tokyo (*oral presenter*).

[2] Mohamad Izzat Azmer, Kiyotaka Sasagawa, **Erus Rustami**, Yasumi Ohta, Hironari Takehara, Makito Haruta, Jun Ohta, "Light Source with High-Performance Emission Filter for Implantable Fluorescence Imaging Device,"

第67回応用物理学会春季学術講演会, 2020.3.13. 上智大学　四谷キャンパス.

[3] Kiyotaka Sasagawa, Yasumi Ohta, Mamiko Kawahara, **Erus Rustami**, Makito Haruta, Takashi Tokuda, Jun Ohta,

"生体埋植蛍光イメージングデバイスの高性能化,"

第42回日本神経科学大会(NEURO2019), 2019.7.27. Toki Messe, Niigata, Japan

[4] **Erus Rustami**, Kiyotaka Sasagawa, Yasumi Ohta, Makito Haruta, Toshihiko Noda, Takashi Tokuda, Jun Ohta, "A needle shape fluorescence micro-imager with interference and absorption filters" 31st Annual Meeting of the Institute of Electrical Engineers of Japan (IEEJ), Hokkaido, 12-14 March 2019 (*oral presenter*).

[5] **Erus Rustami**, Kiyotaka Sasagawa, Yasumi Ohta, Makito Haruta, Toshihiko Noda, Takashi Tokuda, Jun Ohta, "An Implantable CMOS Image Sensor Using Fiber Coupled Laser Excitation," 79th Autumn Meeting, Japanese Society of Applied Physics (JSAP), Nagoya, 18-21 September 2018 (*oral presenter*).